Title of Report: Grain boundary engineering and radiation resistance of GFR candidate metallic materials

Project Title: High Temperature Metallic Materials for GFR

Date of Report: July 31, 2006

Investigators:

Todd Allen, University of Wisconsin, 608-265-4083, allen@engr.wisc.edu

Gary Was, University of Michigan, 734-647-7030, gsw@umich.edu

Jian Gan, Idaho National Laboratory, 208-533-7385, jian.gan@inl.gov

Grain boundary engineering and radiation resistance of GFR candidate metallic materials

T. R. Allen, University of Wisconsin
G. S. Was, University of Michigan
Jian Gan, Idaho National Laboratory

Executive Summary

Research Objectives

Currently, insufficient physical property data exist to qualify candidate material for gas-cooled fast reactor (GFR) designs. The goal of this project is to develop advanced tailored microstructures that will improve radiation resistance, creep resistance, and oxidation resistance, helping to establish metallic materials capable of supporting GFR designs.

The first goal of this project is to improve high temperature creep strength and resistance to environmental attack by optimizing grain boundary structural orientations (a technique known as grain boundary engineering-GBE). Thermal-mechanical treatment is performed on candidate metal alloys to maximize the fraction of low-energy grain boundaries. Following treatment, the changes to microstructure are characterized and response to mechanical loading, radiation, and environmental attack are examined. The focus is on Alloy 800H, an austenitic alloy designed for high temperature boiler components, alloy 617, a Ni-base alloy being considered for high-temperature reactor piping, and T-91, a low carbon (9Cr-MoVNb) ferritic-martensitic alloy designed for lower temperature boiler components and being considered for higher temperature pressure vessels.

The second goal of the project is to characterize radiation resistance of candidate GFR metallic materials with focus on Alloy 800H. Candidate metallic materials for the GFR have not typically been used for high dose core components so an understanding of the radiation resistance is unknown. Therefore, radiation response of these alloys will be characterized by examining the changes in microstructure in samples irradiated with high-energy ions and when available, neutrons from a test reactor.

Research Accomplishments

Grain Boundary Engineering. Grain boundary engineering involves a series of thermo-mechanical treatments designed to convert a fraction of the high-energy grain boundaries to low-energy boundaries (identified as Coincident Site Lattice [CSL] boundaries), thus reducing cracking susceptibility and improving creep strength and oxidation resistance. This project developed the first treatment to enhance the fraction of CSL boundaries in an advanced, ferritic-martensitic steel–T91. The challenge was to enhance the grain boundaries without disturbing the original microstructure. Since the microstructure is critical to achieving high-temperature properties, the heat treatment process requires strict control. A treatment was developed in which the CSL boundary fraction of T91 was enhanced over the as-received case without changing other critical features of the microstructure, such as, grain size, carbide size and location, density, and hardness. Improved creep strength resulted from the preservation of all the microstructural features decisive for creep strength in T-91, and from increasing the fraction of low energy boundaries. In addition to T91, CSL enhancement techniques were developed for alloy 800H, a higher temperature alloy seen as a candidate for high-temperature, gas-cooled reactors. The GBE treatment improved the spallation resistance of the protective oxide formed on 800H when exposed to supercritical water to temperatures of 600°C. This spallation resistance of the GBE-treated material needs to be tested in higher temperature flowing helium with controlled oxygen levels to understand limits of applicability to the GFR environment. Creep and radiation resistance tests of GBE-treated Alloy 800H are in progress. Grain boundary treatments have also been developed for two different lots of Alloy 617, a high temperature capable alloy in consideration for gas reactor piping. Future environmental tests will examine GBE-treated 617.

Radiation Stability of 800H. The second, and relatively minor task, was to examine the radiation stability of Alloy 800H. Heavy ion irradiation was performed to evaluate the radiation response of Alloy 800H. The microstructure of 800H following heavy ion irradiation was examined and no surprising microstructures were found. Radiation resistance tests of standard and GBE-treated Alloy 800H are in progress for samples irradiated in the ATR and HFIR reactors.

Table of Contents

Project Objective....6
Grain Boundary Engineering....6
References....9
A. Grain Boundary Engineering of Alloys T91 and HT9....10
  A.1 Overview....11
    A.1.1 Optimizing Boundaries in T91 and HT-9....11
    A.1.2 Thermal stability of thermo-mechanical treatments for T91....13
    A.1.3 Creep of T91....14
    A.1.3 Microstructural investigation of as-received, aged, crept, and optimized alloys T91....17
  A.2 Future Work....21
  A.3 References....22
B. Grain Boundary Engineering of Alloy 800H....23
  B.1 Overview....24
    B.1.1. Materials and Methods....24
    B.1.2. Optimizing grain boundaries in alloy 800H....24
      B.1.2.1 Coincidence Site Lattice Boundaries (CSLBs)....25
      B.1.2.2 Misorientation....26
      B.1.2.3 Grain Size....28
      B.1.2.4 Verification and Comparison....29
      B.1.2.5. Hardness....29
      B.1.2.6. Thermal Stability of GBE....30
    B.1.3. Grain Boundary Composition....31
    B.1.4. Specimen Preparation for Mechanical Tests....35
  B.2. Supercritical Water (SCW) Exposure....37
  B.3 Future Work....40
  B.4 References....40
C. Grain Boundary Engineering of Alloy 617....42
  C.1. Overview....43
    C.1.1 Single compression and annealing treatments....43
    C.1.2 Multi-step compression and annealing treatments....46
  C.2. Thermal Stability of GBE....50
  C.3. Supercritical Water (SCW) Exposure....51
  C.4. Future Work....52
  C.5 References....53
D. Radiation Response of Alloy 800H....54
  D.1. Literature survey of radiation effects in alloy 800H and alloy 800....55
    D.1.1 Elongation....55
    D.1.2 Grain Size Effects....58
    D.1.3 Fatigue....60
    D.1.4 Tensile....62
    D.1.6 Swelling....63
    D.1.7 Creep....64
    D.1.8 Embrittlement....68
  D.2. Microstructural changes in alloy 800H due to heavy ion irradiation....69

D.2.1 Materials and methods ... 69
D.2.2 Ion-irradiated 800H Irradiated microstructure of 800H ... 69
D.2.3 800H Irradiated in ATR, HFIR, and PHENIX ... 73
D.3 Future Work ... 73
D.4 References ... 73
E. Literature Survey of Radiation Effects in High Temperature Ni-Base Alloys (Hastelloy Variants) ... 74
E.1 Mechanical Strength-thermal Aging ... 75
E.2 Mechanical Strength and Ductility-irradiation ... 78
E.3 Fatigue ... 84
E.4 Creep ... 86
E.5 Creep Rupture ... 88
E.5 References ... 88
F. Conclusions and Outlook ... 89
G. Papers ... 90

Project Objective

Currently, insufficient physical property data exist to qualify candidate material for gas-cooled fast reactor (GFR) designs. The goal of this project is to develop advanced tailored microstructures that will improve radiation resistance, creep resistance, and oxidation resistance, helping to establish metallic materials for GFR designs.

The first goal of this project is to improve high temperature creep strength and resistance to environmental attack by optimizing grain boundary structural orientations (a technique known as grain boundary engineering-GBE). Thermal-mechanical treatment is performed on GFR candidate metal alloys to maximize the fraction of low-energy boundaries. Following treatment, the changes to microstructure are characterized and response to mechanical loading, radiation, and environmental attack are examined. The focus is on Alloy 800H, an austenitic alloy designed for high temperature boiler components, alloy 617, a Ni-base alloy being considered for high-temperature reactor piping, and T-91, a low carbon (9Cr-MoVNb) ferritic-martensitic alloy designed for lower temperature boiler components and being considered for higher temperature pressure vessels.

The second goal of the project is to characterize radiation resistance of candidate GFR metallic materials. Candidate metallic materials for the GFR have not typically been used for high dose core components. Therefore, radiation response of these alloys will be characterized by examining the changes in microstructure in samples irradiated with high-energy ions and when available, neutrons from a test reactor. The focus is on Alloy 800H.

Grain Boundary Engineering

A major factor determining the physical, mechanical, electrical, and chemical properties of polycrystalline materials is the grain boundary structure. In 1929, Hargreaves and Hills first presented the theories of the grain boundary, which stated that different structures can exist for different grain boundaries in metals [1]. Later, Aust and Chalmer showed that these structural differences can lead to different grain boundary properties, such as boundary energy [2]. Kronberg and Wilson indicated the importance of the concept of a coincident site lattice (CSL), whereby at certain crystallographic misorientations, a three-dimensional lattice could be constructed with lattice points common to both adjacent crystals, as shown in Fig.1 [3] .

The CSL is considered the smallest common sublattice of the adjoining grains, the volume ratio of the unit cell of the CSL to that of the crystal is described by the parameter Σ, which can also be considered the reciprocal density of coincident sites. $\Sigma1$ orientation has all boundaries with only small misorientations and are called "small-angle grain boundaries," while the family of 110 tilt $\Sigma3$s is a particularly important set of boundaries because they have very low energy and occur frequently via twinning in materials such as austenitic steels, copper and nickel [3]. Small angular deviations from low Σ CSL relationships can be described as being accommodated by translations of one lattice relative to the other, conserving the periodicity of the exact CSL. The maximum angular deviation from an exact CSL is limited by the Brandon geometric criterion $\Delta\theta \leq 15°\Sigma^{-1/2}$. Low Σ grain boundaries, that is $\Sigma \leq 29$ and $\Delta\theta \leq 15°\Sigma^{-1/2}$, are characterized as “special boundaries”. Experimental studies over the past 40 years have shown that special grain boundaries have the following properties as compared to higher Σ and general boundaries:

1. Lower boundary energy
2. Less susceptible to impurity or solute segregation
3. Smaller diffusivity
4. Greater resistance to grain boundary sliding
5. Greater resistance to intergranular degradation, such as fracture, cavitation and localized corrosion

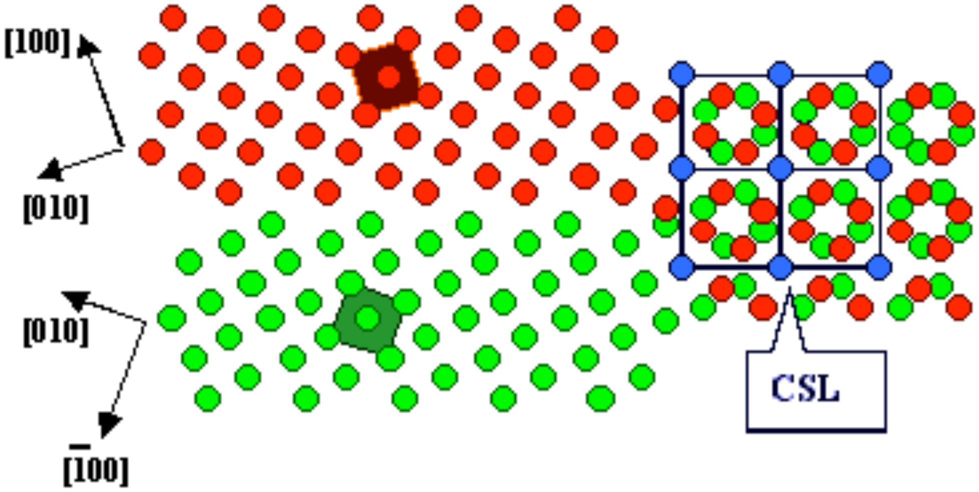

Fig.1. Schematic representation of the Coincidence Site Lattice geometry for a Σ5 interface

The concept of “grain boundary engineering” (GBE) was first introduced by Watanabe [5]. The objective was to improve the bulk properties of polycrystalline metals by increasing the number of “special” grain boundaries in the grain boundary character distribution (GBCD). Since then, GBE has been widely employed to control oxidation embrittlement [6], alleviate intergranular cracking [7], suppress elemental segregation and depletion at grain boundaries [8], and increase the intergranular corrosion resistance [9]. For example, Palumbo successfully increased the special boundaries (Σ≤29) in thermomechanically processed Alloy 600 from 37% to 71%, resulting in commensurate decreases in bulk intergranular corrosion susceptibility, and the material was used for nuclear steam generator tubing and the thermomechanical treatment design was patented [10]. GBE has been successfully applied on INCOLOY alloy 800H to improve the oxidation behavior in supercritical water [11, 12]; experimental results indicate that by promoting an increased Σ3 fraction, the oxide spallation is strongly alleviated on GBE-treated samples compared to control samples. Diffusion is known be significantly reduced in low Σ grain boundaries, as shown in figure 2, so the transport path of Fe cations to form new magnetite, may contribute to the oxide growth, texture, and increased stability.

Although the boundary misorientation is the main factor in GBE, another grain boundary parameter, the grain boundary inclination, should be considered [13]. In addition, the properties of a high-angle boundary are governed primarily by the presence of a low-index boundary plane [14, 15]. Therefore, to achieve materials development using GBE, multiple grain boundary requirements must be established. The following were proposed by Watanabe [13]: (1) grain boundary character distribution, (2) grain boundary misorientation distribution, (3) grain boundary inclination distribution, (4) grain boundary dihedral angle distribution, (5) grain boundary precipitate density distribution, (6) the stability of grain boundary configuration, and (7) the stability of grain boundary structure.

Typically, GBE processing involves two different thermomechanical treatments: one approach is to deform the material to strains that are on the order of 6-8% followed by annealing at temperatures low enough to prevent recrystallization yet cause reorientation of grain boundaries toward lower energy configurations; another approach employs a multi-cycle treatment of moderate strain levels (5-30%) with annealing treatments at relatively high temperatures but for very short times, which are typically on the order of 5-30 minutes. The group of materials amendable to thermomechanical processing is restricted to those that are capable of producing large proportions of Σ3 related boundaries. In practice this equates to metals and alloys that have low stacking fault energy (SFE) and so readily form annealing twins. Annealing twinning is thought to occur for one of two reasons: to decrease the overall interfacial energy when the energy of the boundaries between a grain's neighbors and its twin would be less than that of the boundaries between the neighbors and the grain itself, or to reorient grain boundaries so as to facilitate dislocation absorption and mobility during recrystallization [16]. The introduced twinning can result in the repeated replacement of general or high Σ boundaries with more structurally ordered boundaries. The stacking fault energy (SFE) has great influence on annealing twinning, and experimental results [17] showed that with lower SFE, a higher fraction of deformation twins was obtained after GBE treatment.

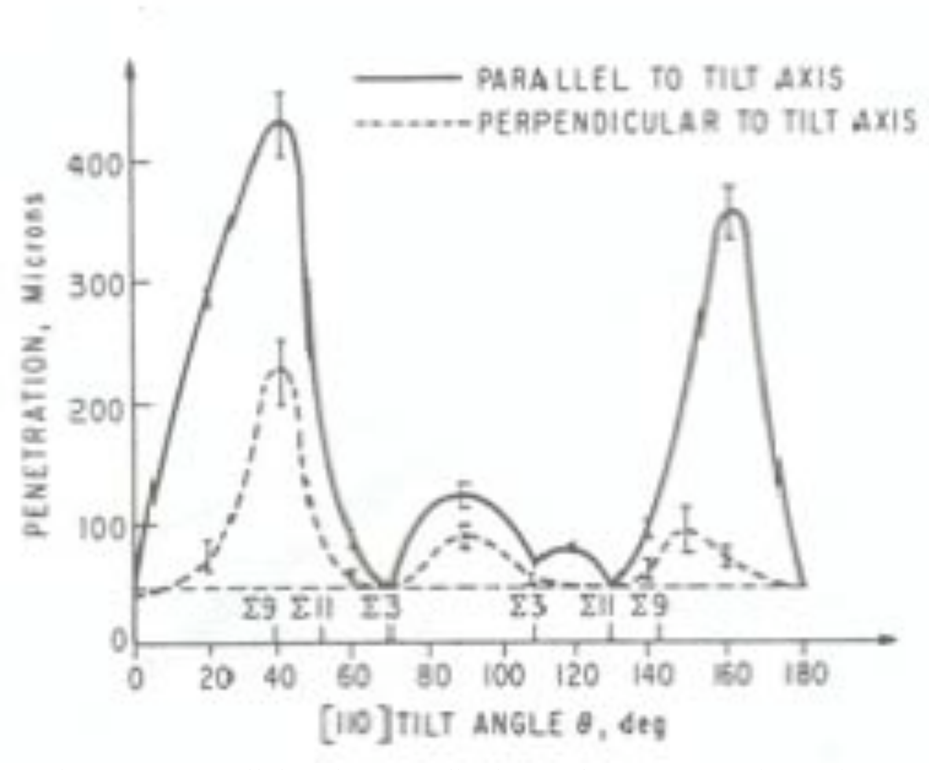

Fig.2. Penetration of Zn parallel and perpendicular to the [011] rotation axis of Al bicrystals [20]

References

[1] F.Hargreaves and R.Hill., "Work-softening and a Theory. of Intercrystalline Cohesion", Journal of the Institute of Metals Vol. XLI, No.1, p.257 (1929)

[2] K. T. Aust, B.Chalmers, "Energies and structures of grain boundaries", Metal Interfaces-A Seminar, Am. Soc. Metals Cleveland, O. , p.153 (1951)

[3] Kronberg ML, Wilson FH. 1949. Secondary recrystallization in copper. Trans Metall Soc AIME 185:501–514.

[4] V.Randle, The Role of the Coincidence Site Lattice in Grain Boundary Engineering, The Institute of Materials, London, 1996 p.65-89

[5] T. Watanabe, An approach to grain-boundary design for strong and ductile polycrystals, Res Mechanica 11 (1984) 47-84.

[6] S.Yamaura, Y.Igarashi, S.Tsurekawa and T.Watanabe, "Grain Boundary Engineering for The Control of Oxidation Embrittlement", Properties of Complex Inorganic Solids 2, p.27 (2000)

[7] C.Cheung and U.Erb, "Application of Grain Boundary Engineering Concepts to Alleviate Intergranular Cracking in Alloys 600 and 690", Materials Science and Engineering A185, p.39 (1994)

[8] Y.B.Hong, K.Hiroyuki, Z.J.Wang, et al., "Suppression of Chromium Depletion by Grain Boundary Structural Change during Twin-induced Grain Boundary Engineering of 304 Stainless Steel", Scripta Materialia 49, p.219 (2003)

[9] M.Shimada, H.Kokawa, Z.J.Wang, Y.S.Sato and I.Karibe, "Optimization of Grain Boundary Character Distribution for Intergranular Corrosion Resistant 304 Stainless Steel by Twin-induced Grain Boundary Engineering", Acta Materialia 50, p.2331 (2002)

[10] P.Lin, G.Palumbo, U.Erb and K.T.Aust, "Influence of Grain Boundary Character Distribution on Sensitization and Intergranular Corrosion of Alloy 600", Scripta Metallurgical et Materialia 33, p.1387 (1995)

[11] L.Tan, K.Sridharan and T.R.Allen, "The Effect of Grain Boundary Engineering on The Oxidation Behavior of INCOLOY Alloy 800H in Supercritical Water", J.Nucl.Mater. 348, p.263 (2006)

[12] H.Gleiter, "The Effect of Inclination on Grain Boundary Energies", Acta Metallurgica 18, p.23 (1970)

[13] I Herbuval, M. Biscondi, C. Goux, Mem. Sci. Rev. Met. 70 (1973) 39.

[14] D.M.Saylor, B.S.El Dasher, A.D.Rollett and G.S.Rohrer, "Distribution of Grain Boundaries in Aluminum as A Function of Five Macroscopic Parameters", Acta Materialia 52, p.3649 (2004)

[15] T.Watanabe, S.Tsurekawa, X.Zhao and L.Zuo, "Grain Boundary Engineering by Magnetic Field Application", Scripta Materialia 54, p.969 (2006)

[16] V.Randle, "Twinning-related Grain Boundary Engineering", Acta Materialia 52, p.4067 (2004)

[17] A.Rohatgi, K.S.Vecchio and G.T.Gray III, " The influence of Stacking Fault Energy on The Mechanical Behavior of Cu and Cu-Al Alloys: Deformation Twinning, Work Hardening, and Dynamic Recovery, Metallurgical and Materials Transactions 32A, p.135 (2001)

A. Grain Boundary Engineering of Alloys T91 and HT9

A.1 Overview

As part of the GFR evaluation of metallic components, a study is underway to determine if grain boundary engineering techniques can improve the high temperature creep strength of candidate metals by optimizing grain boundary structural orientations. Progress was made in the following areas: 1) grain boundary engineering of T91 and HT-9, 2) understanding the thermal stability of treatments developed to optimize the grain boundary structure of T91, 3) creep testing of alloy T91 in both the as-received and optimized conditions, and 4) characterization of the microstructure in the as-received, aged, crept and optimized alloy T91.

A.1.1 Optimizing Boundaries in T91 and HT-9

Ferritic-martensitic (F-M) alloys present a unique challenge to coincident site lattice (CSL) enhancement due to their complicated microstructure. Since the microstructural features are important for high temperature strength it is important to have a clear understanding of the microstructure of F-M alloys. T91 is a low carbon, 9Cr-1MoVNb steel that is used in the two phase, ferritic-martensitic structure. The standard heat treatment consists of a solution anneal at 1066°C for 46 min to completely austenitize the microstructure and dissolve the carbides, and a tempering treatment of 790°C for 42 min to relieve the stresses and enhance toughness. The resulting microstructure consists of tempered martensite laths forming subgrains in a ferrite matrix, with (V, Nb) carbonitrides precipitated mainly on dislocations within the subgrains and $M_{23}C_6$ precipitated on the prior austenite grain boundaries (PAGBs) and on subgrain boundaries. The subgrain structure produced by martensitic transformation and the precipitation of carbides and carbonitrides are the primary microstructure features responsible for high temperature creep strength.

Fig. A.1 shows a schematic illustration of the microstructure of T91. The prior austenite grain (PAG) is divided into packets that contain aligned martensite laths. A packet is a region in which the laths are in close crystallographic alignment with the same habit plane and orientation. Most of the PAGBs are randomly oriented, and the martensite-lath boundaries are predominantly small-angle grain boundaries. During tempering carbides and carbonitrides precipitate on the PAGBs and lath boundaries, respectively. Martensite lath boundaries transform into ferrite subgrain boundaries [A.1] (a subgrain is basically a sub-structure within the deforming grain, bounded by dislocation networks and formed due to misorientations). Recrystallization occurs, and equi-axed ferrite grains form at the expense of the original laths. Carbide particles retard grain growth by pinning grain boundaries. Eventually a microstructure of equi-axed grains and spheroidal carbides is produced.

The challenge of CSL-enhancement in T91 is to enhance the grain boundary CSL fraction without disturbing the original microstructure, responsible for high temperature strength. A series of experiments was conducted to identify a treatment to optimize the CSLB fraction in T91, Table A.1. It was observed that the fraction of CSL boundaries in the alloy, T91 can be increased by a thermomechanical process involving a 5 % strain and a heat treatment of 1040°C:1 h + 800°C:0.66 h followed by air cooling, all without changing the microstructural features like hardness, grain size, carbide size, location, and number density [A.2], Table A.2.

Preserving all the microstructural features decisive for high creep strength in T-91, while increasing the fraction of low angle boundaries is expected to increase creep strength.

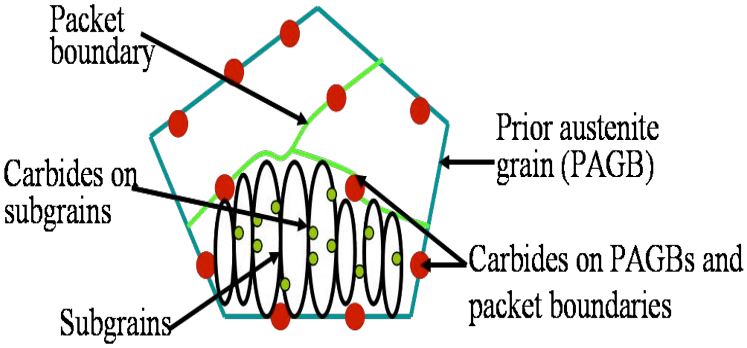
Packet boundary
Prior austenite grain (PAGB)
Carbides on subgrains
Carbides on PAGBs and packet boundaries
Subgrains

Figure A.1 Schematic of the microstructure of T91following solution annealing and tempering.

Such increases in special boundaries have proven effective in reducing creep rates in ferritic and austenitic alloys [A.3-A.4]. The high creep strength of tempered F-M steels results from the presence of a dislocation network of subgrain boundaries (SGBs) that is stabilized by carbides. Thus, subgrain and carbide coarsening cause degradation of high temperature strength. Carbide coarsening at the boundaries depends on grain boundary diffusivity, which is a function of grain boundary structure. Further subgrain coarsening depends on annihilation of grain boundary dislocations and subgrain boundary migration, both of which depend on grain boundary structure. Thus, it is envisioned that an increase in the fraction of special boundaries (with low misorientation angle, thus low diffusivity, energy and mobility) will improve the creep strength.

Due to the complex nature of the microstructure it is important to determine which boundaries are actually modified by CSL-enhancement. As discussed above there are actually three different types of boundaries in the tempered condition of T91; PAGBs, packet boundaries and the subgrain boundaries (Fig A.1). Generally the PAGBs and the packet boundaries have a high misorientation between them and thus are predominantly high angle boundaries [A.5]. The subgrain boundaries are generally the low angle boundaries with small misorientation between them [A.5], and are the ones modified by the CSL-enhancement process. OIM analysis shows an increase in the fraction of Σ1 boundaries from the as-received (AR) condition to the CSLE condition. These boundaries are the subgrain boundaries. Theoretically a Σ1 boundary denotes a perfect (or nearly perfect) crystal; i.e. no boundary at all. However boundaries relatively close to the Σ1 orientation are those with only small misorientations (less than 15°) called "small-angle grain boundaries" - and they are subsumed under the term Σ1 boundaries. The greatest effect of the CSL-enhancement is to increase the fraction of low angle boundaries with misorientation less than 3° over that in the AR samples by about 30%. Fig A.2 shows the distribution of the fraction of Σ1 boundaries in the two conditions with misorientation angle.

Due to the similarity of microstructural features in T91 and HT-9 a similar thermomechanical treatment was applied to HT-9 to successfully increase the fraction of low angle boundaries (Σ1) [A.6]: 5 % strain followed by a heat treatment of 1040°C: 0.5 h + 760°C: 1 h, and an air cool. The fraction of these low angle boundaries with misorientation less than 3° is higher in CSLE samples as compared to AR samples by about 30% (Fig. A.2).

Table A.1 Summary of results of deformation-heat treatment trials to increase the CSL fraction in T91.

Condition: Thermal-Mechanical Processing	CSLB Fraction
As-Received	27.8
5% comp, 800°C, 2h (air cool)	29.7
1050°C, 1h (air cool), 5% comp, 800°C, 2h (air cool)	22.6
1050°C, 1h (air cool), 800°C, 0.66h (air cool)	27.2
13% comp, 1050°C, 1h (air cool), 800°C, 0.66h (air cool)	26.3
8% comp, 1050°C, 1h (air cool), 800°C , 0.66h (air cool)	29.6
5% comp, 1050°C, 1h (air cool), 800°C , 0.66h (air cool)	36.5/35.7

Table A.2 Summary of microstructure for T-91

Property Enhanced	As-Received	CSL
CSL fraction	28%	37%
Grain size	9μm	10μm
Carbide size (diameter) $M_{23}C_6$	0.36 μm	0.37 μm
Linear GB carbide density $M_{23}C_6$	1.8/μm	1.7/μm
Hardness (HRB/HV)	97/225	97/225

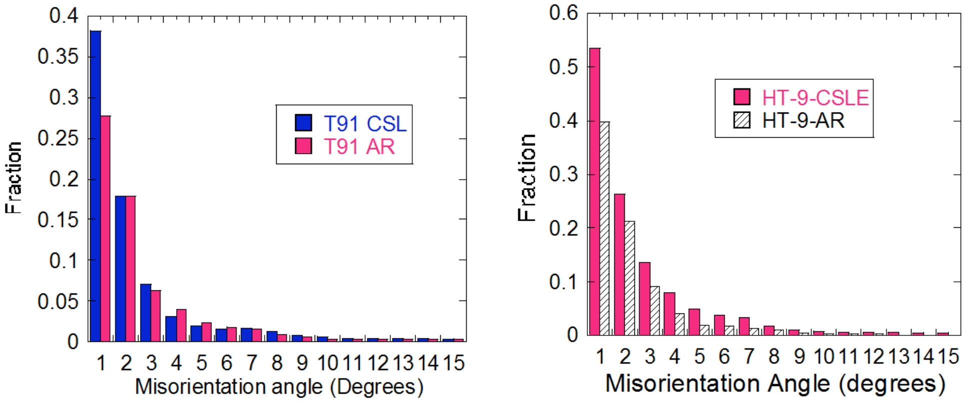

Figure A.2 Plot of fraction of S1 boundary for AR and CSLE condition of T91 for misorientation angle between 0-15°.

A.1.2 Thermal stability of thermo-mechanical treatments for T91

Since the CSL-enhanced alloys are intended for use in components in GFR at high temperature, it is important to verify the stability of these treatments as a function of time-at-temperature. Both AR and CSLE coupons of T91 were exposed at 550 and 600°C for long periods of time to determine whether the CSL fraction is retained. This would indicate if the advantage of GBE treatment would be retainable at high temperature after long exposure times. Fig A.3a shows the plot of the fraction of Σ1 boundaries in both the AR and CSLE samples after exposure at high temperature to different times. At 550°C it is clear that a high fraction of Σ1 boundaries is retained in both the conditions after high exposure to 1000hrs, though there is a slight decrease in the Σ1 boundary fraction in both the conditions after exposure to 2829 hrs, but still the fraction remains higher in the CSLE condition. At 600°C the fraction of Σ1 boundaries is retained up through 500 hr, though further studies need to be done for longer periods of time. Since it's the fraction of Σ1 boundaries with misorientation less than 3° which is the major fraction of these boundaries being higher in the CSLE condition as compared to AR condition, it is important to analyze that separately. This analysis is also important as the overall fraction may remain high but there might be an increase in the misorientation of these boundaries, which would affect their behavior. Fig A.3b shows the plot of the percentage increase of Σ1 boundaries with misorientation less than 3° in CSLE condition as compared to AR condition. It is clear that under all test conditions of exposure at temperature the percentage increase remains stable at around 30%, with a slight decrease after exposure at 550°C for 2829 hrs.

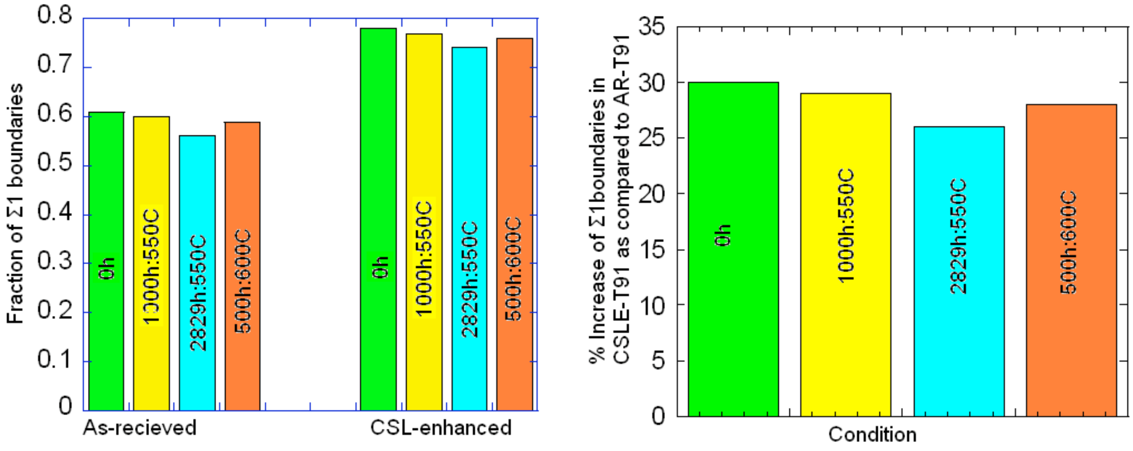

a) b)

Figure A.3 a) Plot of the fraction of S1 boundaries in both the AR and CSLE conditions after exposure at temperature to long periods of time, b) Plot of the increase in fraction of S1 boundaries with misorientation less than 3° in CSLE condition as compared to AR condition after exposure at temperature to long periods of time.

A.1.3 Creep of T91

Tensile bars with a gage length of 21 mm, a gage diameter of 2.2 mm, and a gage thickness of 1.5 mm were used for creep experiments (Fig. A.4a). Figures A.4b and A.4c show the schematic of the compression technique for the deformation step in the CSL-enhancement process. The 5% compressive deformation (5% reduction in thickness) was accomplished by compressing the sample perpendicular to its gauge length between two 14.3 mm square tungsten carbide (WC) blocks (Figure A.4a) using an Instron machine. This deformation step produced two parallel flat surfaces on the initially round in cross section tensile specimens (Fig A.4b).

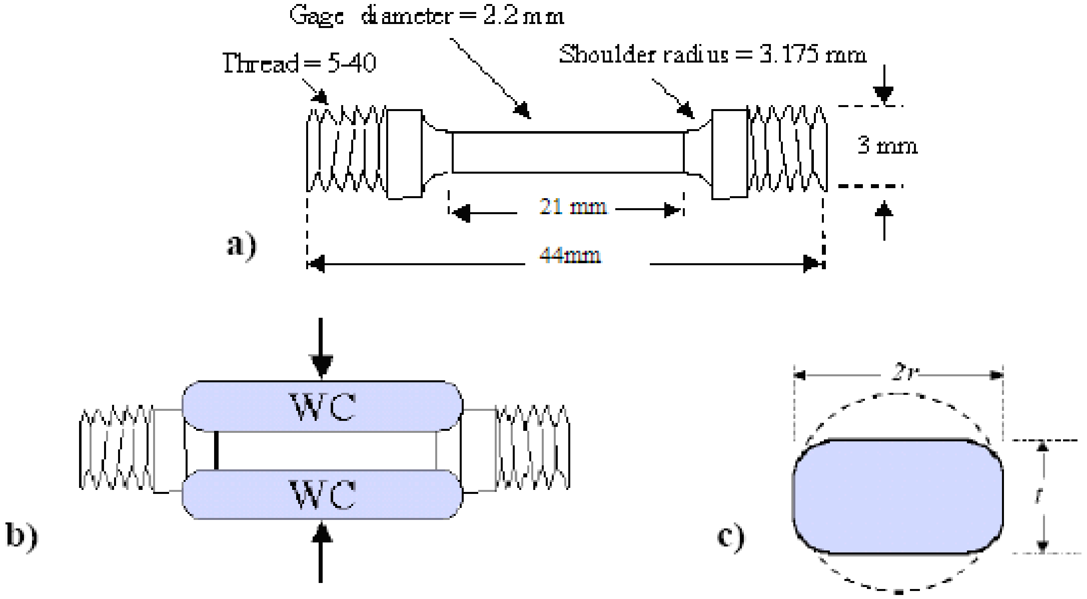

Figure. A.4—a) Dimensions of the as-received tensile specimens, b) schematic illustrating the compression technique, and c) illustration showing the cross-sectional (shaded) area.

Creep experiments were conducted in argon environment on CSLE T91 and AR T91 in the stress range of 140-255 MPa and in the temperature range of 500-600°C. Table A.3 gives results of the all the creep tests conducted on T91. The minimum creep rate for T91 CSLE samples was observed to be less than that of T91 AR samples by a factor of 3-13 [A.7-A.8]. The time to failure (T_f) for AR T91 is greater than that for CSLE T91 for almost every case. Fig A.5 shows a plot of minimum creep rate vs. applied stress for both AR and CSLE conditions at 500-600°C. The plot clearly shows the effect of CSL enhancement in reducing the minimum creep rate of AR T91.

Fig A.6 shows the plots of strain vs. time and strain rate vs. strain for creep tests on samples AR-600-220 and CSLE-600-220. The time to failure is greater for the CSLE condition as compared to the AR condition. Also the slope of the strain vs. time curve is steeper for the AR condition, implying a higher creep rate. Similar behavior was observed under all creep test conditions. Further the creep curve exhibits similar behavior to what has been observed for T91 in the literature. Anderson et al. [A.9], Gianfrancesco et al. [A.10], Ennis et al. [A.11], Eberle et al. [A.12] and Spigarelli et al. [A.13] conducted creep tests on 9Cr-1Mo modified steels at several temperature-stress combinations. T91 exhibits a normal three-stage creep behavior, following a relatively small instantaneous elongation [A.14]. Orlova et al. [A.14], Anderson et al. [A.9], Gianfrancesco et al. [A.10], Eberle et al. [A.12] and Spigarelli et al. [A.13] have shown that a typical creep curve for T91 consists of a primary stage of a decreasing creep rate, a very short secondary region (or rather a minimum creep rate range) followed by a long tertiary stage.

Table A.3 Results for Creep Experiments on AR and CSLE T91

Sample	Min creep rate (s^{-1})	Strain to failure	T_f (hrs)	Sample	Min creep rate (s^{-1})	Strain to failure	T_f (hrs)
AR-500-255	1.34x10^{-7}	0.056	96	CSLE-500-255	6.61x10^{-8}	0.062	154
AR-500-250	1.29x10^{-7}	0.082	160	CSLE-500-250	6.20x10^{-8}	0.072	165
AR-500-245	6.09x10^{-9}	0.031*	666*	CSLE-500-245	2.58x10^{-9}	0.013*	666*
AR-500-235	2.06x10^{-8}	0.080	735	CSLE-500-235	1.57x10^{-9}	0.101	2476
AR-500-220	2.56x10^{-8}	0.005*	242*	CSLE-500-220	6.46x10^{-9}	0.023*	242*
AR-550-245	5.44x10^{-6}	0.125	6	CSLE-550-245	1.75x10^{-6}	0.064	7.5
AR-550-235	7.94x10^{-7}	0.079	21	CSLE-550-235	9.81x10^{-8}	0.064	94
AR-550-220	1.06x10^{-7}	0.088	94	CLSE-550-220	3.01x10^{-8}	0.073	280
AR-550-180	8.67x10^{-9}	0.086	1735	CSLE-550-180	X	X	X
AR-550-165	2.47x10^{-9}	0.019*	2177*	CSLE-550-165	2.57x10^{-9}	0.02*	2829*
AR-550-160	2.49x10^{-9}	0.025*	2829*	CSLE-550-160	1.18x10^{-9}	0.014*	2829*
AR-600-235	2.39x10^{-5}	0.047	0.5	CSLE-600-235	7.56x10^{-6}	0.068	2
AR-600-220	1.41x10^{-5}	0.063	1	CSLE-600-220	2.67x10^{-6}	0.064	5
AR-600-200	4.25x10^{-6}	0.077	3	CSLE-600-200	2.18x10^{-6}	0.081	6
AR-600-180	7.64x10^{-7}	0.085	20	CSLE-600-180	3.45x10^{-7}	0.069	37
AR-600-170	3.33x10^{-7}	0.106	222	CSLE-600-170	1.57x10^{-7}	0.078	63
AR-600-165	3.16x10^{-7}	0.079	44	CSLE-600-165	9.80x10^{-8}	0.099	84
AR-600-160	1.06x10^{-7}	0.089	233	CSLE-600-160	X	X	X
AR-600-155	5.03x10^{-8}	0.084	293	CSLE-600-155	2.14x10^{-8}	0.079	545
AR-600-150	2.57x10^{-8}	0.098	660	CSLE-600-150	2.08x10^{-9}	0.034*	1678*

Sample designation scheme: (alloy condition- temperature-stress)

- - Test not conducted to failure;, X - Test not conducted for that condition as yet.

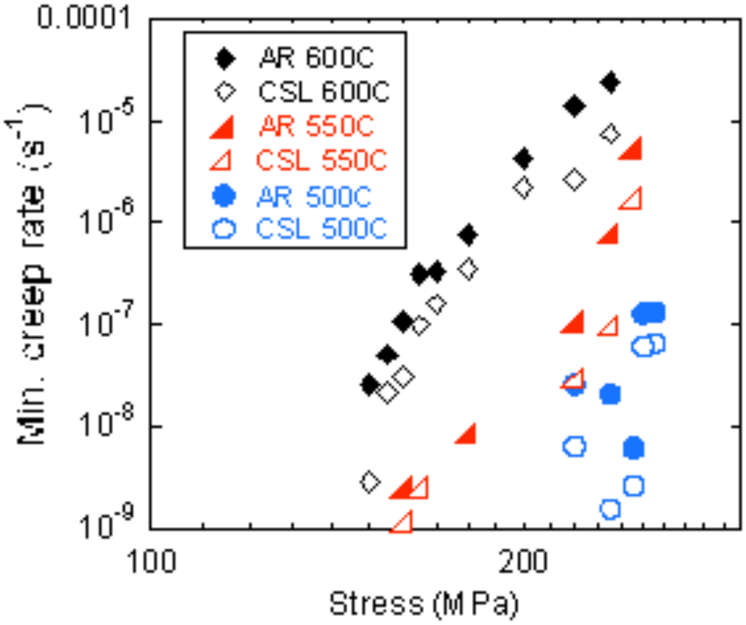

Figure A.5 Plot of minimum creep rate vs. applied stress for creep tests done at 500-600°C on both AR and CSLE T91.

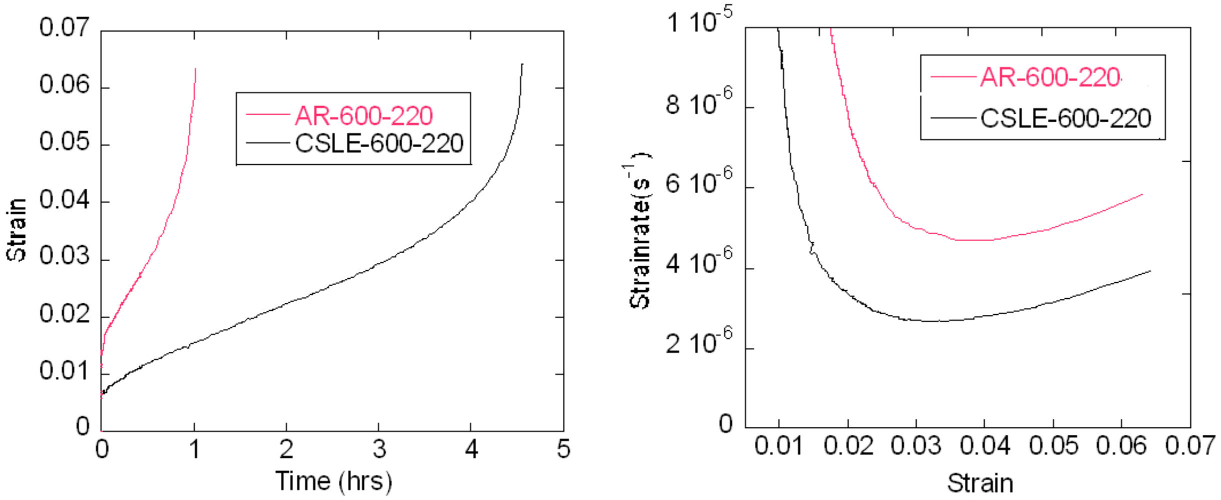

a) b)

Figure A.6 Plot of a) strain vs. time and b) strain rate vs. strain for creep test on samples AR-600-220 and CSLE-600-220.

A.1.3 Microstructural investigation of as-received, aged, crept, and optimized alloys T91

Characterization of the microstructure was performed on the virgin material, aged samples and samples used in creep experiments, for both the as-received and CSL-enhanced conditions on alloy T91 to understand the reasons for the creep behavior. Carbide size on PAGB and subgrain size were measured for each condition listed in Table A.4. Creep tests on samples AR-550-165 and CSLE-550-165 were conducted to a strain of 0.02 (but for different times), while creep tests on samples AR-550-160 and CSLE-550-160 were conducted for the same duration of time (2829 hrs) but to different strains. Further creep tests on samples AR-600-155 and CSLE-600-155 were conducted to the point of fracture (thus different time duration and strain). Samples AR-550 and CSLE-550, and samples AR-600 and CSLE-600 were exposed for the same duration of time.

Table A.4 Quantitative micorstructural parameters for T91 in different conditions

Sample	Carbide size $M_{23}C_6$ (nm)	Subgrain size (μm)	Test Duration (hrs)
AR	360±15	0.57±0.10	NA
CSLE	370±20	0.55±0.10	NA
AR-550-165	570±23	1.20±0.10	2177
CSLE-550-165	560±14	1.18±0.10	2829
AR-550-160	615±18	1.50±0.10	2829
CSLE-550-160	535±21	1.25±0.10	2829
AR-550	540±15	0.90±0.10	2829
CSLE-550	490±16	0.80±0.10	2829
AR-600-155	X	0.96±0.10	294
CSLE-600-155	X	0.80±0.10	545
AR-600	420±17	0.68±0.10	500
CSLE-600	395±13	0.63±0.10	500

Sample designation scheme: crept samples (condition-temperature-stress)
: aged samples (condition-temperature)
NA - Not applicable
X - No measurement performed.

Subgrain growth is a function of strain, and since the microstructure for the two conditions under the same stress and temperature would be expected to be similar at similar strain, subgrain sizes are compared for samples AR-550-165 and CSLE-550-165. The two samples had similar subgrain sizes after creep tests (Fig A.7). It is important to note here that the sample CSLE-550-165 took an additional 650hrs to get to the same subgrain size, indicating a lower coarsening rate in that condition. The sample AR-550-160 has more coarsening than sample CSLE-550-160 by 50% (Fig A.8), again indicating a higher coarsening rate in that condition. Further the subgrain coarsening rate is higher in samples AR-550-160 and CSLE-550-160 as compared to samples AR-550 and CSLE-550 respectively, implying that coarsening is accelerated during creep. Samples AR-550 and AR-600 have a higher subgrain coarsening than samples CSLE-550 and CSLE-600 respectively, indicating a higher coarsening rate in the as-received condition. One important point to note is that the subgrain size in the virgin material was approximately equal in both the conditions.

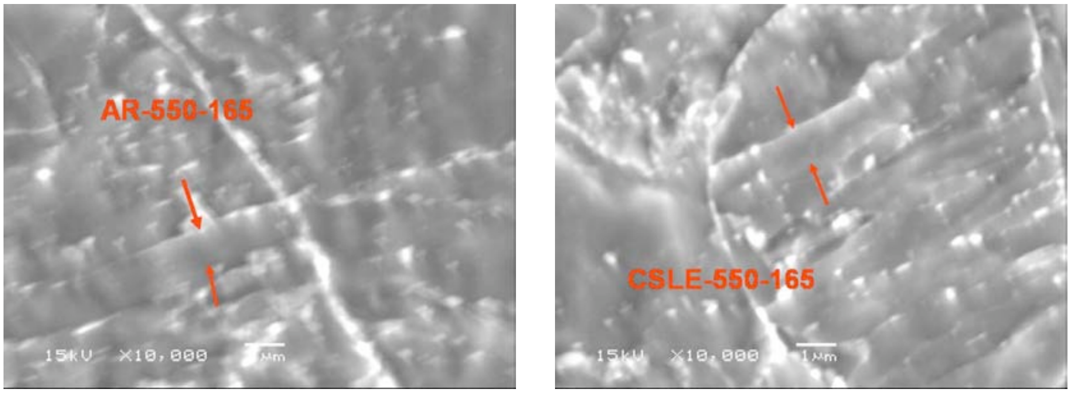

a) b)

Figure A.7 SEM images of subgrains for samples a) AR-550-165 and b) CSLE-550-165.

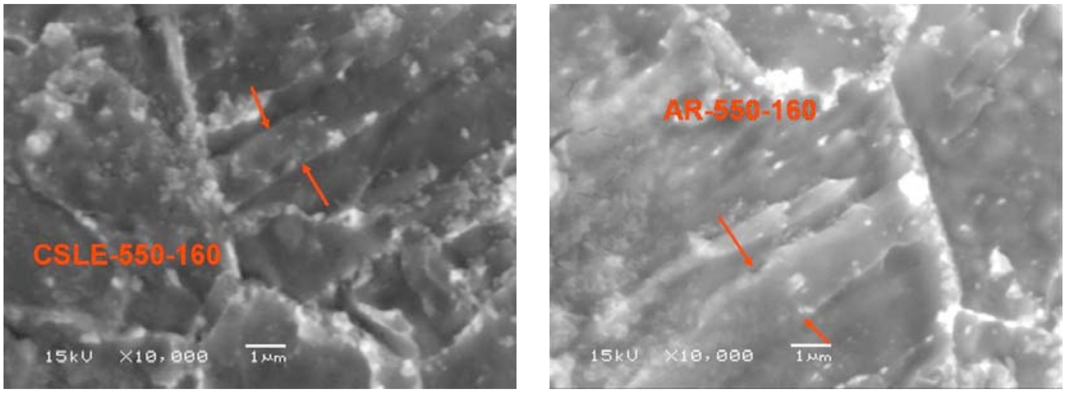

a) b)

Figure A.8 SEM images of subgrains for samples a) AR-550-160 and b) CSLE-550-160.

The increase in subgrain width during creep has been attributed to the annihilation of mobile dislocations in the lattice (subgrain) with dislocations at the subgrain boundaries. Sawada et al. [A.15] described the increase in lath width due to migration of lath boundaries and also unknitting of the dislocations that form lath boundaries. He conducted in-situ experiments during tempering to show the migration of the lath boundary and reasoned that the driving force was strain accumulated during martensitic transformation. The same mechanism governs coarsening during creep. Igarashi et al. [A.16] described creep deformation due to annihilation and rearrangement of excess dislocations inside the lath-martensite, which causes coarsening of the lath and the formation of equi-axed subgrains. Maruyama et al. [A.17] explained two main processes which cause the recovery of the subgrain structure: a) disappearance of a sub-boundary by annihilation of dislocations constructing the sub-boundary and, b) mutual annihilation of two sub-boundaries with opposite sign. Both of these processes are diffusion controlled.

Since carbide coarsening is a function of time at temperature, carbide sizes were compared for the samples aged and used in creep tests for the same duration of time: samples AR-550-160 and CSLE-550-160, samples AR-550 and CSLE-550 and samples AR-600 and CSLE-600. Carbide sizes at PAGBs were observed to be bigger in sample AR-550-160 as compared to sample CSLE-550-160 by 15% (Fig A.9), by 10% in sample AR-550 as compared to sample CSLE-550 and by 6.5% in sample AR-600 as compared to sample CSLE-600 (Fig A.10), indicating a higher rate of coarsening in the as-received conditions. This also shows that coarsening is accelerated with creep, similar to what has been observed by Eggeler et al [A.18].

Note that since the exposure times at the two different temperatures (550°C and 600°C) are not the same, it is not possible to determine the role of temperature in coarsening. Further carbide sizes on PAGBs are approximately similar for samples AR-550-165 and CSLE-550-165, though the later sample was exposed to much longer times. It is important to note here that the carbide size at PAGBs were similar in the virgin material for both the conditions.

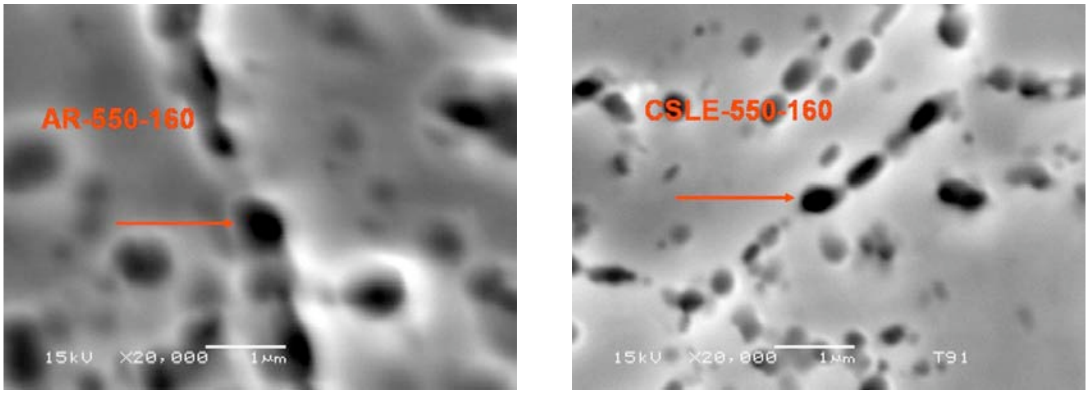

a) b)

Figure A.9 SEM images of carbides at PAGBs for samples a) @-AR-550-160 and b) @-CSLE-550-160.

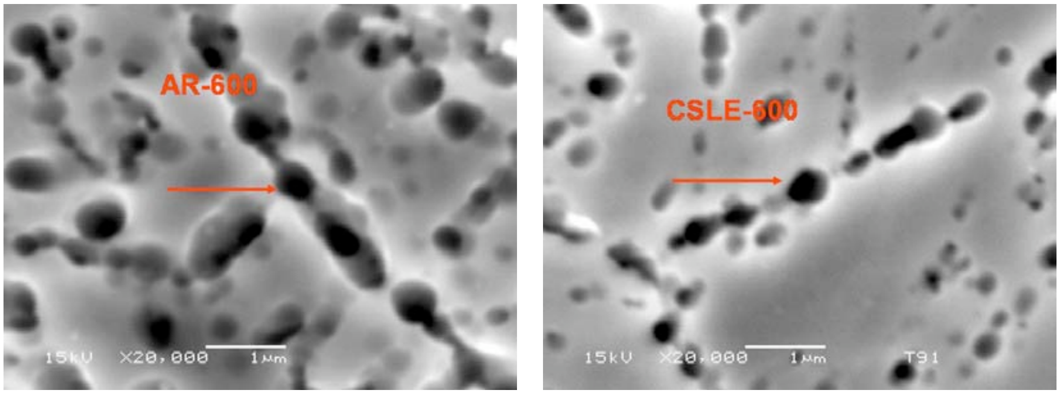

a) b)

Figure A.10 SEM images of carbides at PAGBs for samples a) AR-600 and b) CSLE-600.

The improved creep behavior of grain boundary engineered T91 is attributed to the reduced subgrain and carbide coarsening in the optimized alloy after creep testing. The coarsening of subgrains by the migration of subgrain boundaries by absorbing excess dislocations causes creep deformation [A.19], while the carbide particles retard the recovery of subgrain structure during creep deformation and improve creep properties [A.1]. Thus, the ability to maintain a small subgrain size pinned by carbides for long times at high temperature and stress is important for high creep strength [A.1]. Subgrain boundaries consist of dislocation networks which, compared with the subgrain interiors are hard regions in the microstructure of ferritic steels. A small subgrain is equivalent to a high volume fraction of hard regions in the microstructure, and could thus be expected to give rise to high creep strength [A.20-A.22]. Once formed, the boundaries of the subgrains lead to hardening as they induce long-range internal back stresses in the interior of the subgrains by forcing the mobile dislocations to take a bowed configuration [A.23]. Preliminary investigations have shown a higher internal stress for the CSLE condition as compared to the AR condition, leading to reduced effective stress for creep and thus lower creep rates [A.7-A.8].

Huang et al [A.24] studied subgrain growth and low angle boundary mobility. They observed that subgrain growth tends to be discontinuous (certain subgrains may grow faster than others) and that discontinuously growing subgrains are generally more highly misoriented to their surroundings than the slower growing subgrains. Also boundary mobilities were found to increase rapidly with increasing misorientation. Since there is a higher fraction of low angle boundaries with low misorientation in the CSLE condition as compared to the AR condition the coarsening of subgrains would be less in CSLE condition as compared to the AR condition and this has been also observed experimentally. Since the smaller subgrains result in increased creep strength, the higher creep strength of the CSLE condition is understandable.

A.2 Future Work

- Since subgrain and carbide coarsening takes place after a considerable period of time during creep, but the difference in creep rates between the two conditions (AR and CSLE) are observed from time zero onwards under all test conditions, it implies that there is some other factor which governs creep strength. One major difference is in the structure of the boundaries in the two conditions, which can affect the rate of annihilation and production of dislocations necessary for creep deformation. Thaveeprungsriporn and Was [A.25] hypothesized that the reason for the difference in creep behavior of alloys containing high fractions of CSLBs is due to the difference in dislocation absorption at CSLBs versus high angle boundaries (HABs). The authors suggested that the increased structural order and reduced free volume of the CSL boundaries inhibits dislocation motion by vacancy diffusion and climb, as well as the absorption and dissociation of extrinsic dislocations in these boundaries. Thus, it seems sensible to measure the dislocation density in the two conditions both prior to and after a short-term creep test.
- CSL-enhancement can be viewed as a benefit in terms of temperature increment to achieve the particular minimum creep rate. That is, the CSLE condition will yield the same creep strength as an AR sample but at a higher temperature. For example calculations have shown that that the minimum creep rate for the AR condition at 200MPa:500°C can be achieved with the same applied stress at 542°C for the CSLE condition. Thus, the temperature benefit of the CSLE condition is 42°C. To understand this effect at higher temperatures it is important to understand the thermal stability of this treatment at longer times at 600°C and also to check it at 650°C. These are the temperature of interest at which components made from these alloys would be used in service.
- It would be valuable to perform additional microstructural characterization on all samples used in creep tests to measure subgrain and carbide size to obtain a relation for the coarsening behavior to be able to link it quantitatively to creep strength.
- Though F-M alloys are considered to be resistant to stress corrosion cracking (SCC), HT-9 has exhibited evidence of IG cracking in argon and supercritical water. Thus, it might be interesting to observe whether GBE is useful in mitigating SCC.
- Initiate studies of the effect of GBE on impact properties

A.3 References

[A.1] K.Iwanga and S.Takaki, Key Engineering Materials Vols. 171-174 (2000) pp. 477-482.
[A.2] G.Gupta, G.S.Was, B.Alexandreanu, "Grain Boundary Engineering of Ferritic-Martensitic alloy T91," Journal of Metallurgical and Materials Transactions A, Vol. 35A, No. 2, pp. 717-719, 2004.
[A.3] B.W.Bennett and H.W.Pickering: Metallurgical Transactions. A, 18A (1987), pp.1117-1124.
[A.4] T.Watanabe: J.De.Physique, 5, (1998), pp. 555-564.
[A.5] K.Kaneko et al, Materials Science and Engineering A 374 (2004) 82-89.
[A.6] G.Gupta, G.S.Was, T.R.Allen, P.Ampornrat, "Role of Grain Boundary Engineering in Mitigating Stress Corrosion Cracking of HT-9 in Supercritical Water," Journal of Nuclear Materials, submitted.
[A.7] G.Gupta, G.S.Was "The Role of Grain Boundary Engineering on the High Temperature Creep of Ferritic-Martensitic Alloy T91," Journal of ASTM international, March 2005, Vol.2, No.3.
[A.8] G.Gupta, G.S.Was, "Interpretation of Improved Creep Properties of a 9Cr-1Mo-Nb- V (T91) Steel by Grain Boundary Engineering," TMS Letters, 2005, vol. 2, Issue 3, p.g 71-72.
[A.9] P.Anderson, T.Bellgardt and F.L.Jones, Materials science and Technology, Feb 2003, Vol. 19, 207-213.
[A.10] Correlation between Microstructural Evolution and Creep Response in 9Cr-1Mo and 9Cr-1Mo-NbVW Heat-Resistant steels, A.DI Gianfrancesco, O.Tassa and S.Spigarelli*. Centro Sviluppo Materials S.p.A., Roma, Italy, * INFM/Department of Mechanics, University of Ancona, Italy, Modelling of Microstructual Evolution, 161-175.
[A.11] P.J.Ennis and A.Czyrska-Filemonowicz, OMNI (Vol 1, No. 1) April 2002.
[A.12] N.Eberle and F.L.Jones, Materials science and technology, Feb 2003, Vol 19, 214-218.
[A.13] S.Spigarelli, E.Cerrie, P.Bianchi and E.Evangelista, Materials science and technology, Dec 1999, Vol. 15, 1433-1440.
[A.14] A.Orlova, J.Bursik, K.Kucharova, V.Sklenicka: Materials Science and Engineering A245 (1998), pp.39-48.
[A.15] K.Sawada et al, Material Science and Technology June 2003, Vol. 19 739-742.
[A.16] Igarashi et al, ISIJ International, Vol 41 (2001), supplement, pp. S101-S105.
[A.17] Maruyama et al, ISIJ International, Vol 41 (2001), No 6, pp. 641-653.
[A.18] G.Eggeler, Acta Metall. Vol. 37, No 12, pp. 3225-3234.
[A.19] Fujio Abe, Metallurgical and Materials Transactions; Apr 2003; 34A, 4; Research Library pg. 913.
[A.20] Oleg D.Sherby, Metallurgical Transactions A, Vol. 8A, June 1977-843.
[A.21] M.E.Kassner, Mat. Res. Soc.Symp.Proc.Vol.362, 1995 Materials Research Society, 157-162.
[A.22] John Hald, ISIJ International, Vol. 43 (2003), No. 3, pp. 420-427.
[A.23] R.Sedlacek, W.Blum and S.Forest, Metallurgical and Materials Transactions, Bol 33A, Feb 2002-319.
[A.24] Y.Huang et al, Acta Mater. 48 (2000) 2017-2030.
[A.25] V.Thaveeprungsriporn and G.S.Was, Metall.Trans.A 28A (1997) 2101-2112.

B. Grain Boundary Engineering of Alloy 800H

B.1 Overview

Alloy 800H is a candidate for high temperature application in many Generation IV systems. Two experimental programs were carried out in Alloy 800H. The first was a study of the ability to control grain boundary character distributions as a potential improvement to the mechanical property and corrosion resistance of 800H. The second was to gain basic information on the microstructural stability of 800H under radiation.

B.1.1. Materials and Methods

Grain boundary engineering (GBE), proposed by Watanabe in the early 1980s [B.1], was employed to promote a high proportion of coincidence site lattice boundaries (CSLBs) to potentially improve the mechanical properties of 800H. The material used in this study was commercial INCOLOY alloy 800H with measured chemical composition (in wt.%): 45.26 Fe, 31.59 Ni, 20.42 Cr, 0.76 Mn, 0.57 Ti, 0.50 Al, 0.42 Cu, 0.13 Si, 0.069 C, 0.014 P, and 0.001 S. The as-received alloy was annealed at 1177 °C for 24 minutes per centimeter of thickness followed by water quench.

The study of the grain boundary character distribution (GBCD) was performed in a LEO 1530 FEGSEM with the TSL orientation imaging microscopy (OIM) system MSC2200. The SEM was operated at 20kV and the automatic electron backscatter diffraction (EBSD) scan was performed over an area of 660×1230 μm^2 using a hexagonal grid with a step size of 2.5 μm. The number of scanned grains is about 150 for different samples, which provides relatively good quantitative statistical analysis. To allow identification of the phases present with the EBSD analysis software, a crystallographic data file was established by X-ray diffraction analysis. For phase analysis with EBSD, a voting scheme and the confidence index (CI) established by TSL were used [B.2]. A high number of votes and higher CI values indicate a higher possibility that the phase is correctly identified.

B.1.2. Optimizing grain boundaries in alloy 800H

One cycle thermomechanical processing, strain followed by annealing, was employed in this study to ensure the minimum grain size requirement of alloy 800H, ~60 μm [B.3, B.4]. The samples were subjected to a thickness reduction of 6.6±0.2% before annealing at 1050°C. The annealing temperature, which is 127°C lower than the annealing temperature of as-received material, was selected to keep properties such as hardness, yield strength and elongation similar to the as-received alloy [B.3]. Different annealing times, 20, 45, 90, 120 and 150 minutes, were conducted to investigate the effect of annealing time on GBE. The seven types of samples are denoted as as-received, 6.6%, 1050C20, 1050C45, 1050C90, 1050C120, and 1050C150 in this report.

B.1.2.1 Coincidence Site Lattice Boundaries (CSLBs)

To determine whether a measured boundary can be classified as CSLBs, the Brandon criterion [B.5] was used as the allowable deviation from the exact orientation relationship. This states that the maximum allowable misorientation ($\Delta\theta$) from the exact CSL relationship is $\Delta\theta = \theta_m\Sigma^{-1/2}$, where θ_m is the maximum misorientation angle for a low angle boundary (typically 15°). EBSD area scans of the 6.6%, 1050C90 and as-received samples are shown in Fig. B.1 (a), (b) and (c), respectively. The GBCD with Σ3 highlighted can be observed in this figure, showing Σ3 boundaries were strongly promoted by the thermomechanical processing. In addition, the grain size of the 6.6% sample was increased by annealing. Quantitative results of the low-Σ CSLBs frequency of three typical samples (6.6%, 1050C90 and as-received) are shown in Fig. B.2. For statistical analysis, a total grain boundary length of 29±3 mm was obtained by selecting an appropriate area on the EBSD scan map of each sample. Fig. B.2 shows that the Σ3 frequency of 59% for the 1050C90 sample is significantly increased as compared to that of 12% and 36% for the 6.6% and as-received samples, respectively. Meanwhile, the $\Sigma3^n$ (Σ9 and Σ27) frequencies are also increased due to thermomechanical processing. For the other four types of samples, the quantitative results of Σ3 frequency show an increase within short-time annealing (e.g. 20, 45, 90 minutes), and decrease after long-time annealing (e.g. 120, 150 minutes). In contrast, the frequency of low-angle GBs (Σ1) is very high for the deformed sample (6.6%), and decreases within short-time annealing and increases after long-time annealing. Similar frequencies for Σ1 and Σ3 were observed for the as-received sample.

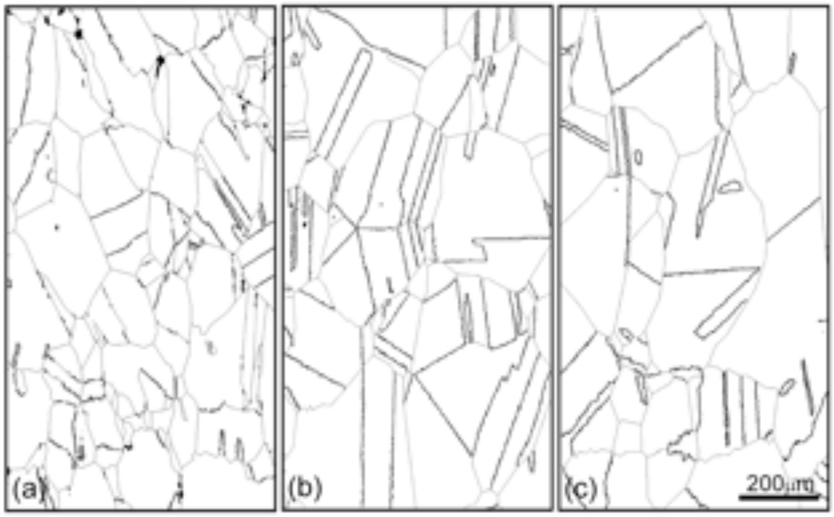

Fig. B.1. EBSD area scans of (a) 6.6%, (b) 1050C90, and (c) as-received samples, where GBs are in gray lines and Σ3 boundaries are highlighted. The black spots in (a) are unindexed indicating the accumulation of deformation-induced defects such as dislocations.

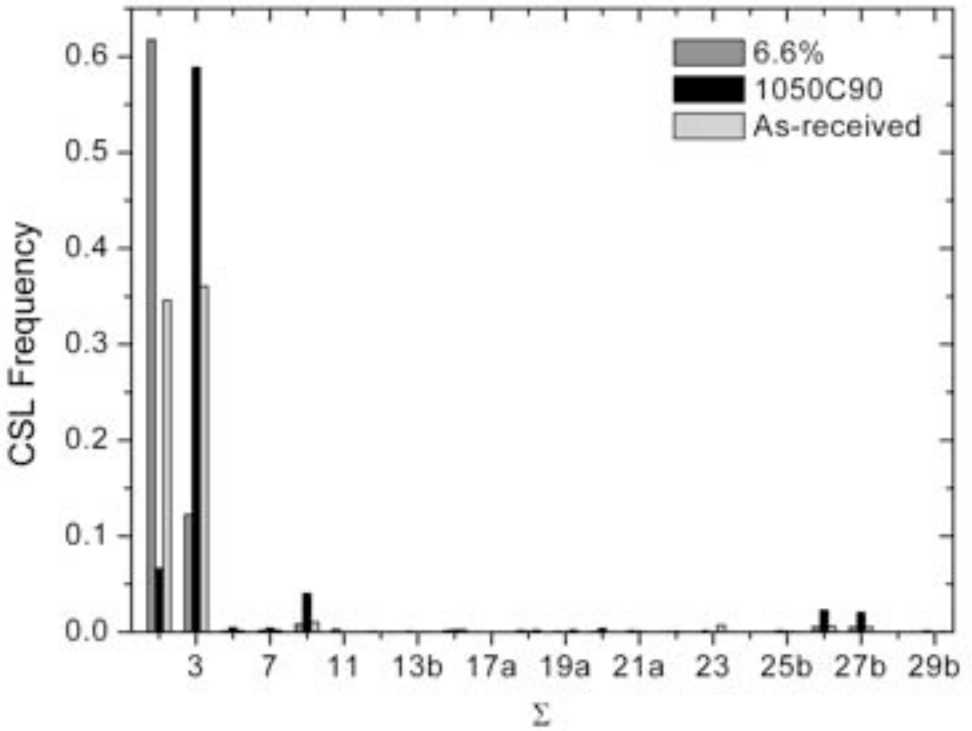

Fig. B.2. CSL frequency as a function of Low-Σ CSLBs (Σ≤29b) of 6.6%, 1050C90 and as-received samples.

B.1.2.2 Misorientation

GBE appears to produce materials with decreasing deviations from exact Σ misorientation [B.6]. Since Σ3 boundaries are mainly correlated with property improvement [B.7], deviations from the exact Σ3 misorientation are worthy of studying to evaluate the GBE effect. As shown in Fig. B.3, sample 1050C90 with the highest Σ3 frequency displays the smallest deviation from exact Σ3 while samples 1050C150 and 6.6% with low Σ3 frequency show high deviations, indicating two extreme situations for GBE of alloy 800H. Similar phenomenon, that the Σ3 frequency evolves towards a more exact Σ3 misorientation during annealing, was also observed by Thomson *et al* [B.8].

GBCD evolution during annealing of deformed material can be also indicated by the frequency of GBs versus the misorientation angle, as shown in Fig. B.4. The GBCD can be simplified by setting a misorientation angle of 15° as a division between low- and high-angle boundaries, which keeps the same angle as that defined in the Brandon criterion. The simplified GBCD of different samples is shown as an inset in Fig. B.4. The 6.6% and 1050C90 samples possess the smallest and the largest fraction of high-angle boundaries, respectively, while the other five types of samples possess medium fraction of high-angle boundaries.

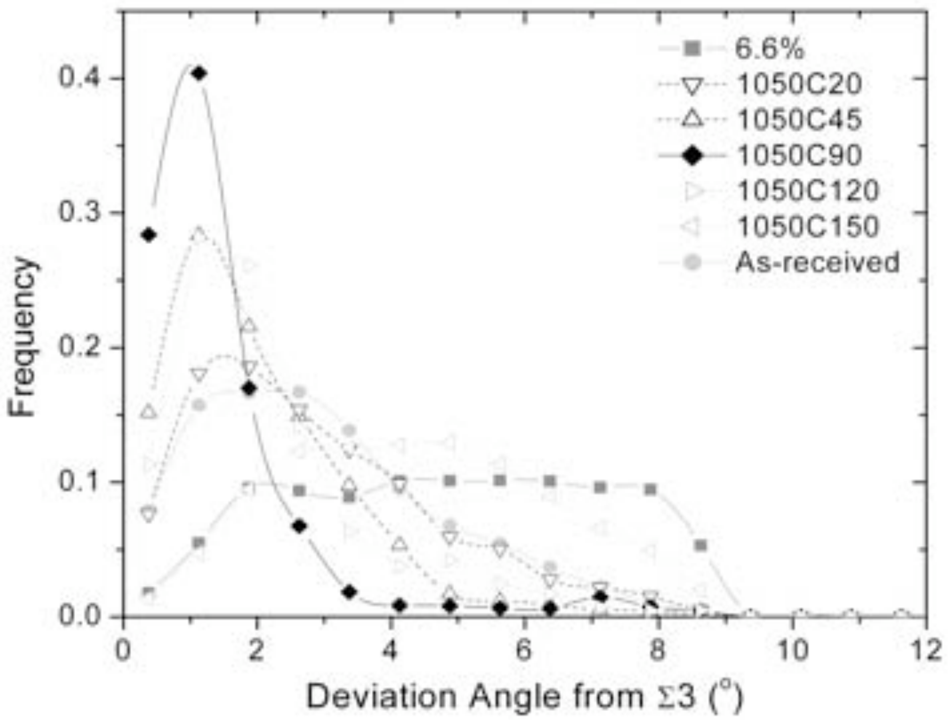

Fig. B.3. The frequency of CSLBs deviating from exact Σ3.

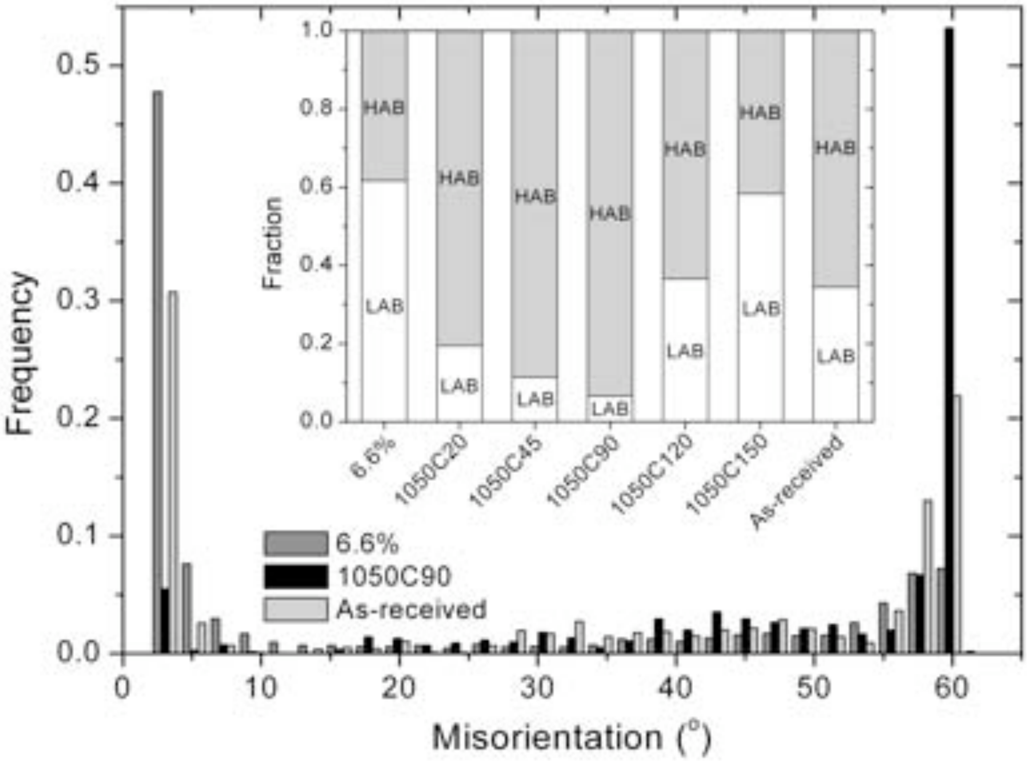

Fig. B.4. GBCD of the EBSD area scans of 6.6%, 1050C90 and as-received samples. The inset indicates the fractions of low-angle boundaries (LAB) and high-angle boundaries (HAB) for seven types of samples.

B.1.2.3 Grain Size

Fig. B.1 indicates that grain size increased during annealing. To obtain a reliable grain size value, coherent-twins were removed from EBSD scan data because they are immobile and not a constituent of the intergranular transport network. Low-Σ boundary frequency as a function of grain size is plotted in Fig. B.5. The grain size of the deformed sample (6.6%) is less than 60 μm, and grain size increases with annealing time. As shown in Fig. B.5, the frequency of low-Σ CSLBs increases significantly with small grain growth. Alloy 800H annealed at 1050ºC is mainly composed of austenite that should have some carbides and nitrides precipitates as suggested by Ref. [B.3]. When the grain size increase associated with annealing is so large that sufficient solute or precipitates accumulate at GBs, an associated reduction of GB mobility and increase of GB energy [B.9] occurs, leading to a decrease in thefrequency of low-Σ CSLBs with excessive grain growth. Therefore, minimizing excessive grain growth during thermomechanical processing is important for the retention of a high frequency of low-Σ CSLBs. For alloy 800H, large grain size contributes to strength and resistance to creep and rupture at high temperatures. However, excessive grain growth can lower the toughness after exposure to elevated temperature.

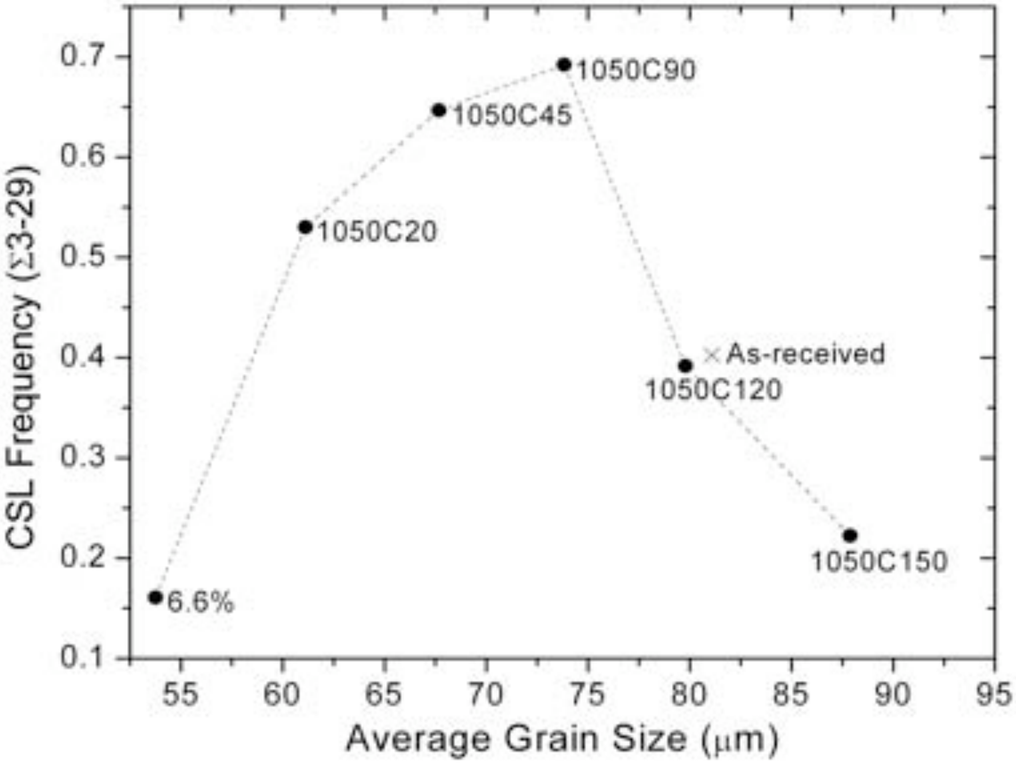

Fig. B.5. CSL frequency as a function of average grain size of INCOLOY alloy 800H.

B.1.2.4 Verification and Comparison

Due to the dominant effect of Σ3 boundaries as part of the low-Σ CSLB structure, Palumbo and co-workers studied the twin-limited microstructure [B.9-B.112]. By using the upper and lower limits for annealing twin contributions to the frequency of low-Σ CSLBs [B.11], and the theoretical twin limit (2/3) [B.12], a triangle can be sketched as shown in Fig. B.6. The annealed alloy 800H samples (1050C20, 1050C45 and 1050C90) fall into this triangle, while 6.6% and as-received samples, and the samples with excessive grain growth after long-time annealing (1050C120 and 1050C150) fall out of this triangle and below the lower limit. For comparison, the data of INCOLOY alloy 800 [B.9] are also included in Fig. B.6. Most of the alloy 800 data close to the upper limit indicate that the alloy 800 was strongly GB engineered. The strong GBE potential of alloy 800 is because there is no grain size limitation for alloy 800, which generally have a much smaller grain size than alloy 800H. Materials with smaller initial grain size produce a higher frequency of low-Σ CSLBs [B.9, B.13].

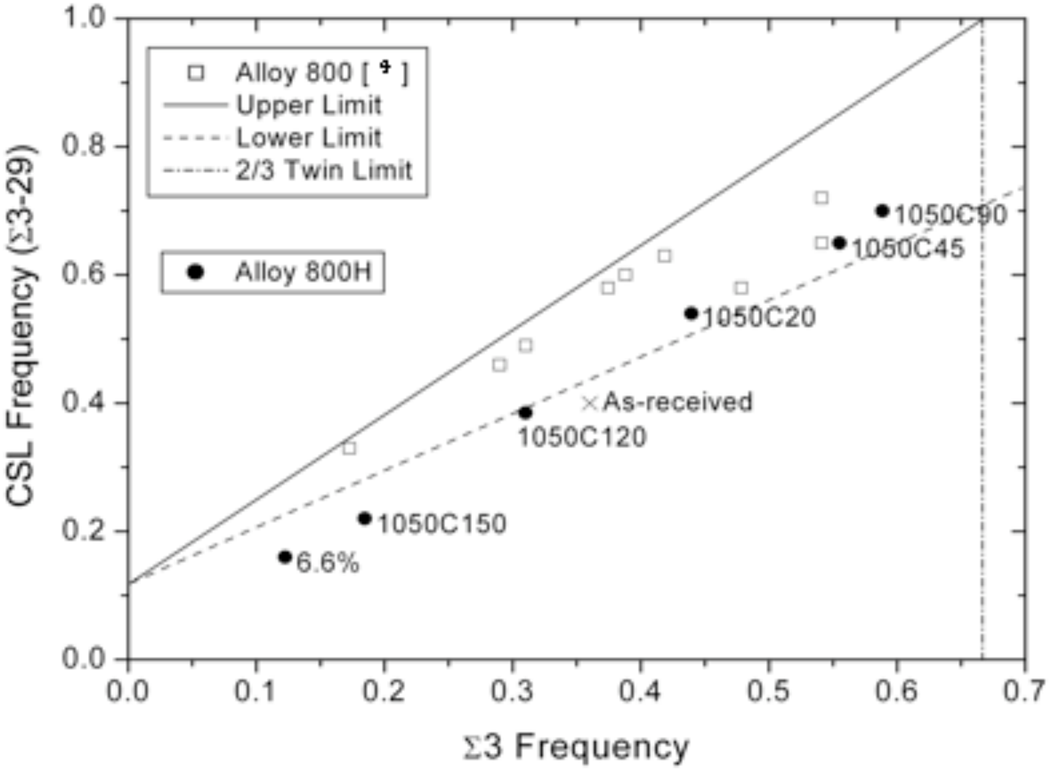

Fig. B.6. CSL frequency as a function of annealing twin (Σ3) frequency.

B.1.2.5. Hardness

The effect of annealing time on the Vicker's hardness was evaluated with a micro-hardness tester equipped with a Vicker's indenter at a load of 1000gf. The Vicker's hardness of the deformed sample (6.6%) and the five GBE-treated samples (1050C20, 1050C45, 1050C90, 1050C120 and 1050C150) are plotted in Fig. B.7 compared to that of the as-received sample. The deformed sample has very high hardness with a large deviation due to the stored deformation energy inhomogeneously distributed in material. The Vicker's hardness decreases with the annealing time. The GBE-treated sample 1050C90 has hardness comparable with as-received sample.

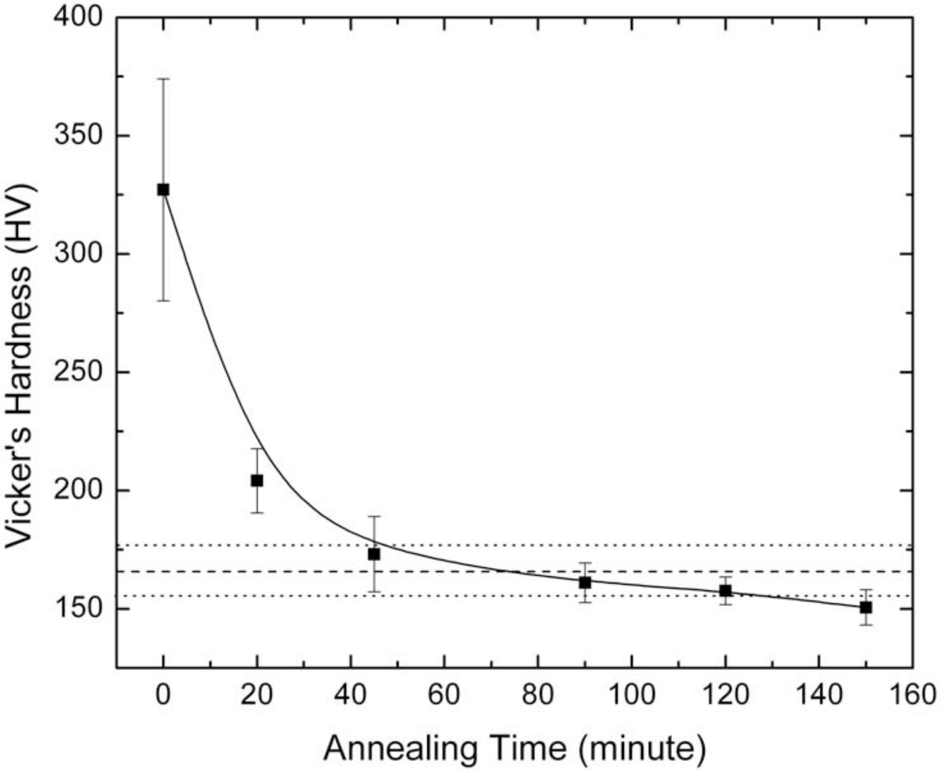

Fig. B.7. The effect of the annealing time on the Vicker's hardness of deformed (6.6%) and GBE-treated (1050C20, 1050C45, 1050C90, 1050C120 and 1050C150) samples. The Vicker's hardness of the as-received sample is plotted in a dash line with standard deviation in dot lines.

B.1.2.6. Thermal Stability of GBE

GBE treatment has the ability to effectively improve the population of CSLBs which has potential benefit for many properties, e.g. creep, stress corrosion cracking, etc. To maintain the benefits, the thermal stability of the population of CSLBs is an important factor when the parts are employed at high temperature. Since the INCOLOY alloy 800H is designed to be used at temperatures up to 760°C, thermal stability of GBE-treated samples was tested at three temperatures, i.e. 500°C, 600°C and 760°C, in air for ~675 and ~1004 hours. As-received samples were also tested at the same time for comparison.

The results of the GBE thermal stability, specifically the evaluation of the number fraction of CSLBs and high-angle boundaries (HABs), are shown in Fig. B.8. The higher number fraction of CSLBs and lower number fraction of HABs are preferred according to the concept of GBE. As shown in Fig. B.2, the fraction of CSLBs and HABs of as-received samples was not significantly affected by the annealing. For GBE-treated samples, annealing at 500°C did not affect the fraction of CSLBs and HABs. In contrast, annealing at 600°C and 760°C decreased the CSLBs fraction to a similar level, about 20% lower than the CSLBs fraction of as-GBE-treated sample and about 10% higher than that of as-received sample. The HABs fraction of GBE-treated samples annealed at 600°C is similar to that of as-GBE-treated sample. However, annealing at 760°C significantly increased the HAB fraction similar to the as-received sample. In addition to the annealing temperature effect on the thermal stability of GBE, longer annealing time generally impairs the effect of GBE.

As will be explained in Section C on Alloy 617, the stability of GBE treatments is dependent on the distribution of special boundaries so the possibility exists that improved high-temperature stability of 800H may still be achievable.

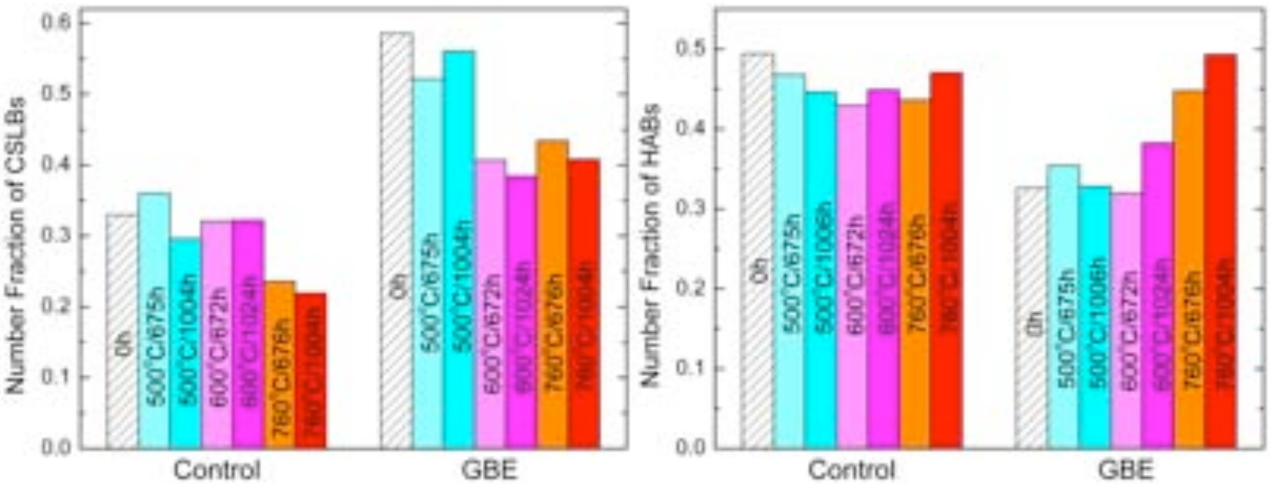

Fig. B.8. Number fraction of coincidence site lattice boundaries (CSLBs) and high angle boundaries (HABs) of as-received and GBE-treated (1050C90) samples prior to annealing (0 hour) and annealing at 500°C, 600°C and 760°C for ~675 and ~1004 hours.

B.1.3. Grain Boundary Composition

A PHI 670 scanning Auger electron spectroscope (AES) was used to analyze microchemistry at interfaces such as grain boundaries. AES sample bars of dimension 2mm × 1mm × 20mm were fabricated from as-received and GBE-treated materials. To promote intergranular fracture, sample bars were cut with a small notch on one surface and cathodically charged with hydrogen in a solution of 0.1N sulphuric acid with the addition of As_2O_3 as a poison for the recombination of hydrogen. Sample bars were fractured in situ at a pressure lower than 1×10^{-9} Torr by bending with a special fracture stage attached to the Auger vacuum chamber. Once the fracture was achieved, a secondary electron image of the fracture surface was obtained to identify the areas of the sample that failed intergranularly. Analyses in an area of about 1 μm^2 were performed on grain boundary facets and areas of ductile fracture for comparison. Auger spectra from 30–1000 eV were recorded from every point analyzed at a beam energy of 10 keV. Results of chemical composition are reported as atomic concentration calculated following Davis et al [B.14]. Sensitivity factors of iron, chromium, and nickel have been obtained by comparing calculated concentration at the ductile areas of as-received sample to the bulk composition of the material.

Typical fracture features, i.e. intergranular (IG) and ductile (D), of as-received and GBE-treated samples are shown in Fig. B.9. Black precipitates in sizes up to ~10 μm were observed on both intergranular and ductile features of the as-received and GBE-treated samples.

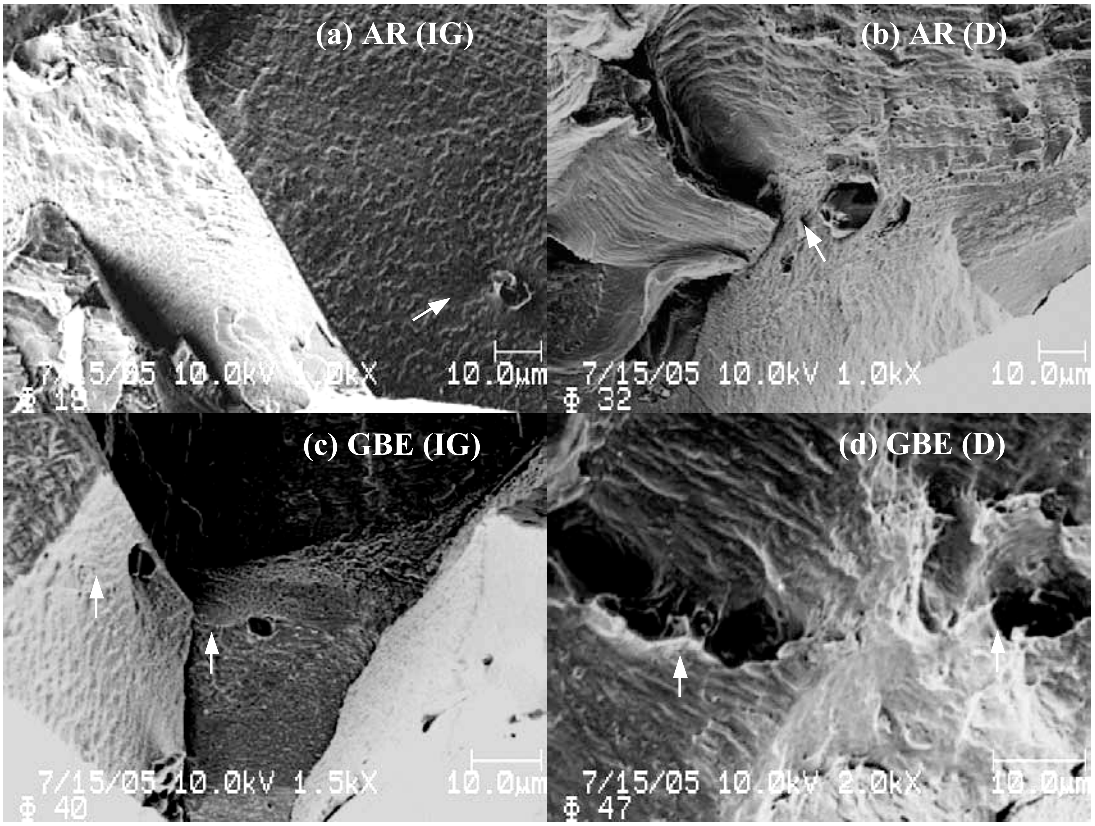
(a) AR (IG)
7/15/05 10.0kV 1.0kX 10.0µm
Φ 18
(b) AR (D)
7/15/05 10.0kV 1.0kX 10.0µm
Φ 32
(c) GBE (IG)
7/15/05 10.0kV 1.5kX 10.0µm
Φ 40
(d) GBE (D)
7/15/05 10.0kV 2.0kX 10.0µm
Φ 47

Fig. B.9. SEM images of fractured features, i.e. intergranular (IG) and ductile (D), in as-received (AR) and GBE-treated samples. Particles noted with white arrows are present on both intergranular and ductile features.

Auger surface surveys were performed on the intergranular and ductile fractured features. Similar spectra were obtained for both as-received and GBE-treated samples. Typical Auger spectra at intergranular and ductile features on the fractured surface of GBE-treated sample are shown in Fig. B.10. It is clear that the major components, i.e. Fe, Ni, and Cr, are well identified at ductile features as shown in Fig. B.10(a). In addition to the major components, Ti and C with noticeable peak-to-peak height are identified at intergranular features as shown in Fig. B.10(b). P was also observed on some intergranular features. Typical Auger spectrum of the particles, corresponding to the features noted with white arrows in Fig. B.9, are shown in Fig. B.10(c). The precipitates are titanium carbide.

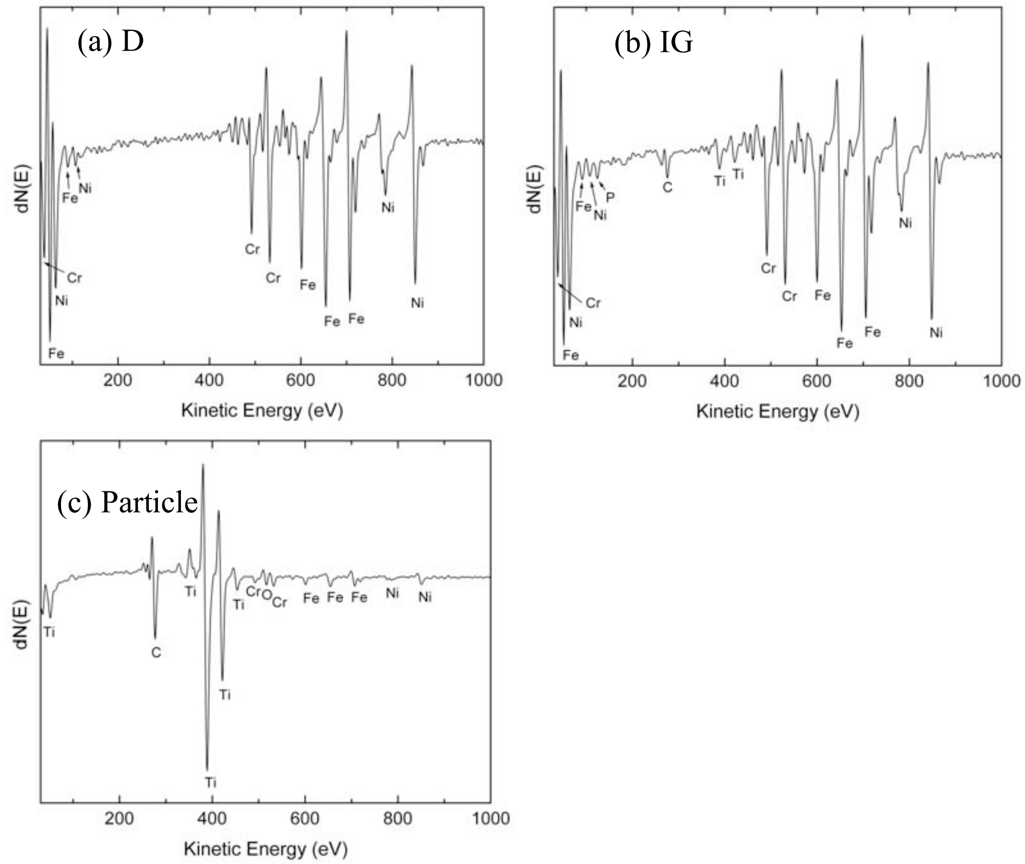

Fig. B.10. Typical Auger spectra obtained from features observed on fractured surface of GBE-treated sample: (a) ductile (D), (b) intergranular (IG), and (c) particle in Fig. B.8 pointed with white arrows.

Atomic concentrations at intergranular and ductile features on fractured surface were obtained based on semi-quantitative Auger analyses. More than 15 different locations on each fractured feature were analyzed to make the data more statistically representative. Atomic concentrations of the as-received and GBE-treated samples at the intergranular features on fractured surfaces are summarized in Table B.1. The atomic concentration of Ti and C was calculated from the sensitivity factors of Ti and C assuming the particles are stoichiometric TiC. P is not included in Table 1 because it was not detected at all intergranular features.

Table B.1. Atomic concentrations of major components at the intergranular (IG) and ductile (D) features on fractured surface.

Sample		Fe	Ni	Cr	Ti	C
As-received	D	46.2±0.2	31.5±0.5	22.3±0.4		
	IG	38.0±1.9	27.6±1.3	21.6±.0.7	3.0±0.8	9.7±2.0
GBE-treated	D	45.5±0.2	31.5±0.5	23.0±0.3		
	IG	36.8±2.5	26.4±2.2	22.1±1.8	4.0±1.0	10.7±2.6

The atomic concentration difference between the intergranular and ductile features for Fe, Ni, Cr, Ti and C of the as-received and GBE-treated samples is shown in Fig. B.11. Fe and Ni are depleted while Ti and C are enriched at intergranular features. Cr is slightly depleted at intergranular features. In many steels with grain boundary precipitates, Cr enrichment occurs at intergranular features due to the formation of chromium carbides, e.g. $Cr_{23}C_6$ or Cr_7C_3. With the addition of titanium into this alloy, titanium preferentially grabs carbon compared to chromium due to the lower Gibbs free energy of TiC. Fig. B.11 shows disproportional enrichment of C compared to Ti, which indicates some other types of carbides may exist at grain boundaries, e.g. chromium carbides. But it is more possible that the extra enrichment of C comes from the contamination from the AES chamber. The contamination intensity of C generally increases with the extension of the exposure time after in-situ fracture. A similar phenomenon is the O intensity variation due to the contamination. The atomic concentration of the components in GBE-treated sample shows slightly larger deviation compared to that in as-received sample. This study indicates that GBE-treated sample has component segregation behavior similar to as-received sample. The GBE treatments do not appear to change typical grain boundary chemistry.

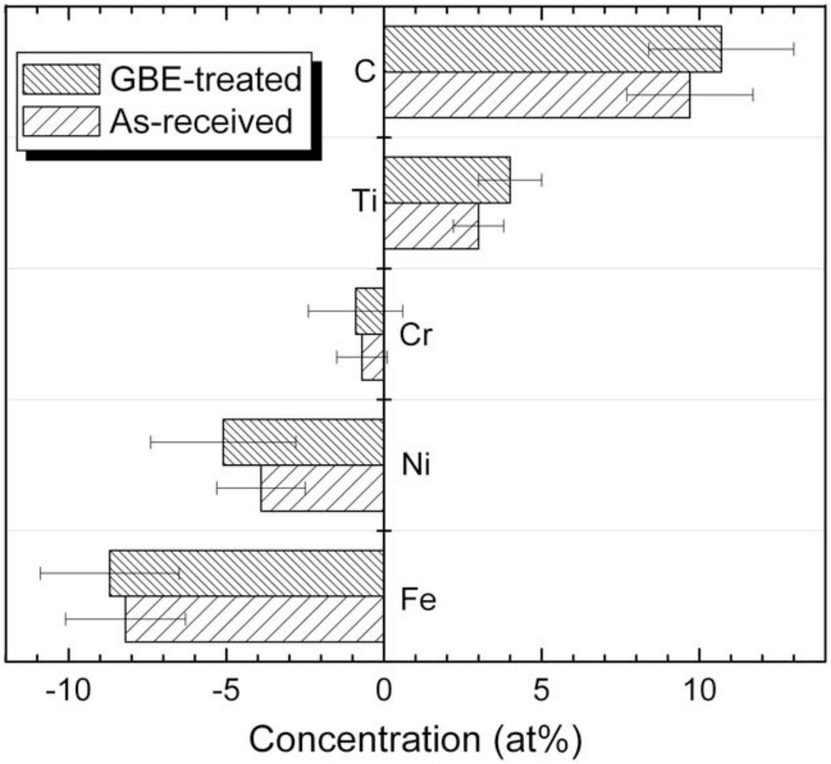

Fig. B.11. Atomic concentration difference between the intergranular and ductile features for Fe, Ni, Cr, Ti, and C.

B.1.4. Specimen Preparation for Mechanical Tests

Two types of specimens were prepared to verify the mechanical performance of the GBE-treated 800H compared to as-received 800H. One is a round cross-section as shown in Fig. B.12(a), and the other is in rectangular cross-section as shown in Fig. B.12(b). Creep testing is being performed at the Pacific Northwest National Laboratory (PNNL) at 525°C on the specimens with round cross-section. Creep specimens were fabricated from alloy 800 in standard condition and in a grain boundary engineering condition. One specimen of each condition was placed in series in a dead weight creep test frame with a three-element clamshell furnace. The temperature of each specimen was individually monitored with a thermocouple placed within 5 mm of the specimen. The specimens were loaded to 175 MPa and heated to 525°C in air. The furnace was periodically shutdown and the length of the specimens was measured. After seven months at these conditions, no appreciable creep deformation had occurred. The load has been increased to 225 MPa, and testing is underway again

Tensile tests will be performed on the specimens with rectangular cross-section at the Oak Ridge National Laboratory (ORNL), including samples irradiated at 750°C and 900°C. The HFIR irradiations were completed in the summer of 2006 and testing will occur later in 2006.

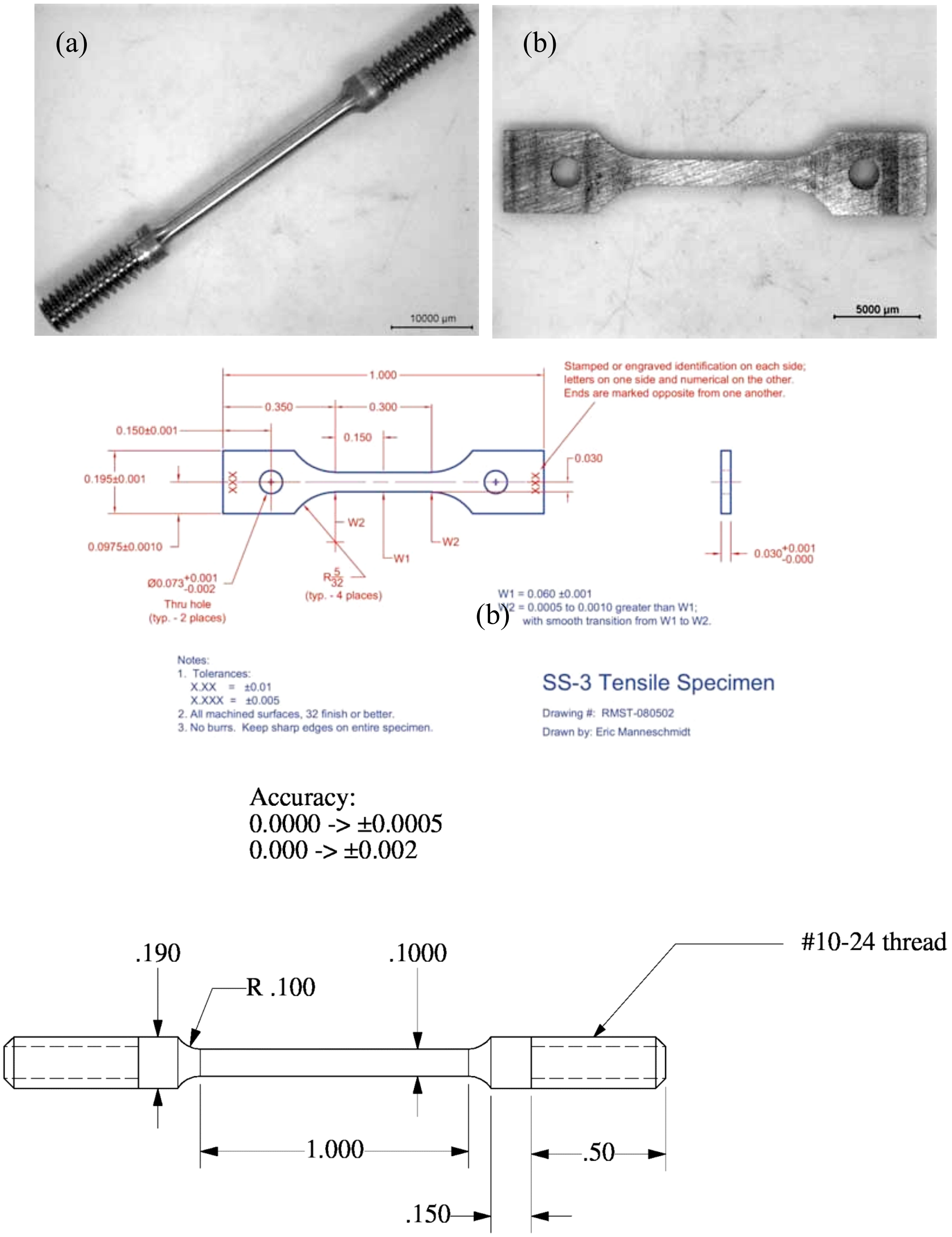
(a)
(b)
10000 µm
5000 µm
1.000
0.350
0.300
0.150±0.001
0.150
0.195±0.001
0.0975±0.0010
0.030
XXX
W2
W1
W2
Ø0.073 +0.001 -0.002
Thru hole
(typ. - 2 places)
R 5/32
(typ. - 4 places)
0.030 +0.001 -0.000
Stamped or engraved identification on each side; letters on one side and numerical on the other. Ends are marked opposite from one another.
W1 = 0.060 ±0.001
W2 = 0.0005 to 0.0010 greater than W1; with smooth transition from W1 to W2.
(b)
Notes:
1. Tolerances:
X.XX = ±0.01
X.XXX = ±0.005
2. All machined surfaces, 32 finish or better.
3. No burrs. Keep sharp edges on entire specimen.
SS-3 Tensile Specimen
Drawing #: RMST-080502
Drawn by: Eric Manneschmidt
Accuracy:
0.0000 -> ±0.0005
0.000 -> ±0.002
.190
.1000
R .100
#10-24 thread
1.000
.50
.150

Fig. B.12. Optical images of (a) mechanically machined creep test specimen with round cross-section, and (b) wire-EDM (Electro-Discharge Machine) fabricated tensile test specimen with rectangular cross-section. The design of the tensile specimen (b) and the creep specimen (a) are also shown.

B.2. Supercritical Water (SCW) Exposure

Altering the grain boundary structures is expected to change the ability of metallic materials to resist unstable oxidation. While waiting for high-temperature environmental chambers to be constructed to test alloy 800H in high-temperature flowing gas, the effect of GBE on corrosion was examined by exposing coupons to supercritical water. Control (cut from annealed material) and GBE-treated (thermomechanical-processed) samples were polished to 1 μm finish prior to exposure in SCW with 25 ppb (part per billion) dissolved oxygen at conditions of 500°C and 25 MPa for exposure times to 1026 hours.

Gravimetry and optical topographical microscopy results showed that extensive oxide spallation occurred on the control samples but not on the GBE-treated samples. Oxide spallation is generally caused by stress generation in an oxide scale. There are generally two types of stresses in oxide scale: growth stress (also called intrinsic stress) developed during the oxidation process, and thermal stress developed on cooling due to the different thermal expansion between the oxide scale and the metal substrate. Although the origin of the growth stress is complex, it is strongly affected by the crystal structures, the oxide/metal volume ratio (also called Pilling-Bedworth ratio [B.15]), and the growth behavior of the oxide.

Since the austenite substrate has the same FCC structure as that of magnetite and spinel [B.16], and because magnetite and hematite have a similar Pilling-Bedworth ratio [B.17], the effect of crystal structure and volume of oxide and metal on growth stress is likely to be negligible. Therefore, for alloy 800H the growth stress is mainly affected by growth behavior of the oxide. To understand the growth behavior of the oxide, oxide texture was analyzed based on the EBSD data. Inverse pole figures (IPF) of magnetite and hematite on 3C and 4G samples, as shown in Fig. B.14, were used as examples to show the oxide texture for the control and GBE-treated samples, respectively. According to the specimen layout during EBSD analysis, which is schematically shown in Fig. B.13(c), the directions parallel to the oxide growth and oxide surface are defined as TD [010] (transverse direction) and RD [100] (rolling direction), respectively. As shown in Fig. B.14, both magnetite and hematite have texture on 3C and 4G samples along the TD [010] and RD [100] directions. However, the oxide texture intensity (defined as the ratio of measured intensity to the intensity of a random orientation) on the 3C sample is stronger than that on the 4G sample, as can be noted on the corresponding texture intensity scale bar.

The maximum texture intensities of magnetite and hematite on the 3C and 4G samples along the TD [010] and RD [100] directions are plotted in Fig. B.15 for comparison. The control sample (3C) had stronger texture than the GBE-treated sample (4G), and the hematite texture was greater than the magnetite texture. For the 3C sample, the texture along the RD [100] direction was stronger than that along the TD [010] direction, especially for hematite texture in which the texture intensity along RD [100] direction was about 3 times of that along TD [010] direction. In contrast, the texture intensity along the RD [100] and TD [010] directions for the 4G sample was similar. These results indicate that the oxide formed in the 3C sample was more anisotropic than that in the GBE-treated 4G sample.

It has been reported that anisotropic energy of grain boundaries results in anisotropic texture development [B.18,B.19]. In addition, grain boundary energy is related to growth stress (intrinsic stress) [B.20]. It is suggested that the strong anisotropic oxide texture, especially that of hematite as shown in Fig. B.15, developed on the control samples may anisotropically increase the growth stress and thus promote oxide scale cracking and spallation. GBE tunes the grain boundary character distribution, and thus the grain boundary energy distribution. Grain boundaries with relatively isotropic energy may be promoted after thermomechanical processing, which results in an oxide growth favoring improved spallation resistance. Therefore, the lower level of oxide spallation that occurred on the GBE-treated samples may be attributed to the relatively isotropic oxide texture. Moreover, the smaller hematite grain size on GBE-treated samples as shown in Fig. B.13 could alleviate growth stress buildup [B.21] and thus benefit spallation resistance.

In addition to growth stress, thermal stress could be also alleviated in GBE-treated samples. This is because the thermal expansion of hematite is approximately a linear function of temperature, but the thermal expansion of magnetite is similar to that of hematite as a function of temperature up to ~300°C and then increases with temperature [B.22]. The thermal expansion difference between hematite and magnetite at temperature above ~300°C can be reduced by the higher hematite fraction in the oxide on GBE-treated samples.

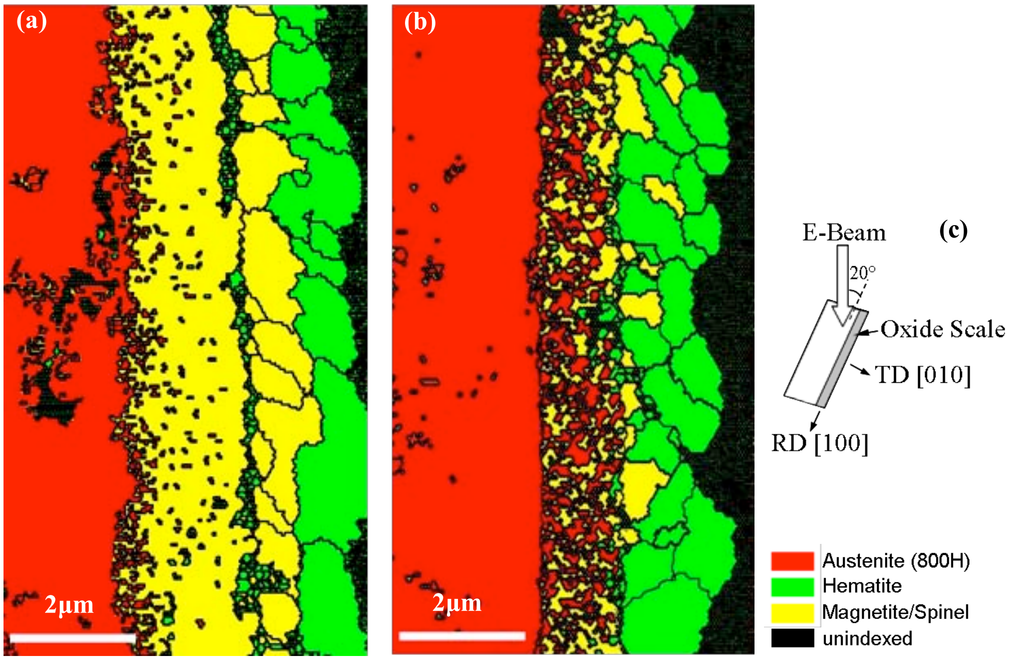

Fig. B.13. EBSD scanning map of (a) 3-week SCW-exposed control (3C) and (b) 4-week SCW-exposed GBE-treated (4G) samples. The specimen layout during EBSD analysis is schematically shown in (c) with the direction of TD [010] and RD [100] parallel to oxide growth and oxide surface, respectively.

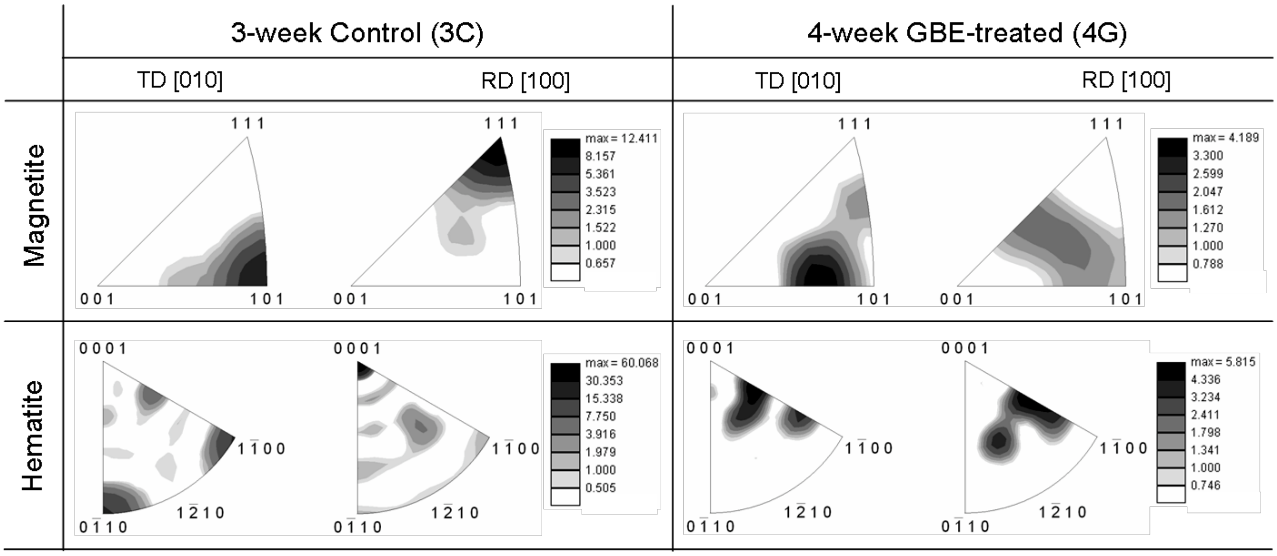

Fig. B.14. Inverse pole figures (IPF) of magnetite and hematite in ~3-week SCW-exposed control (3C) and ~4-week SCW-exposed GBE-treated (4G) samples along the direction parallel to oxide growth (TD [010]) and oxide surface (RD [100]). The contrast of the IPFs indicates corresponding texture intensity scale as shown in the legend.

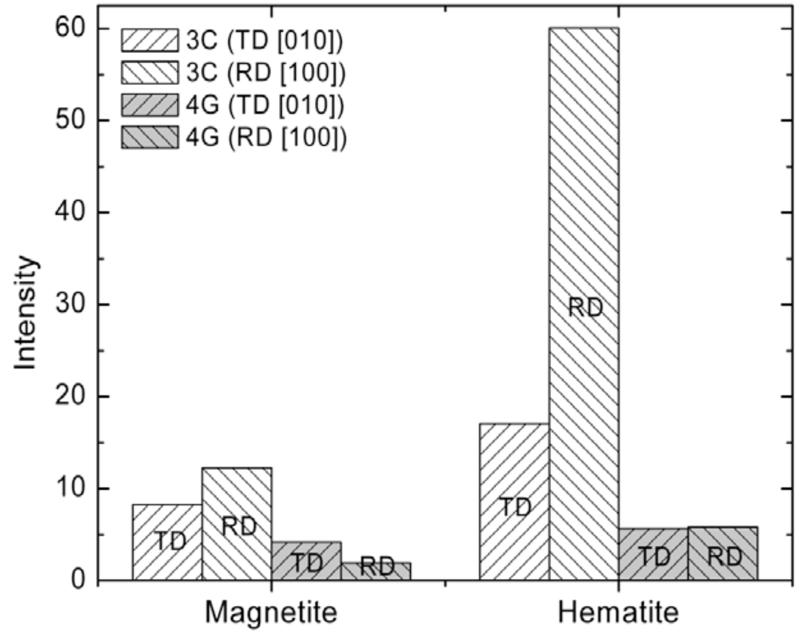

Fig. B.15. Maximum texture intensity (defined as the ratio of measured to random orientation) of magnetite and hematite on 3-week SCW-exposed control (3C) and 4-week exposed GBE-treated (4G) samples along the direction parallel to oxide growth (TD [010]) and oxide surface (RD [100]).

B.3 Future Work

- The thermal stability GBE-treated samples is being tested to understand the limits of stability of the GBE treatments.
- Determining if GBE-treatment stability can be improved by adjusting initial boundary character needs to be pursued
- The limits of improved oxide stability using the GBE-treated 800H need to be further studied
- Creep and tensile testing of GBE-treated 800H needs to be completed
- Initiate studies of the effect of GBE on impact properties

B.4 References

[B.1] T. Watanabe: *Res. Mechanica*, 1984, vol. 11, pp. 47-84.
[B.2] D.P. Field: *Ultramicroscopy,* 1997, vol. 67, pp. 1-9.
[B.3] INCOLOY alloy 800H & 800HT, Technical Bulletin, Special Metals Publication SMC-047, March 2004. (http://www.specialmetals.com)
[B.4] V. Randle: *Acta Mater.*, 1999, vol. 47, pp. 4187-96.
[B.5] D.G. Brandon: *Acta Metall.*, 1966, vol. 14, pp. 1479-84.
[B.6] A.J. Schwartz, W.E. King: *JOM*, 1998, vol. 50, pp. 50-55.
[B.7] V. Randle: *The role of the coincidence site lattice in grain boundary engineering*, The Institute of Materials, London, 1996, pp. 7, 91.
[B.8] C.B. Thomson, V. Randle: *Acta Mater.*, 1997, vol. 45, pp. 4909-16.
[B.9] C.G. Rhodes, and A.W. Thompson, Metallurgical Transactions A, 8A (1977), 1901
[B.10] G. Palumbo, K.T. Aust. In: H. Weiland, B.L. Adams, A.D. Rollett (Eds.): *The 3rd International Conference on Grain Growth (ICGG-3)*, The Minerals, Metals & Materials Society, Pittsburgh, PA, USA, June 1998, pp. 311-20.
[B.11] P. Lin, G. Palumbo, K.T. Aust: *Scripta Mater.*, 1997, vol. 36, pp. 1145-9.
[B.12] G. Palumbo, K.T. Aust, U. Erb, P.J. King, A.M. Brennenstuhl, P.C. Lichtenberger: *Phys. Status Solidi A*, 1992, vol. 131, pp. 425-8.
[B.13] T. Watanabe. In: U. Erb, G. Palumbo (Eds.). *Grain Boundary Engineering: A Symposium in Honor of Dr. K.T. Aust*, CIM, Canada, 1993, pp. 57.
[B.14] Davis, L. E. MacDonald, N. C., Palmberg, P. W., Riach, G. E. and Weber, R. E., *Handbook of Auger Electron Spectroscopy,* Physical Electronics Industries, Eden Prairie, MN, 1976.
[B.15] N.B. Pilling, R.E. Bedworth, The oxidation of metals at high temperatures, J. Inst. Metals 29 (1923) 529-534.
[B.16] The JCPDS Powder Diffraction File (PDF), International Centre for Diffraction Data (ICDD).
[B.17] P.R. Roberge, Handbook of Corrosion Engineering, McGraw-Hill, New York, 2000. p.233.

[B.18] N.M. Hwang, B.J. Lee, C.H. Han, Texture evolution by grain growth under a system of anisotropic grain boundary energy, Scripta Mater. 37 (1997) 1761-1767.

[B.19] N. Ma, A. Kazaryan, S.A. Dregia, Y. Wang, Computer simulation of texture evolution during grain growth: effect of boundary properties and initial microstructure, Acta Mater. 52 (2004) 3869-3879.

[B.20] H. Sankur, W.J. Gunning, J.F. DeNatale, Intrinsic stress and structural properties of mixed composition thin films, Applied Optics 27 (1988) 1564-1567.

[B.21] W. Gao, Z. Li, Nano-structured alloy and composite coatings for high temperature applications, Mater. Res. 7 (2004) 175-182.

[B.22] Thermophysical Properties of Matter, Thermophysical Properties Research Center (TPRC), 1970.

C. Grain Boundary Engineering of Alloy 617

C.1. Overview

Research to optimize the grain boundary distributions in alloy 617 proceeded in parallel at both Michigan and Wisconsin. Two different lots of 617 were used and optimization processes were developed independently. A first approach investigated treatments using a single compression and annealing step. The second approach investigated multi-step compression and annealing treatments.

C.1.1 Single compression and annealing treatments

Various thermomechanical treatments were performed on a first lot of alloy 617 to determine the optimal treatment to use to enhance the CSLB fraction in the alloy. The annealing temperatures for these treatments ranged from 900˚C to 975˚C and the compression treatments ranged between 3% and 9%. The full set of treatments performed and the resulting CSLB fractions are listed in Table C.1. The optimized treatments are highlighted in gray. The two measures used to quantify the CSLB fraction in the alloy were the total CSLB fraction and the CSLB fraction after the twin boundary contribution was subtracted from the total.

Orientation imaging microscopy (OIM) scans on the as-received 617 were performed to determine the initial CSLB fractions of the alloy. The only CSLBs observed were the Σ3, Σ9, Σ27a, and Σ27b boundaries; the contribution of the other CSLBs were below the detection limit. It was determined that the as-received material had a total CSLB fraction of 42% (58% HAB) and that if the contribution of the Σ3 twin boundaries was removed, this percentage was reduced to 26% (74% HAB).

The thermomechanical treatments that used annealing temperatures of 925˚C and 950˚C resulted in the most substantial CSLB enhancement. The annealing temperature proved to be the most important parameter in determining the type of CSLB enhancement that occurred in the specimens. Compressing the samples by 5% and annealing the sample at 925˚C for 7.5 minutes did not result in a very substantial increase in the total CSLB fraction (43% CSLBs), but it did produce a very substantial increase in the CSLB fraction when the twin contribution was eliminated (37% CSLBs). Therefore, the samples annealed at 925˚C, contained fewer twins, but more Σ3 boundaries were incorporated into the intergranular network of the material, which is the type of microstructure desired to reduce the cracking susceptibility of the alloy. This thermomechanical treatment did not change the grain size of the alloy. The final grain size was 33 μm compared to 32 μm in the as-received condition.

The sample compressed 5% that was annealed at 950˚C showed a very substantial increase in the total CSLB fraction (51% CSLBs), as well as a small increase in the CSLB fraction (34% CSLBs) when the twins were eliminated from the measurement, indicating that the fraction of twin boundaries within the grains increased substantially, and a few additional Σ3 boundaries were created in the intergranular network as a result of the thermomechanical treatment. This type of microstructure is desirable because it improves the creep behavior of the alloy. This thermomechanical treatment did, however, increase the grain size from 32 μm to 42 μm or by 31%.

A sample compressed 7% was given an anneal at 950˚C. The results of the OIM scan on this sample were very similar to the results on the 5% compression sample that was annealed at 950˚C. The total CSLB fraction was 52% and CSLB fraction when the twins were eliminated was 34%. This confirmed that the CSLB enhanced microstructure was more dependent on the annealing temperature than on the amount of compression. This treatment resulted in an average grain size of 46 μm, an increase of 44% over the as-received condition. The OIM scans on 617 in the as-received condition and in all three CSLB enhanced conditions are shown in Figure C.1.

Table C.1: Summary of thermomechanical treatments used for CSLB enhancement

Specimen#	*Sample designation	Grain size (μm)	Σ3	Σ9+27	CSLB	HAB	CSLB – twins	HAB
1	617-as received	30	0.387	0.026	41%	59%	26%	74%
1	617-as received-verification	34	0.403	0.022	43%	58%	26%	74%
2	(5-900:7.5)	35	0.397	0.022	42%	58%	29%	71%
3	(5-925:7.5)	33	0.403	0.031	43%	57%	37%	63%
3	(5-925:7.5)+925:7.5	40	0.442	0.021	46%	54%	31%	69%
4	(5-925:7.5)-verification-1	32	0.345	0.027	37%	63%	27%	73%
4	(5-925:7.5)-verification-2	30	0.359	0.027	39%	61%	29%	71%
5	(5-925:7.5)x3	25	0.21	0.014	22%	78%	17%	83%
5	(5-925:7.5)x3 + 925:7.5	26	0.214	0.012	23%	77%	17%	83%
6	(7-925:7.5)x3 + 925:7.5	23	0.13	0.012	14%	86%	12%	88%
7	(7-925:7.5)x3 + 925:7.5 + 925:15	24	0.157	0.013	17%	83%	15%	85%
8	(3-950:7.5)	36	0.452	0.012	46%	54%	35%	65%
9	(5-950:7.5)	42	0.483	0.024	51%	49%	34%	66%
10	(5-950:7.5)-verification	30	0.314	0.019	33%	67%	25%	75%
11	(5-950:7.5)x3	26	0.173	0.01	18%	82%	14%	86%
11	(5-950:7.5)x3 + 950:5	25	0.156	0.014	17%	83%	12%	88%
12	(7-950:7.5)	46	0.511	0.013	52%	48%	34%	66%
13	(5-975:7.5)	29	0.293	0.022	32%	69%	25%	75%
13	(9-975:7.5)	36	0.411	0.013	42%	58%	31%	69%

*Note: Sample designation is denoted in the following way:

(%compression - annealing temperature : minutes annealed) × #cycles + additional annealing temperature : additional annealing time

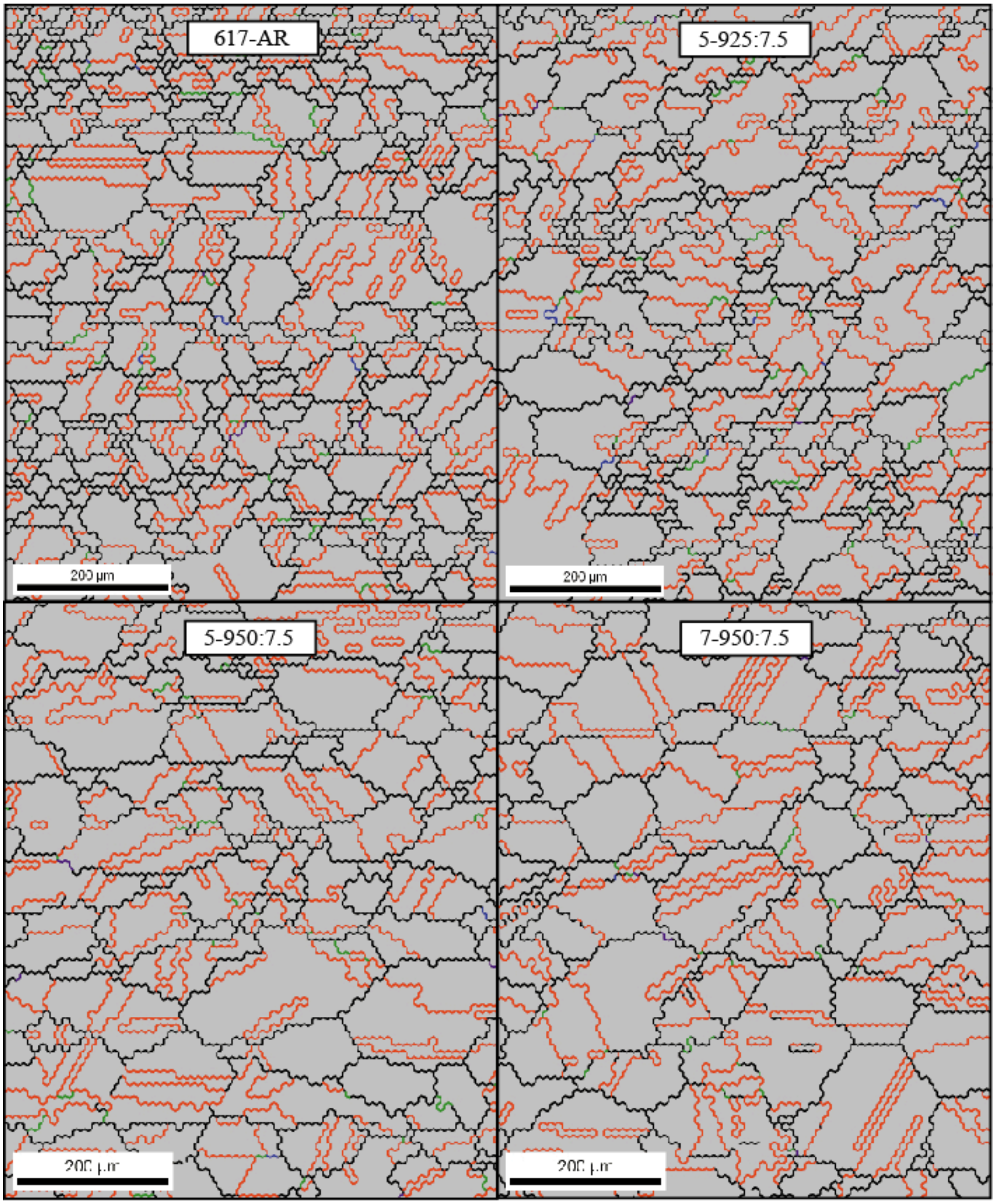

Figure C.1: OIM scans on the as-received material and the three samples that showed CSLB enhancement.

While a substantial increase in the CSLB fraction was achieved using the thermomechanical treatments previously described, the microstructure was not reproduced when the thermomechanical treatments were performed on new samples to verify the results. The CSLB fraction in the sample compressed 5% that was annealed at 925˚C was only ~28% when the twins were subtracted which was only slightly higher than in the as-received condition (26% CSLB). The total CSLB fraction in sample compressed 5% and annealed at both 925˚C and 950˚C dropped below the CSLB fraction in the as received material as indicated in Table C.1.

Attempts to increase the CSL fraction further focused on multiple (2 or 3) deformation and heat treat cycles. A series of three cycles of each thermomechanical treatment resulted in a sharp reduction in the CSLB fraction in the specimens. The CSLB fraction in a sample that was compressed 5% and annealed at 925˚C three times was only 17% and the CSL fraction in a sample that was compressed 5% and annealed at 950˚C three times was only 14%. Subsequent anneals on these same samples only resulted in further reductions in the total CSLB fraction. This lack of success using multi-step processes on the first lot of alloy 617 can be contrasted to the success using multi-step processes on a second lot of 617 that is described in the next section.

C.1.2 Multi-step compression and annealing treatments

The material used in this study was commercial INCONEL alloy 617 (UNS N06617) procured from Special Metals Inc. The chemical composition (in wt.%) of this alloy is listed in Table C.1. The as-received material was solution annealed at a temperature of 1176°C for a time commensurate with section size followed by water quenching.

Table C.1. Composition of the as-received INCONEL alloy 617 (wt%)

Ni	Cr	Co	Mo	Al	Fe	Ti	Si	Mn	C	Cu	S	B
>51.4	21.7	12.4	10.9	1.2	1.2	.3	.2	.05	~.1	<.05	<.015	<.006

Grain boundary engineering (GBE), proposed by Dr. Watanabe in the early 1980s [C.1], was employed in this study to promote a high proportion of low-Σ coincidence site lattice boundaries (CSLBs, $3 \leq \Sigma \leq 29$) for potential control of material's properties. In the nomenclature of the coincidence site lattice (CSL) model, the newly formed superlattice is denoted by a value of Σ, where the Σ value is defined as the reciprocal of the fraction of lattice points in the boundaries that coincide between the two adjoining grains. Thus, there is a low distortion of atomic bonds and relatively small free volume for CSLBs and consequently result in low boundary energy. Thermomechanical processing was performed on INCONEL alloy 617 to optimize grain boundary structure.

The study of the grain boundary character distribution (GBCD) was performed with a LEO 1530 FEGSEM incorporated with the TSL orientation imaging microscopy (OIM) system MSC2200. The SEM was operated at 20kV and the automatic electron backscatter diffraction (EBSD) scan was performed over an area of $500 \times 1000\ \mu m^2$ using a hexagonal grid with a step size of 5 μm. The number of scanned grains is about 1100 for each sample, which provided statistically significant results. To allow for the identification of the present phase with the EBSD analysis software, a crystallographic data file was established by X-ray diffraction analysis. For phase analysis with EBSD, a voting scheme and the confidence index (CI) established by TSL were used [C.2]. A high number of votes and higher CI values indicate a higher possibility that the phase is correctly identified. To determine whether a measured boundary can be classified as CSLBs, the Brandon criterion [C.3] was used as the allowable deviation from the exact orientation relationship. This states that the maximum allowable misorientation ($\Delta\theta$) from the exact CSL relationship is $\Delta\theta = \theta_m \Sigma^{-1/2}$, where θ_m is the maximum misorientation angle for a low angle boundary (typically 15°).

Various combinations of cold rolling and annealing were employed as the thermomechanical processing to achieve GBE effects on the as-received samples. Based on previous experience with GBE of an austenitic alloy 800H [C.4], an annealing temperature, 1100°C, followed by water quenching was used to ensure a single-phase austenite. Three levels of thickness reduction (5%, 9%, and 13%), different annealing times (15, 30, 45, 60, and 90 minutes), and multiple cycles of thermomechanical processing were employed in this study to investigate their effect on GBCD.

The average grain size of the as-received and GBE-treated samples is 22 μm and 26 μm, respectively. The minor enlargement of the grain size is reasonable because some random boundaries were transformed to coherent Σ3 boundaries. Coherent Σ3 boundaries were not counted as grain boundaries during grain size measurement because they are immobile and not a constituent of the intergranular transport network (see figure 2 of the introduction).

The EBSD analyzed GBCD of the GBE-treated samples, as well as as-received sample, are shown in Fig. C.2. The large thickness reduction did not significantly increase the low-Σ CSLB fraction or even reduce the fraction of the low-Σ CSLBs. This may be because the internal energy introduced by cold work could not be easily released following annealing to promote the transformation from random boundaries to low-Σ CSLBs. In addition, the low-Σ CSLBs increased by the previous processing cycle may be not able to be retained during the next cycle with a high thickness reduction. Optimal GBE-treatment was achieved using multiple processing cycles with a 5% thickness reduction. Two representative conditions of GBE-treated samples are highlighted with circles in Fig. C.2 and are denoted as GBE1 and GBE2. These two GBE-treated samples possess a similar low fraction of random boundaries (~27%). The major difference is that GBE2 has a ~13% smaller fraction of Σ1 boundaries (or a higher fraction of low-Σ CSLBs) compared to GBE1.

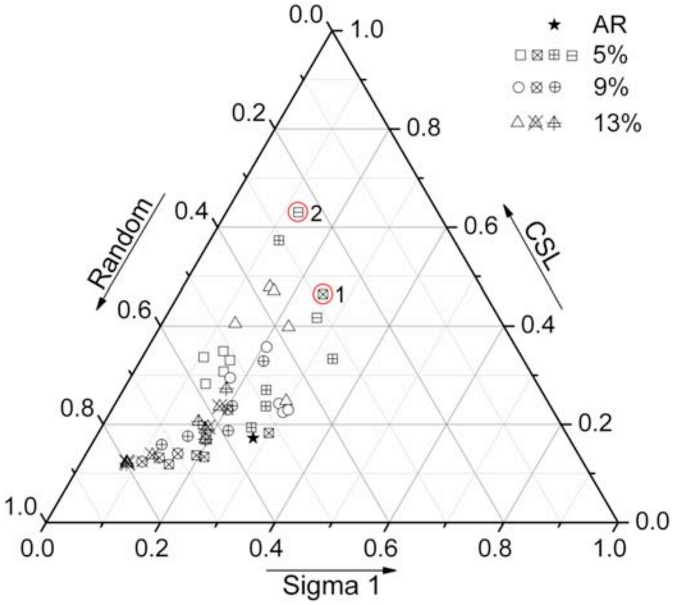

Fig. C.2. Grain boundary character distribution (GBCD: *Σ*1, low-Σ *CSL*Bs (Σ3-Σ29), and *random* boundaries) of the as-received (AR) and GBE-treated samples as a function of initial percentage reduction in thickness (5%, 9%, and 13%). The two data points highlighted with circles represent good GBE-treated conditions with similar low fraction of random boundaries, which are denoted as GBE1 and GBE2.

The fraction of the low-Σ CSLB components for the as-received and the two GBE-treated samples (GBE1 and GBE2) are shown in Fig. C.3. It is clear that the fractions of $\Sigma 3^n$ (Σ3, Σ9 and Σ27) boundaries were greatly enhanced for GBE-treated samples, GBE1 and GBE2. The fraction of Σ3 boundaries of GBE1 and GBE2 increased to ~36% and ~49%, respectively, compared to the ~11% for the as-received sample. The fractions of Σ9 and Σ27 boundaries of GBE1 and GBE2 were about 5-9 and 7-10 times of the as-received sample, respectively. The increased fractions of $\Sigma 3^n$ boundaries indicate that a lot of twinning and multiple twinning events occurred during annealing after cold rolling to ~5%. This is desirable for property improvement of materials. As shown in Fig. C.2, the fraction of $\Sigma 3^n$ boundaries of GBE2 is ~17% higher than that of GBE1 in addition to the difference in the fraction of Σ1 boundaries shown in Fig. C.2.

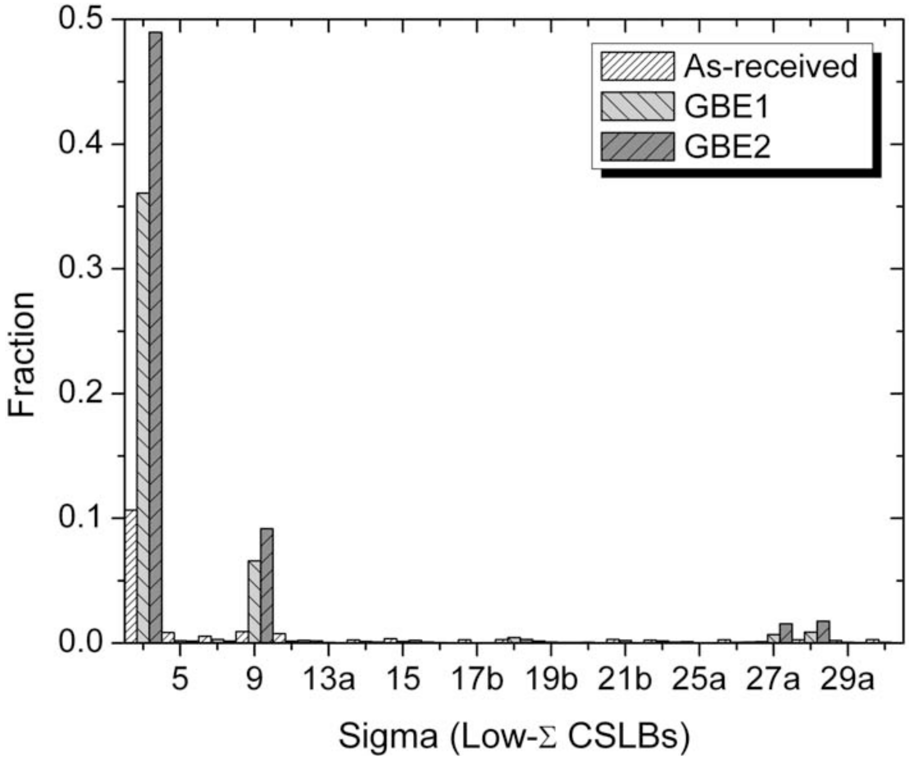

Fig. C.3. Fraction of low-Σ CSLBs of the as-received and GBE-treated samples, GBE1 and GBE2.

The fraction of grain boundaries as a function of the misorientation angle of as-received and GBE-treated samples is shown in Fig. C.4. The misorientation can be simplified by setting a misorientation angle of 15° as a division between low- and high-angle boundaries, which keeps the same angle as that defined in the Brandon criterion. The as-received sample has a high fraction of low-angle boundaries with the major contributor Σ1 (~2°). The GBE2 sample has a high fraction of high-angle boundaries with the major contributor Σ3 (60°) and Σ9 (38.9°). The GBE1 sample has similar fraction of low-angle and high-angle boundaries.

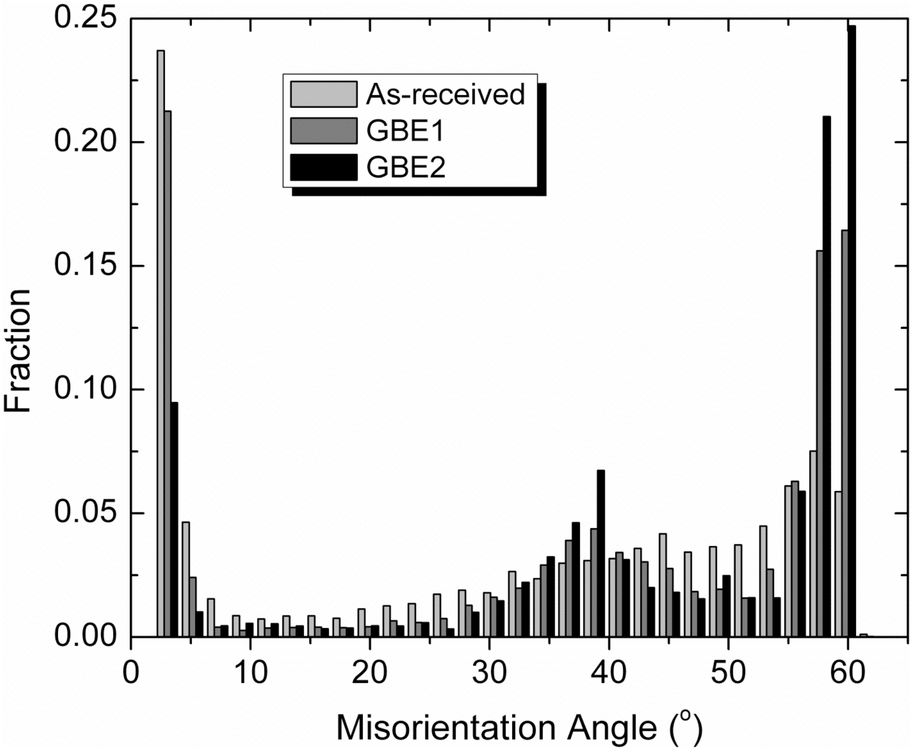

Fig. C.4. Grain boundary misorientation of the as-received and GBE-treated samples (GBE1 and GBE2).

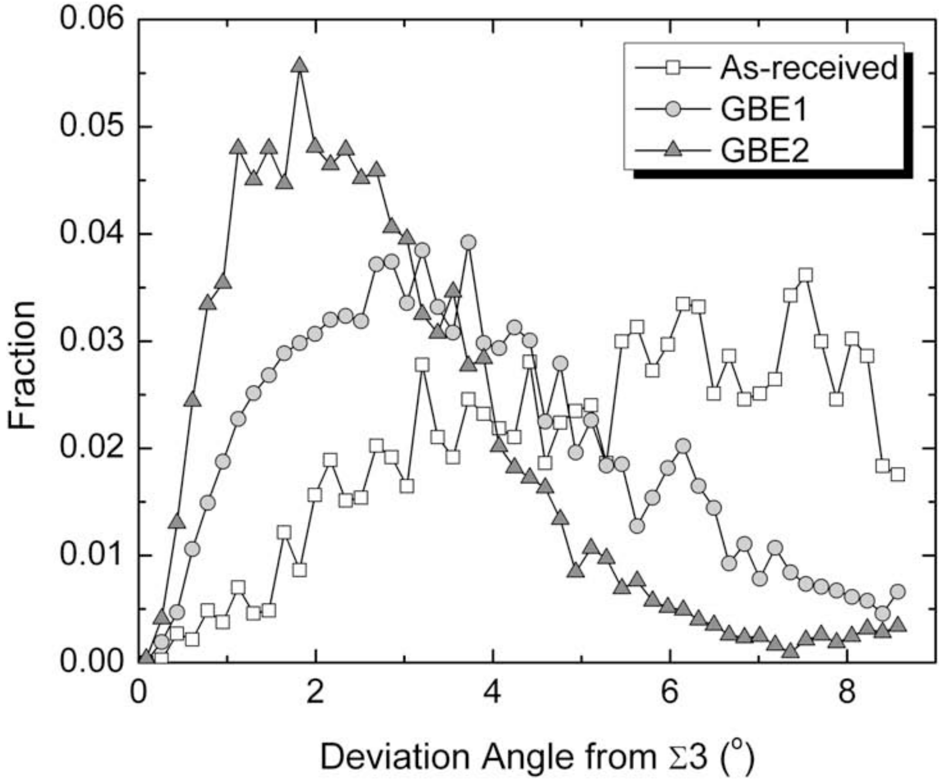

Fig. C.5. Deviation angle from exact Σ3 of the as-received and GBE-treated samples, GBE1 and GBE2.

The quality of the GBE could be represented by the deviations from exact Σ misorientation. Since Σ3 is the most important CSLBs correlated with property improvement [C.5], the deviation from the exact Σ3 misorientation, which is plotted in Fig. C.5, is worthy of studying to evaluate the GBE quality. The GBE2 sample, which has the highest fraction of Σ3 boundaries, shows the smallest deviation from the exact Σ3 compared to the as-received and GBE1 samples.

C.2. Thermal Stability of GBE

GBE treatment has the ability to effectively increase the population of CSLBs which are beneficial for many properties, e.g. creep, stress corrosion cracking resistance, etc. Since atomic migration is promoted at elevated temperature, TMP-promoted low-Σ CSLBs may become unstable and be transformed into random boundaries. Thus, it is necessary to evaluate the thermal stability of GBE-optimized samples. Due to the anticipated high-temperature application of alloy 617, thermal stability of GBE-treated samples was tested at 850°C in air for 4 and 6 weeks. The selection of the annealing temperature, 850°C, refers to the design of a Generation IV nuclear reactor, e.g. the outlet temperature of the gas-cooled fast reactor (GFR) [6]. As-received samples were also tested at the same time for comparison.

The fractional change of Σ1, low-Σ CSLBs, and random boundaries due to annealing at 850°C is shown in Fig. C.6. The fractional change is insignificant for the GBE2 sample. In contrast, the 6-week annealed as-received and GBE1 samples exhibit noticeable changes. This result indicates a trend that an initial large fraction of Σ1 boundaries can be changed to CSLBs when the initial fraction of random boundaries is relatively large, e.g. >~50% for the as-received sample, or random boundaries when the initial fraction of random boundaries is moderate, e.g. ~30% for the GBE1 sample. Fig. C.6 also shows that longer annealing time generally impairs the effect of GBE. According to the GBE thermal stability test, therefore, the use of GBE-treated samples with a low fraction of Σ1 and high fraction of low-Σ CSLBs is reliable at 850°C, at least for 1000 hours.

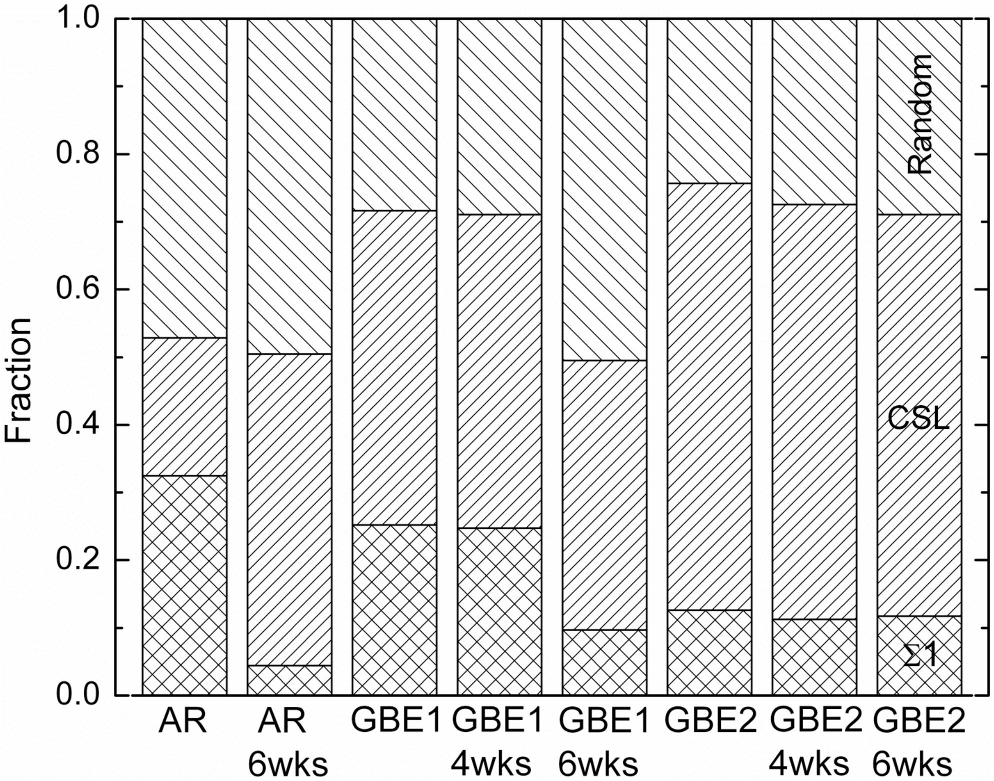

Fig. C.6. Thermal stability of the grain boundary character distribution of as-received and GBE-treated samples, GBE1 and GBE2, after exposure at 850°C for 4 and 6 weeks.

C.3. Supercritical Water (SCW) Exposure

While waiting for high-temperature environmental chambers to be constructed to test 617 in high-temperature flowing gas, the effect of GBE on corrosion was examined by exposing coupons to supercritical water.

The effect of GBE on oxidation behavior of alloy 617 was studied by exposing the as-received and GBE-treated (GBE1 and GBE2) samples to SCW at 500°C and 25 MPa. The weight gains of the samples exposed for 385 hrs are shown in Fig. C.7, which indicate a higher and a lower weight gain for GBE1 and GBE2, respectively, compared to the as-received sample. Detailed comparison on the microstructure of these samples will be performed. Longer exposure time for these samples, i.e. ~667 hrs, is currently being performed.

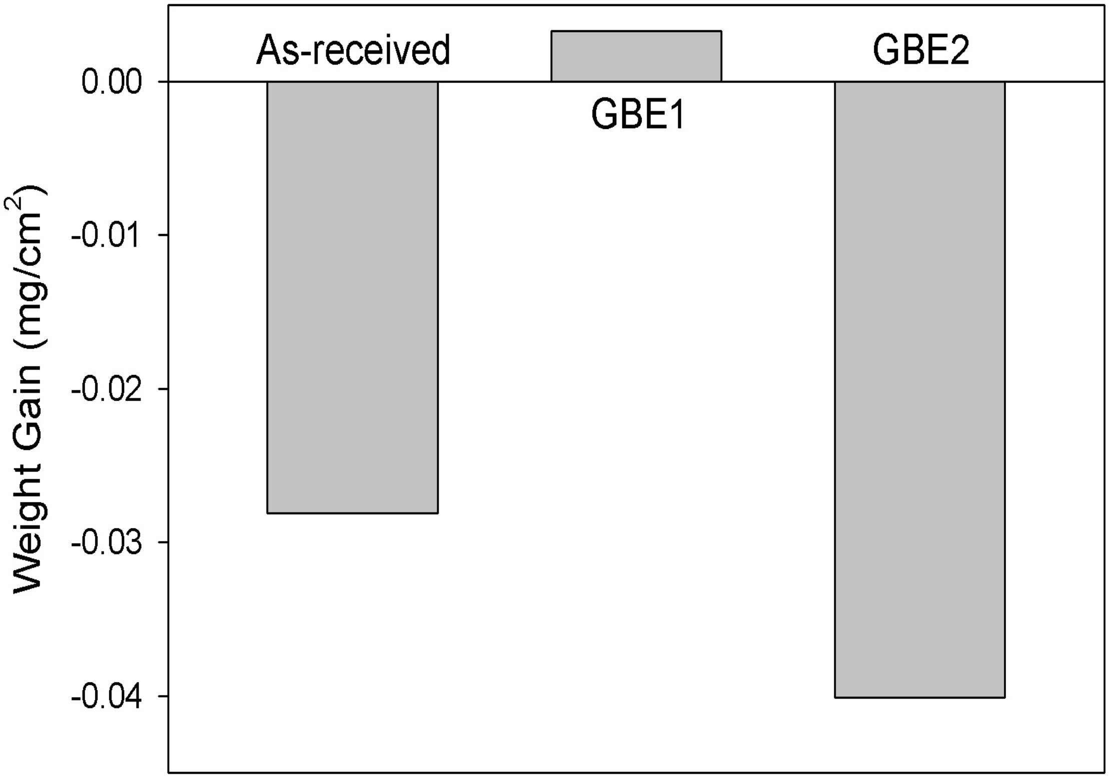

Fig. C.7. Weight gain of as-received and GBE-treated (GBE1 and GBE2) samples exposed to supercritical water at 500°C and 25 MPa for 385 hrs.

C.4. Future Work

- A thermal stability study must be performed on the CSLB-enhanced microstructure of alloy 617 to determine the maximum temperature that the alloy can withstand while maintaining its CSLB enhanced microstructure. The thermal stability of as-received and GBE-treated (GBE1 and GBE2) samples is being tested at a higher annealing temperature (1000°C).
- Successfully verify that the thermomechanical treatments performed on the 617 at 925˚C and 950˚C will reliably enhance the CSLB fraction in the alloy. The stronger dependence of the CSLB-enhanced microstructure on annealing temperature rather than %compression indicates that a stronger emphasis on temperature control may solve this reproducibility problem.
- Creep tests and constant extension rate tensile (CERT) tests must be performed on samples of alloy 617 in the CSLB-enhanced condition to verify that these microstructures improve the creep and cracking resistances of the alloy.
- Additional oxidation tests at longer times and higher temperatures to determine the effect of GBE on oxide growth and stability.
- Initiate studies of the effect of GBE on impact properties

C.5 References

[C.1] T. Watanabe: *Res. Mechanica*, 1984, vol. 11, pp. 47-84.

[C.2] D.P. Field: *Ultramicroscopy*, 1997, vol. 67, pp. 1-9.

[C.3] D.G. Brandon: *Acta Metall.*, 1966, vol. 14, pp. 1479-84.

[C.4] L. Tan, T.R. Allen, An EBSD study of grain boundary engineered INCOLOY alloy 800H, Mater. Met. Trans. A 36 (2005) 1921-1925.

[C.5] V. Randle: *The role of the coincidence site lattice in grain boundary engineering*, The Institute of Materials, London, 1996, pp. 7, 91.

[C.6] A Technology Roadmap for Generation IV Nuclear Energy Systems, Issued by the U.S. DOE Nuclear Energy Research Advisory Committee and the Generation IV International Forum, December 2002. (http://gif.inel.gov/roadmap/)

[C.7] G. Palumbo, K.T. Aust, U. Erb, P.J. King, A.M. Brennenstuhl, P.C. Lichtenberger: *Phys. Status Solidi A*, 1992, vol. 131, pp. 425-8.

D. Radiation Response of Alloy 800H

D.1. Literature survey of radiation effects in alloy 800H and alloy 800

Only limited studies of the radiation resistance of alloy 800 and alloy 800H have ever been performed. The results are highlighted in the following sections. Alloy 800 has the same allowed composition range as 800H. The difference between the two is the grain size, which is larger in alloy 800H to improve high temperature creep strength.

D.1.1 Elongation

Lindgren reports the findings for elongation tests on Incoloy 800 [D.1]. The samples were annealed at 1150°C followed by either irradiation to 2 to 3×10^{20} n/cm^2 at 760°C or soaked at 760°C for the control. The tests were preformed at 760°C and 0.002% per minute elongation. Figure D.1 shows these results. Typical of austenitic alloys, the elongation at failure decreased during irradiation. The uniform elongation following irradiation was still quite large, near 10%. Little change in yield strength occurred. Lindgren also reports the effect of strain rate on the fracture elongation. This can be seen in Figure D.2. The elongation at fracture is minimum between 10^{-3} and 10^{-2} s^{-1}. Thiele et al. reports on rupture elongation of Incoloy 800H at various temperatures [D.2] to fluences of 1×10^{25} n/m^2. In Figure D.3, Incoloy 800H is represented by alloy 2. After irradiation, the rupture elongation dramatically decreases with the greatest decrease occurring at the highest temperature of 850°C.

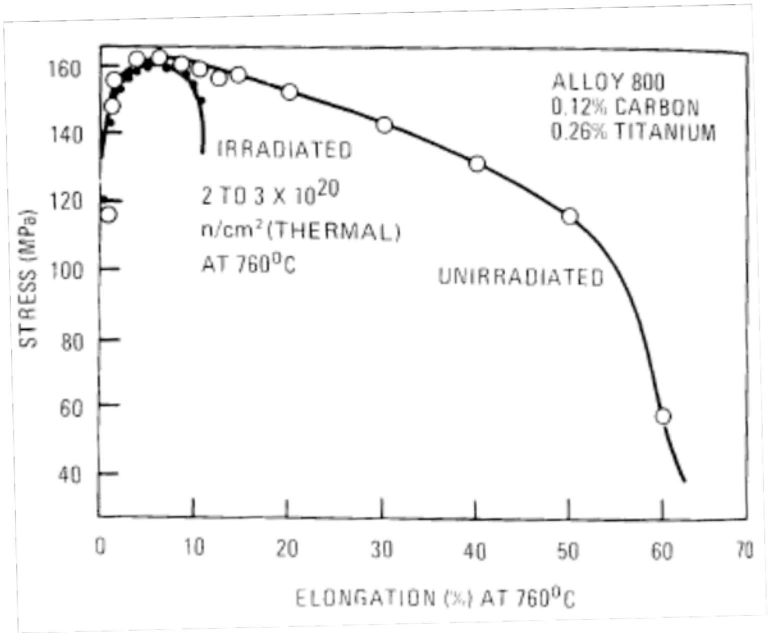

Figure D.1. Tensile stress-strain curves from irradiated and control samples of Incoloy 800 with varying degrees of carbon content.

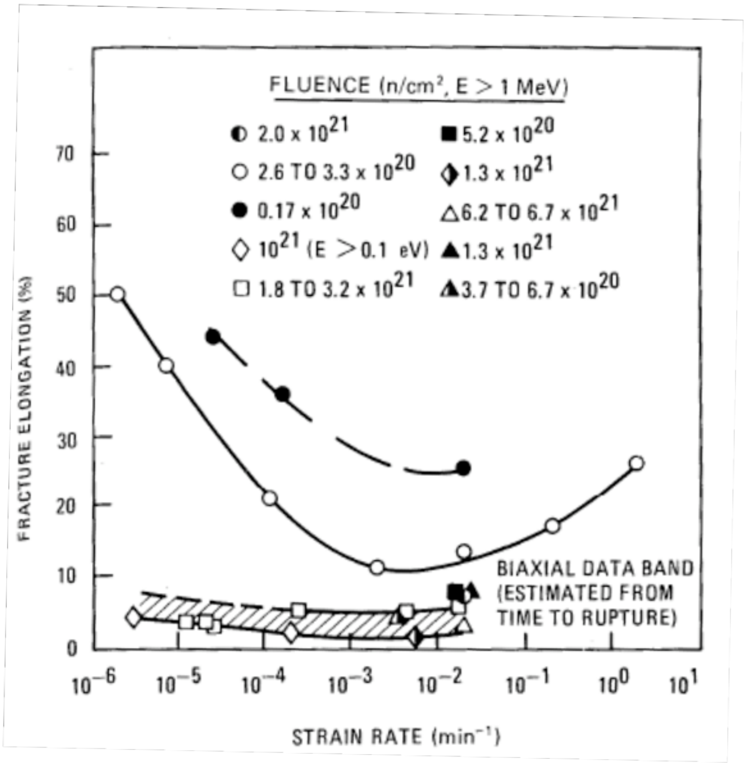

Figure D.2. Effect of strain rate on the fracture elongation of Incoloy 800 at 704°C.

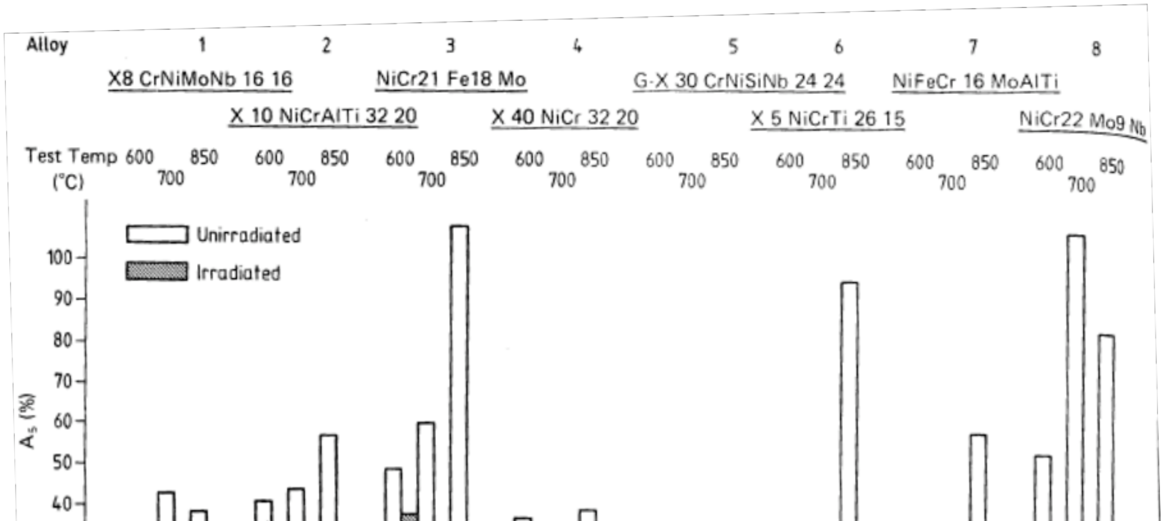

Figure D.3. Influence of test temperature on rupture elongation (A_s) of various Ni-base alloys (alloy 2 is alloy 800, alloy 3 is Hastelloy X) before and after irradiation.

Harman studied Incoloy 800 using the Oak Ridge Research Reactor [D.3]. Nine heats of commercial vacuum melted Incoloy 800 were irradiated in both the core and poolside. These samples were used to study the effect of carbon and titanium on mechanical properties of 800H. The samples were irradiated in a He + 1% O_2 atmosphere at temperatures ranging from 500 to 760°C with fluences ranging from 2 to $8\text{x}10^{20}$ n/cm^2 thermal and 1 to $8\text{x}10^{20}$ n/cm^2 fast. Control samples were heated in a laboratory furnace using an inert argon atmosphere. All the testing was conducted in air at temperatures of 700 and 760°C. Elongation of both high and low carbon alloys tested at 700°C after thermal exposure for ~2300 hours at 700°C only and after exposure to about $0.8\text{x}10^{21}$ n/cm^2 (thermal or fast) at 700°C can be seen on Figure D.4 [D.3]. The tensile tests reported by Harman were done at 0.002/min and creep stresses ranging from 11,000 to 15,000 psi depending on the carbon levels. A pronounced peak in creep ductility with and without irradiation in samples with 0.1% titanium is noted for both carbon levels. The higher creep ductility of the low-carbon alloys is due to their finer grain size. The good ductility in the irradiated samples was observed at other temperatures as well. Figure D.5 shows the ductility of Incoloy 800 at 760°C of irradiated and control samples as a function of the strain rate [D.3]. The specimens were solution annealed at 1150°C and irradiated at 760°C with fluences of 3 to $4\text{x}10^{20}$ n/cm^2 thermal. At sufficiently low strain rates the post-irradiation ductility of the samples containing 0.1% titanium approaches that of the corresponding control sample.

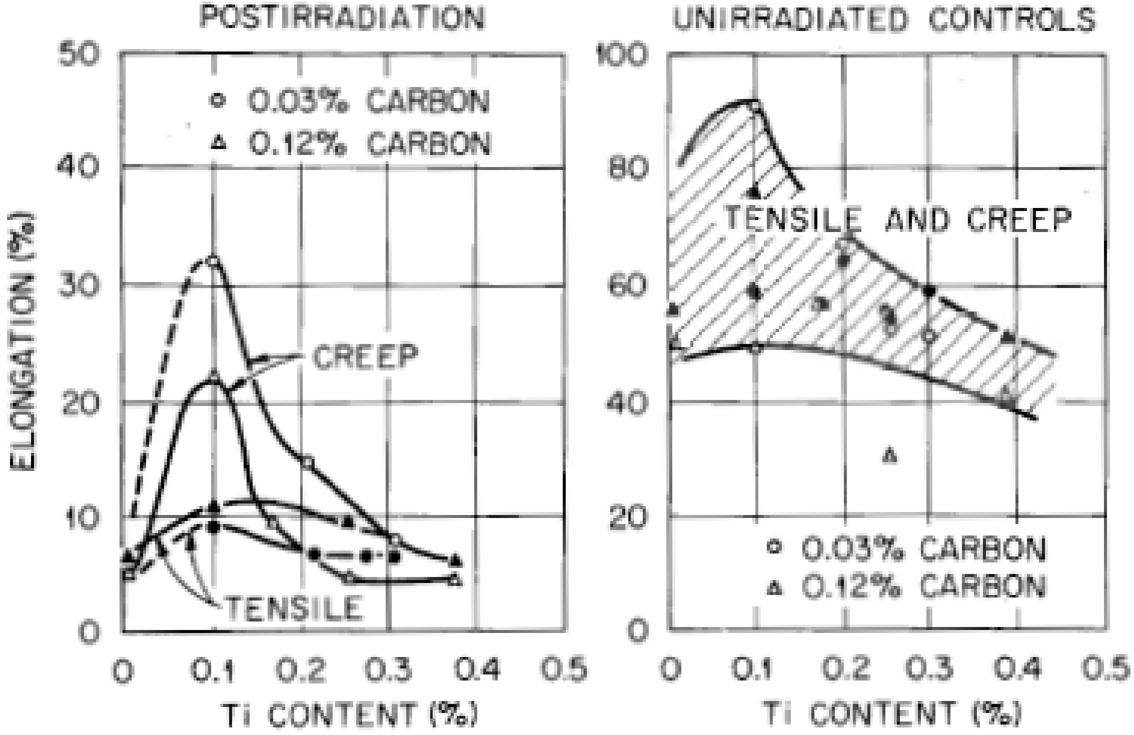

Figure D.4. Tensile and creep ductility of Incoloy 800 at 700°C.

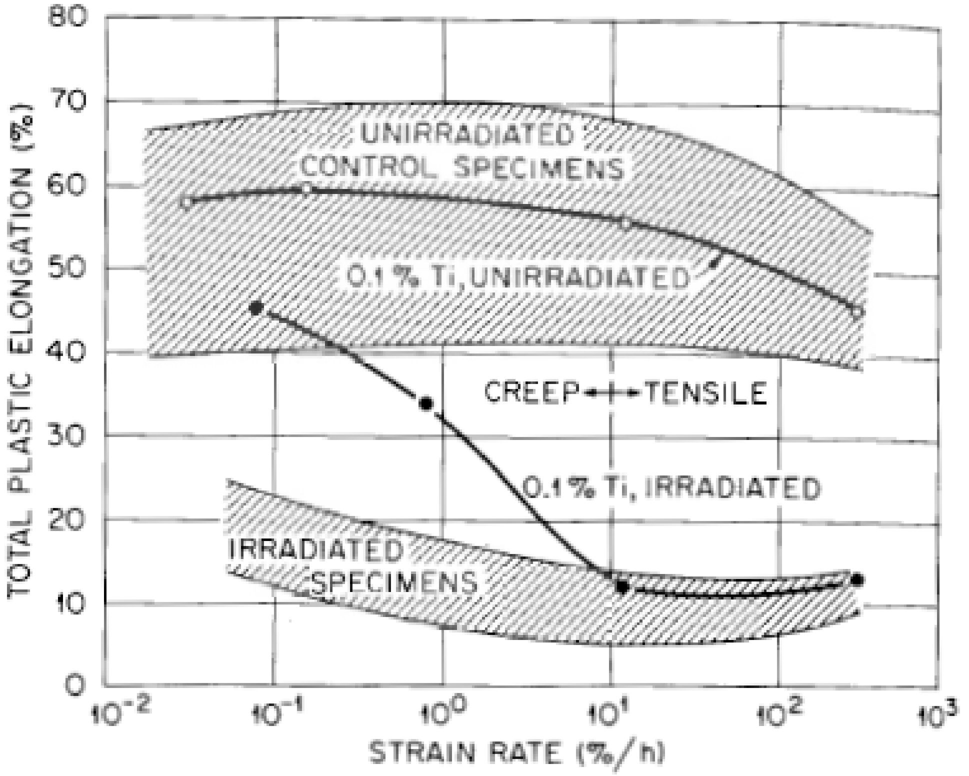

Figure D.5. Effect of strain rate on ductility of Incoloy 800 at 760°C.

D.1.2 Grain Size Effects

Harman controlled grain size in Incoloy 800 samples by recrystallizing cold-worked material at different temperatures [D.3]. Average grain diameters of 7 to 170 μ for the samples with carbon contents of 0.03% was produced and average grain diameters of 4 to 40 μ was produced for the samples with a carbon content of 0.12%. Harman reports that increasing the grain size provided lower creep rates, longer rupture times and higher ultimate tensile strengths for the unirradiated control samples. The ductility of unirradiated Incoloy 800 generally increased with decreasing grain size or decreasing strain rate. All of these effects were also observed in the irradiated samples. There was also a very pronounced effect of grain size on the postirradiation ductility of the specimens.

Figure D.6 shows the creep elongations and rupture times of 0.1 and 0.3% titanium heats of both carbon levels of Incoloy 800 tested in air at 700°C and 10,000 psi [D.3]. The samples were irradiated to a thermal fluence of 2 to $3x10^{20}$ n/cm^2 at 700°C. The fine grain samples with 0.1% titanium has elongations of 85 to 100% with a decrease to 60 to 85% for samples with larger grain sizes. The corresponding control samples elongation of 130 to 165% for the fine grain samples and 75 to 90% for the samples with larger grains. The Incoloy 800 samples with 0.3% titanium were less ductile but showed a similar grain size effect. Samples with fine grains show postirradiation creep elongation values of 35% with a decrease to 15% for larger-grained samples. The elongation values for the control samples with 0.3% titanium were very similar to those with 0.1% titanium. No effect of carbon content was seen for either titanium level. Figure

D.6 also shows the significantly longer rupture times for the coarse grained samples. The control specimens showed longer rupture times than the irradiated samples and the grain size effect was even more pronounced. The minimum creep rates for irradiated and unirradiated of the 0.1% titanium content samples are shown in Figure D.7 [D.3]. The samples were irradiated to 2 to $3x10^{20}$ n/cm^2 at 700°C and tested in air at 10,000 psi and 700°C. A strengthening effect of carbon is seen for the larger grain diameters.

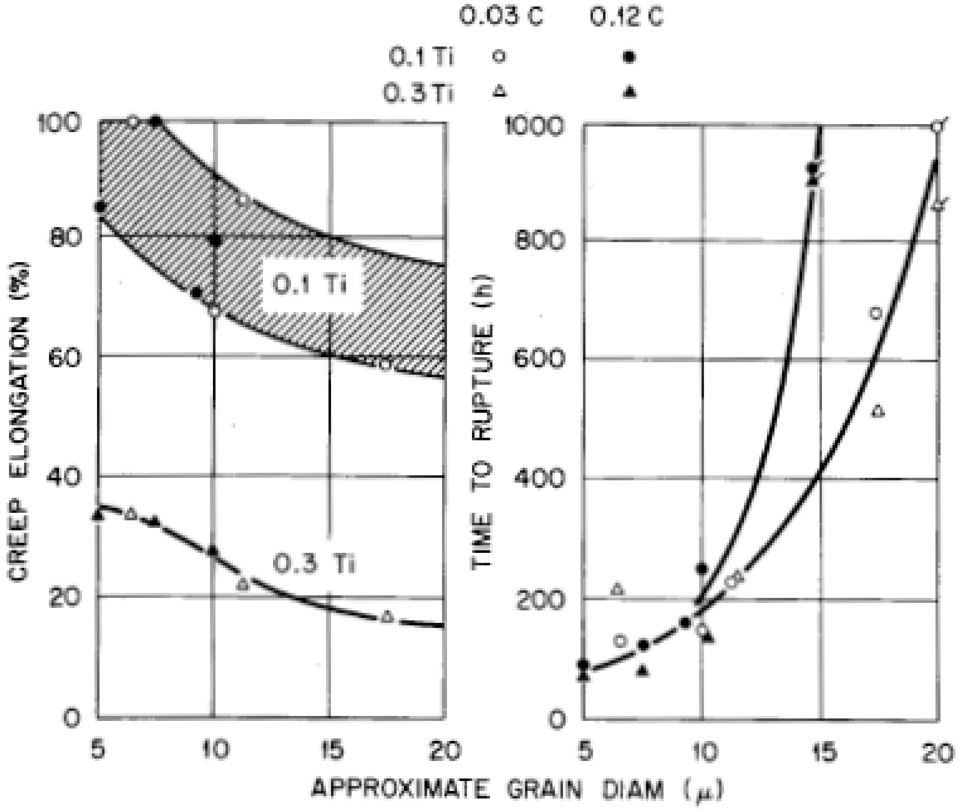

Figure D.6. Effect of grain size on the creep-rupture properties of Incoloy 800.

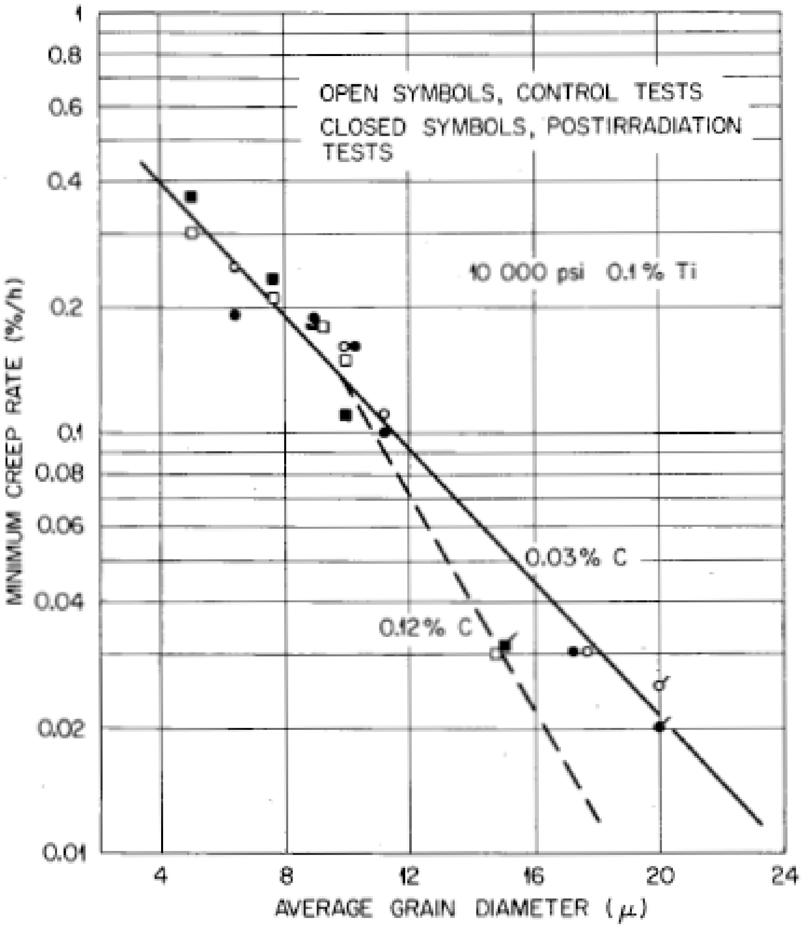

Figure D.7. Effect of grain size on the creep strength of Incoloy 800.

D.1.3 Fatigue

Fatigue crack growth studies of irradiated Incoloy 800 samples were done by James [D.4]. The samples were irradiated in the Experimental Breeder Reactor II in flowing sodium coolant at temperatures of 400 to 430°C. Fatigue testing was accomplished in an air environment at 427°C. Figure D.8 compares the results for unirradiated and irradiated samples. Linear least-squares regression lines are drawn through sets of data in the figure. In general, the amount of scatter around the regression lines is similar for the irradiated and unirradiated samples. Figure D.8 shows that there is little or no influence of irradiation on the fatigue-crack growth behavior of Incoloy 800. The regression lines for the two sets of data are very similar with the scatter bands for both irradiated and unirradiated samples overlapping.

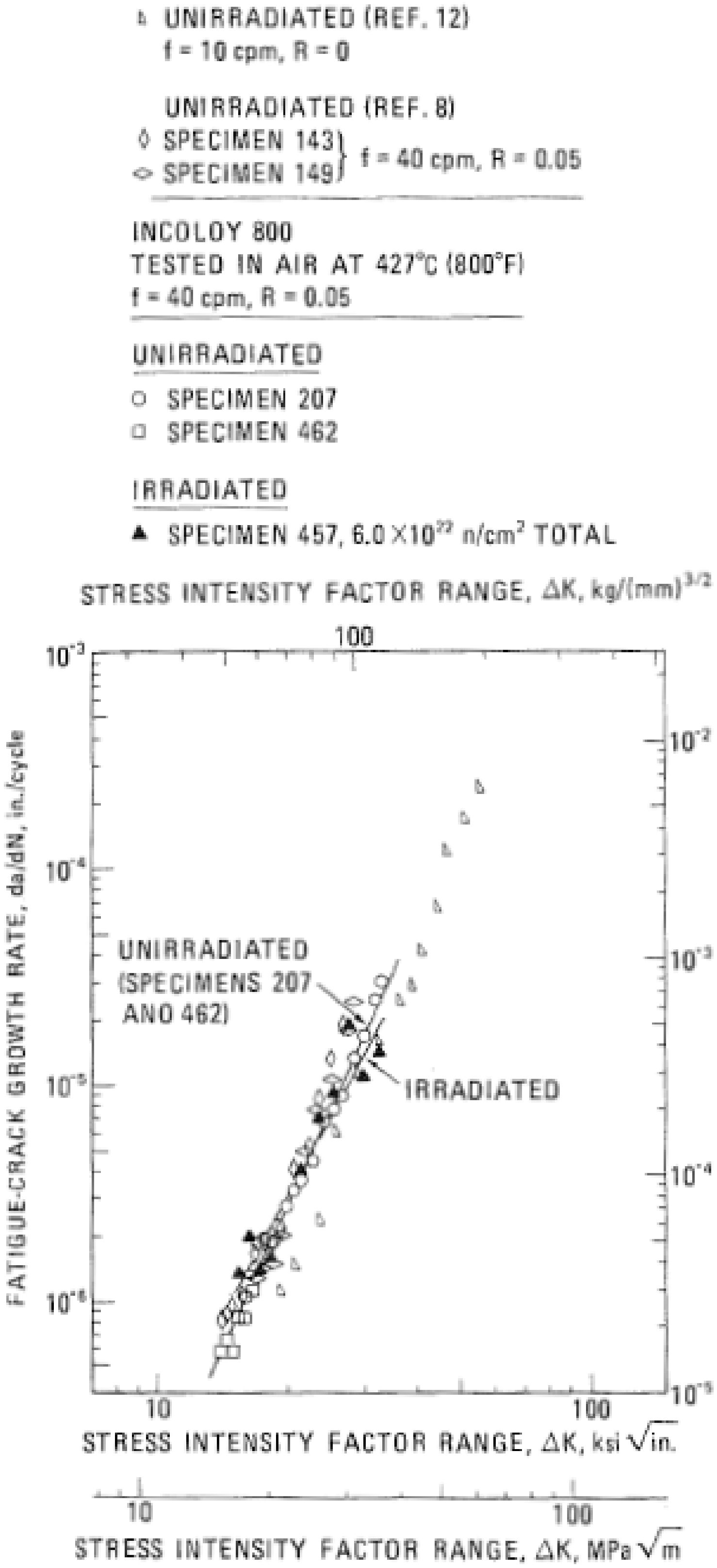

Figure D.8. Fatigue-crack propagation behavior of unirradiated and irradiated Incoloy 800.

Fatigue behavior of Incoloy 800 was also studied by Brinkman et al [D.5]. Strain-controlled fully reversed uniaxial fatigue tests were conducted at constant strain ranges that varied from approximately 0.35 to 2.44% peak-to-peak. The samples were fatigued until failure and the strain rate was controlled at either 8×10^{-4} or 6×10^{-5} s^{-1}. For Incoloy 800, reductions in fatigue life attributable to irradiation ranged up to a factor of 35. Severe irradiation-induced embrittlement of the Incoloy 800 resulted in a large decrease in fatigue life that appeared to be fluence dependent, particularly in the high-strain, low-cycle-to-failure region.

D.1.4 Tensile

Thiele et al describe the results of tensile test on Incoloy 800H at 600, 700 and 850°C [D.2]. The irradiated samples show an increase of the yield strength (0.2% proof stress). The effect is seen to decrease with increasing temperature. Figure D.9 shows these results with Incoloy 800H represented by alloy 2. The ultimate tensile strength (UTS) of Incoloy 800H is shown in Figure D.10. At 600°C, the irradiated sample shows a slight increase in UTS while at the two higher temperatures, there is no difference in the UTS between the unirradiated and irradiated samples.

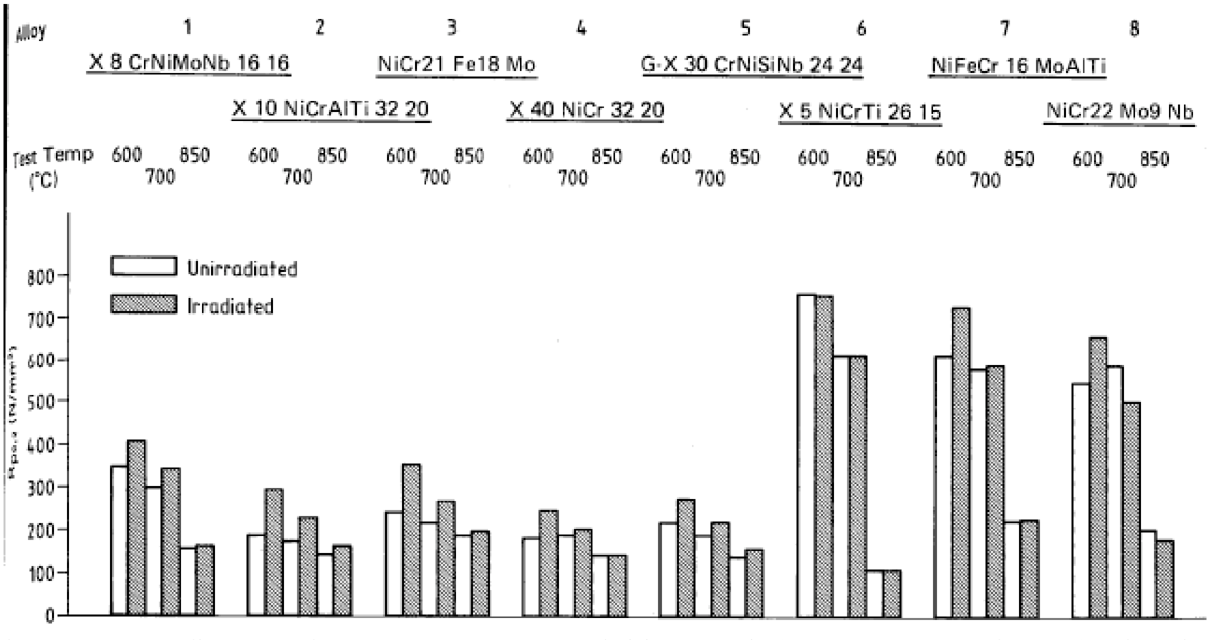

Figure D.9. Influence of test temperature on yield strength ($R_{p0.2}$ 0.2% proof stress) of various Ni-base alloys (alloy 2 is alloy 800, alloy 3 is Hastelloy X) before and after irradiation.

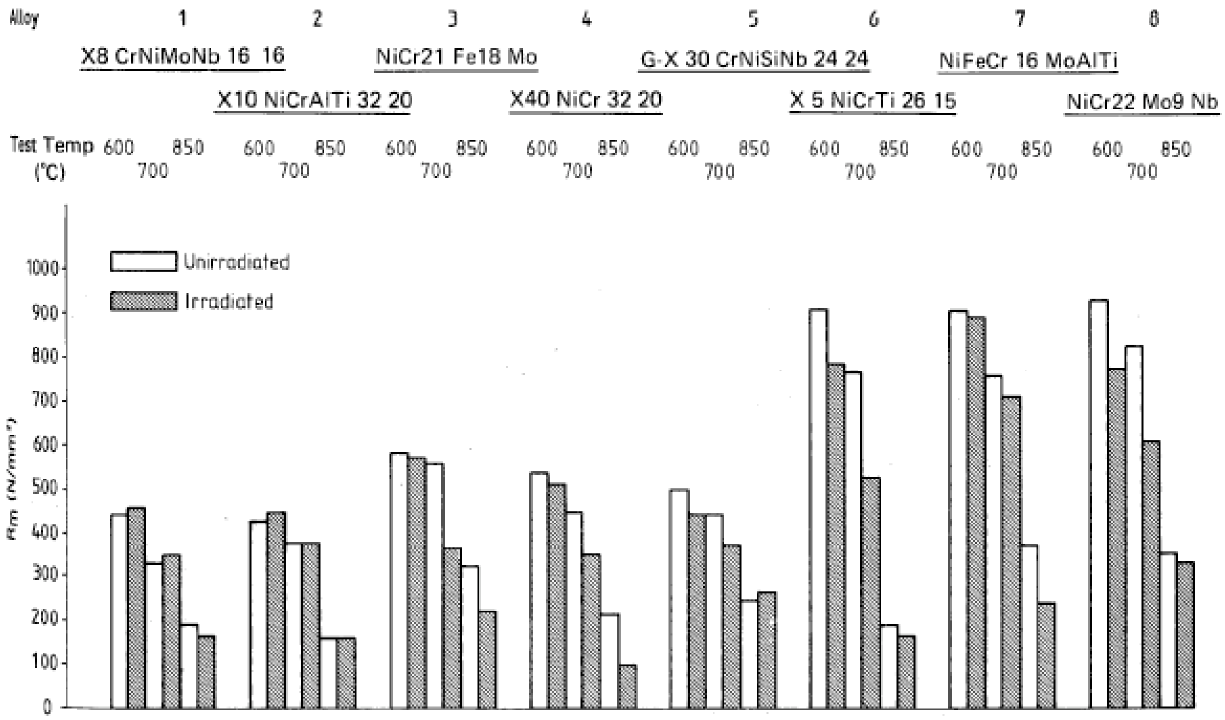

Figure D.10. Influence of test temperature on ultimate tensile strength (R_{max}) of various Ni-base alloys (alloy 2 is alloy 800, alloy 3 is Hastelloy X) before and after irradiation.

The data from Brinkman et al [D.5] indicated that for Incoloy 800, irradiation results in a marked decrease in ductility, and increase in yield strength, an increase in the ultimate tensile strength and a substantial decrease in uniform elongation [D.5]. Limited tensile data at a strain rate of $6x10^{-5}$ s^{-1} for the irradiated Incoloy 800 indicate a significant strain dependency of the strength level at 700°C.

D.1.6 Swelling

Gelles studied Incoloy 800 along with several other alloys to determine swelling response after irradiation [D.6]. Samples of solution treated Incoloy 800 were irradiated at either 425°C to a fluence of $2.07x10^{23}$ n/cm^2 or 540°C to a fluence of $2.32x10^{23}$ n/cm^2. For the samples irradiated at 425°C, the swelling was 41.1% while the samples irradiated at 540°C show a swelling of just 12.0%.

Microstructural examinations of Incoloy 800 by Gelles show that it swells more than other austenitic alloys due to voids growing larger [D.6]. In the Incoloy 800, the largest voids seen tend to be associated with large precipitate particles. Also void coalescence is seen in the samples with large void structures. In the sample irradiated at 425°C, examples of dislocation and gamma prime precipitate structures were seen. The dislocation structure consists of a fine tangle of dislocations and loops and the precipitate structure includes blocky gamma prime particles and a fine dispersion of MC carbide particles. Microstructural comparisons between austenitic alloys confirm the density measurements and show Incoloy 800 to be a high swelling alloy. This is in contrast the work by Bates and Powell that shows alloy 800H to swell much less than compositions typical of austenitic stainless steels like 310. AISI 310 is based on Fe-25Cr-21Ni while 800H is based on Fe-21 Cr-32Ni [D.7]. Typically increasing bulk Ni and decreasing bulk Cr decreases swelling

D.1.7 Creep

Creep rupture was reported by Lindgren for Incoloy 800 [D.1]. The samples were solution treated at 980°C and then irradiated at 650, 700 or 705°C. The samples were irradiated at different fluences of fast and thermal neutrons. All the samples were tested at 705°C. The results can be seen in Figure D.11. The creep rupture strengths of unirradiated and irradiated Incoloy 800 appear to be about equal for longer rupture lifetimes. Figures D.12 and D.13 show the effect of carbon and titanium levels on the creep and tensile elongation of irradiated Incoloy 800. The data reported in Figure D.12 comes from samples that were irradiated in the Oak Ridge Research Reactor at 650°C and 700°C and tested at 700°C. The fluence was approximately 0.8×10^{21} n/cm^2 thermal. The data reported in Figure D.13 comes from samples that were annealed at 1150°C then irradiated at 760°C to 3 to 4×10^{20} n/cm^2 thermal. The tests were conducted at 760°C. The creep elongation peaks for compositions of 0.1 % Ti and is greater for smaller grain size in those higher carbon alloys.

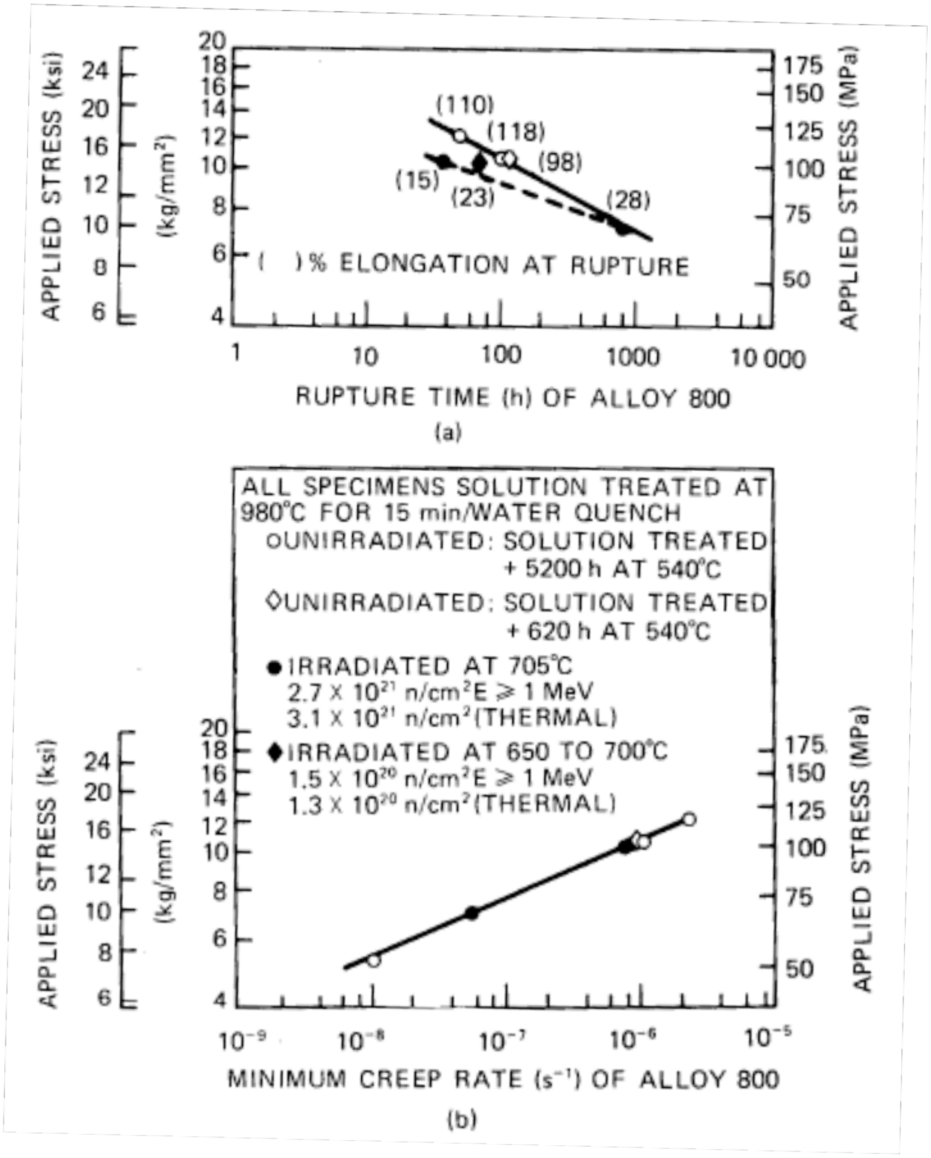

Figure D.11. Creep rupture results of unirradiated and irradiated Incoloy 800: (a) time to rupture as a function of applied stress and (b) minimum creep rate as a function of applied stress.

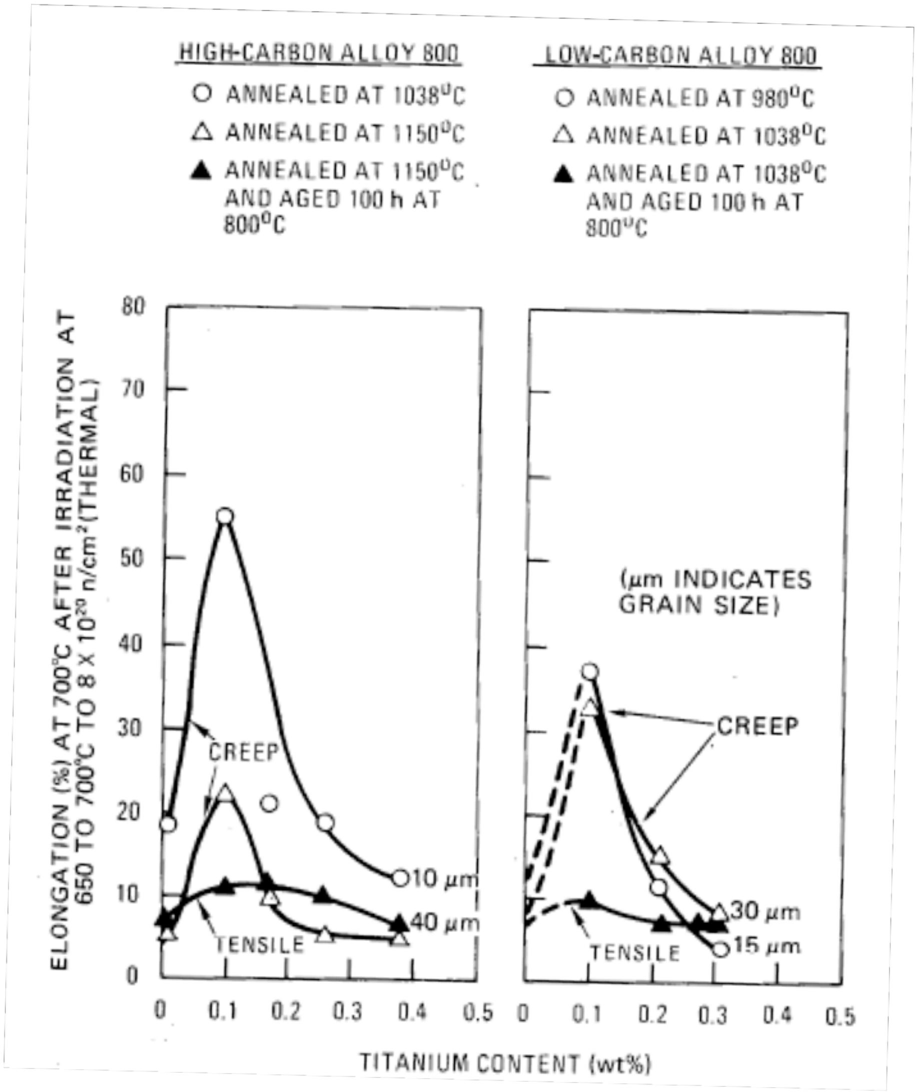

Figure D.12. Postirradiation ductility of experimental heats of Incoloy 800.

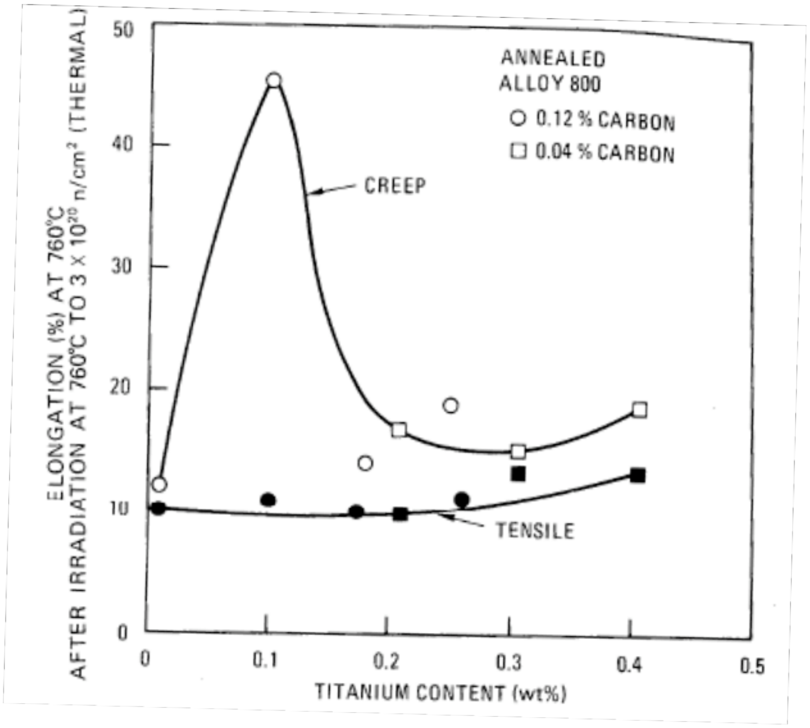

Figure D.13. Postirradiation ductility of experimental Incoloy 800.

D.1.8 Embrittlement

Thiele et al showed that significant high temperature embrittlement, as measured using the reduction in area as the measure of embrittlement, occurs at 700°C and 850°C for Incoloy 800H [D.2]. This trend is shown in Figure D.14.

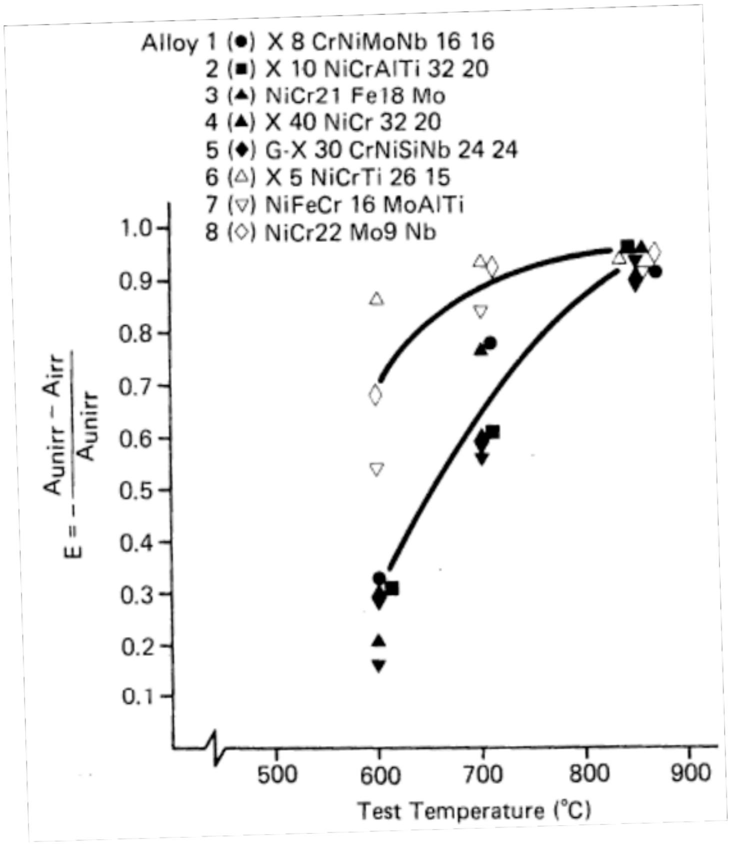

Figure D.14. Influence of test temperature on embrittlement, *E*, of Incoloy 800H represented by alloy 2.

D.2. Microstructural changes in alloy 800H due to heavy ion irradiation

D.2.1 Materials and methods

The composition for alloy 800H is listed in Table D.1. The alloy is commercial grade and used in the as-received condition. No thermal mechanical treatment was given. The manufacturer of the alloy 800H specified a final heat treatment at temperature of 1177ºC for 2.25 hours.

Ni-ion irradiations were conducted at the Environmental and Molecular Science Laboratory at Pacific Northwest National Laboratory using 5 MeV Ni ions at 500°C and $1\text{x}10^{-7}$ torr with a damage rate of $1.39\text{x}10^{-3}$ dpa/s. The material was irradiated to doses of 5 and 50 dpa on a foil sample with size approximately 15x15x0.200 mm^3.

Microstructure characterization for unirradiated and the irradiated samples was carried out using a 200KV transmission electron microscope equipped with EDS for chemical analysis and a digital camera with an imaging area of 19x19 mm on screen and a resolution of 2048x2048 pixels for each digital picture.

Table D.1. Composition for Alloy 800H (Fe balance).

Alloy	C	Mn	P	S	Si	Ni	Cr	Mo	Other
800H	0.069	0.76	0.014	0.001	0.13	31.59	20.42	Not measured	Ti_0.57, Cu_0.42 Al_0.50

D.2.2 Ion-irradiated 800H Irradiated microstructure of 800H

The unirradiated microstructure of alloy 800H is shown in the Figure D.15. The micrograph shows a relatively high dislocation density (~ $4\text{x}10^{13}$ m^{-2}) for the alloy heat-treated at 1177ºC for 2.25 hours. There are no precipitates found in the unirradiated condition.

For the 800H irradiated with Ni ions at 500ºC to a dose of 5 dpa, the microstructure was altered by the formation of faulted dislocation loops. No voids were found at 5 dpa. The irradiated microstructure is dominated by the dislocation loops shown in Figure D.16. The average size of the faulted loops is 12.5 nm with a loop density of $1.2\text{x}10^{16}$ cm^{-3}. Although no radiation-induced precipitates were found in the matrix, precipitates were found in a piece of suspension film attached around the edge of the perforation. This suspension film was formed accidentally during jet-polishing and provided an opportunity to reveal possible precipitates in the materials. Figure D.17 shows precipitates caught on the suspension film and the EDS spectrum comparison between the matrix and the precipitates on the film. These precipitates may consist of different types with an average size of approximately 9 nm. The EDS spectrum shows that these precipitates are rich in Cr (40~56%), Si (4~14%), Al (5~10%) and Ti (1.5~2.5%). The crystal structure of the precipitates could not be determined due to the small size and the presence of multiple types of precipitates. Since a 5 dpa irradiation only took 60 min to complete, it is hard to believe all these precipitates were formed due to irradiation. It appears that most of these precipitates were existed in the unirradiated materials but at a very low density, and are therefore difficult to detect.

For the 800H irradiated to 50 dpa at 500ºC, the irradiated microstructure is dominated by faulted loops and small precipitates uniformly distributed throughout the sample. No cavities were detected under this irradiation condition. The bright field image (g=200) and the rel-rod dark filed image of the faulted loops are shown in Figure D.18. The average size of faulted loops is 8.4 nm with a loop density of $2.3\text{x}10^{16}$ cm^{-3}. While an increase by nearly a factor of 2 in loop density is expected as compared to the 5 dpa sample, the decrease in loop size was a surprise. The decrease in loop size may be due to the presence of finely distributed small precipitates developed at high dose. The finely distributed precipitates, shown in Figure D.19, were not seen in the 5 dpa and the unirradiated samples. The average size of these precipitates is 5.9 nm, about 50% smaller than the precipitates observed in the 5 dpa sample shown in Figure D.20. Since the dark field image of the precipitates in Figure D.21 was taken using the diffraction from the precipitates, not all the precipitates were present in the picture. The estimated precipitate number density is greater than $9.1\text{x}10^{15}$ cm^{-3}, at least more than two orders of magnitude higher than the precipitate density in the 5 dpa sample. Both composition analysis and the crystal structure determination for these small precipitates were not successful due to their small sizes. These uniformly distributed small precipitates are expected to play an important role in material mechanical properties. Once formed, these precipitates will act as extensive sinks for point defects and alter the microstructural evolution under irradiation such as loop formation and growth. It is believed the presence of finely distributed precipitates may be responsible for the decrease in loop size at high dose comparing to 5 dpa sample.

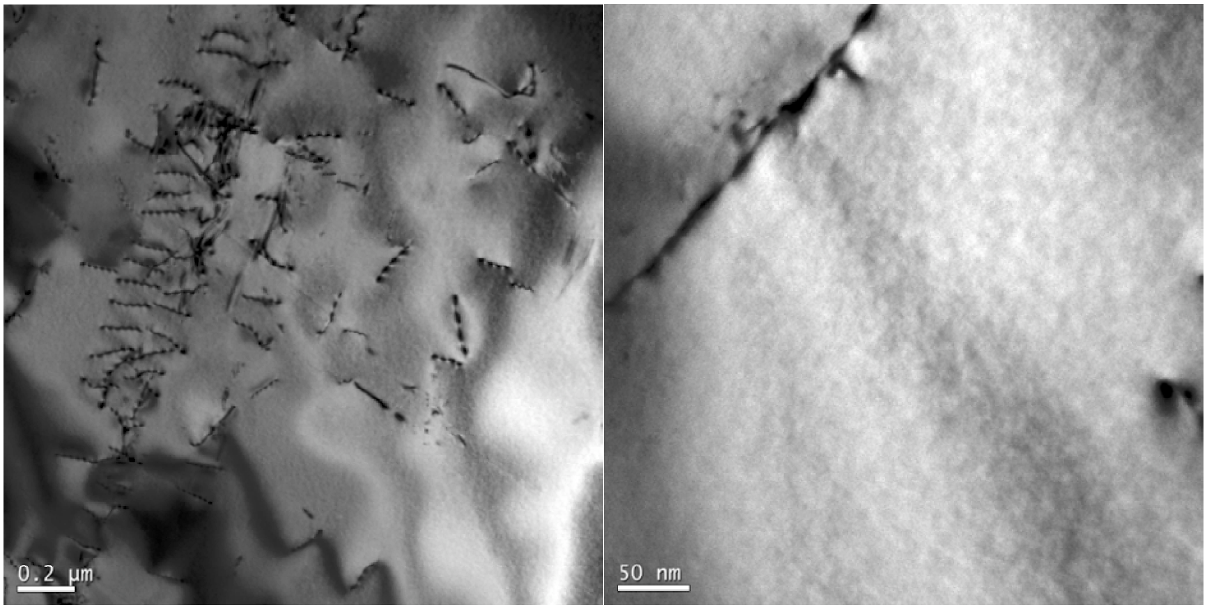

Figure D.15. Unirradiated microstructure of alloy 800H (imaged with g=200 diffraction) reveals dislocations in low magnification (left) and high magnification (right). The alloy has a relatively high dislocation density considering it was heat-treated at 1177ºC for 2.25 hours.

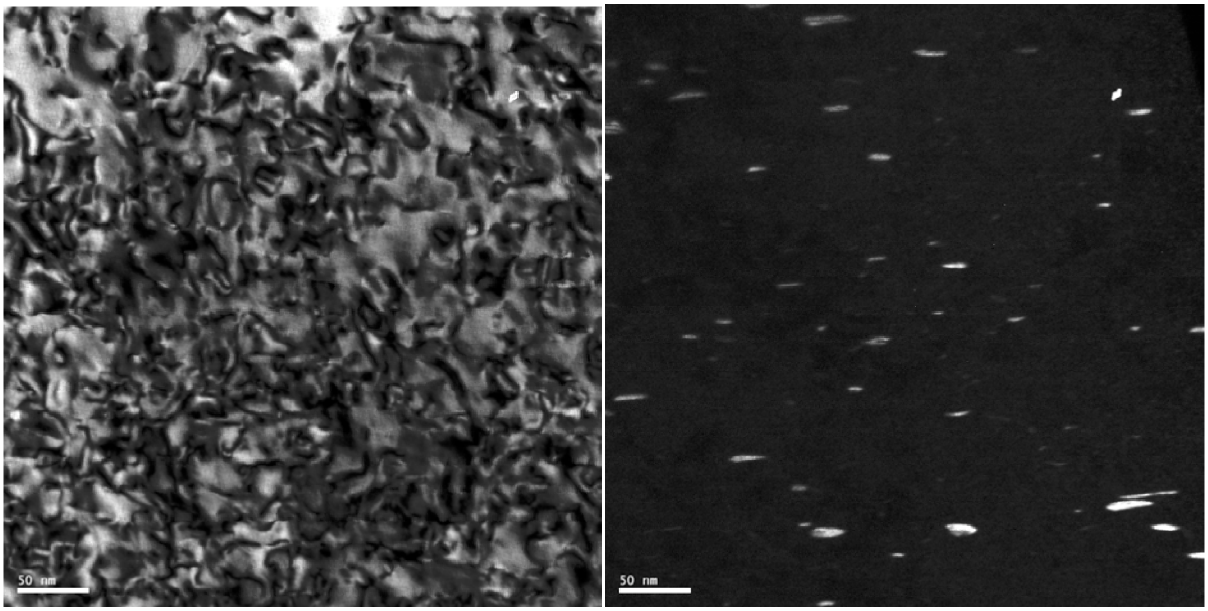

Figure D.16. Microstructure in alloy 800H irradiated with Ni ion at 500ºC to dose of 5 dpa. Bright filed image (left) showing dislocation loops under g=200 and the rel-rod dark filed image (right) showing ¼ of the faulted dislocation loops.

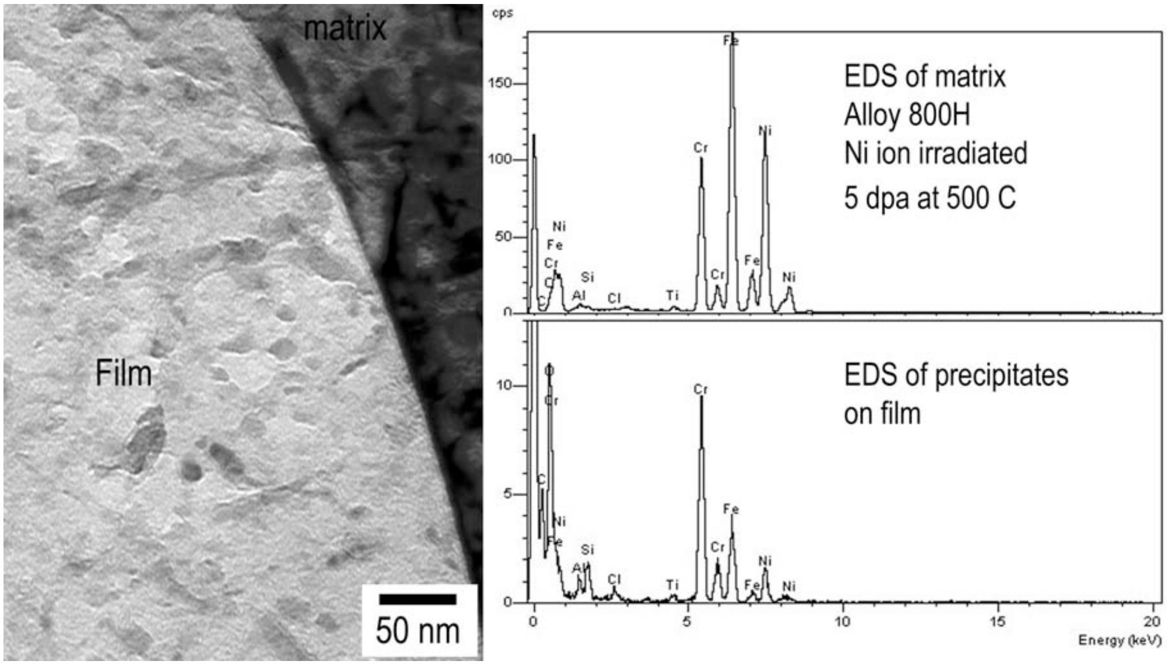

Figure D.17. Precipitates caught on a suspension film near the edge of the perforation (left) in 800H irradiated at 500ºC to 5 dpa. The EDS comparison between the matrix and precipitates on film showing the precipitates are rich in Cr, Si, Al and Ti.

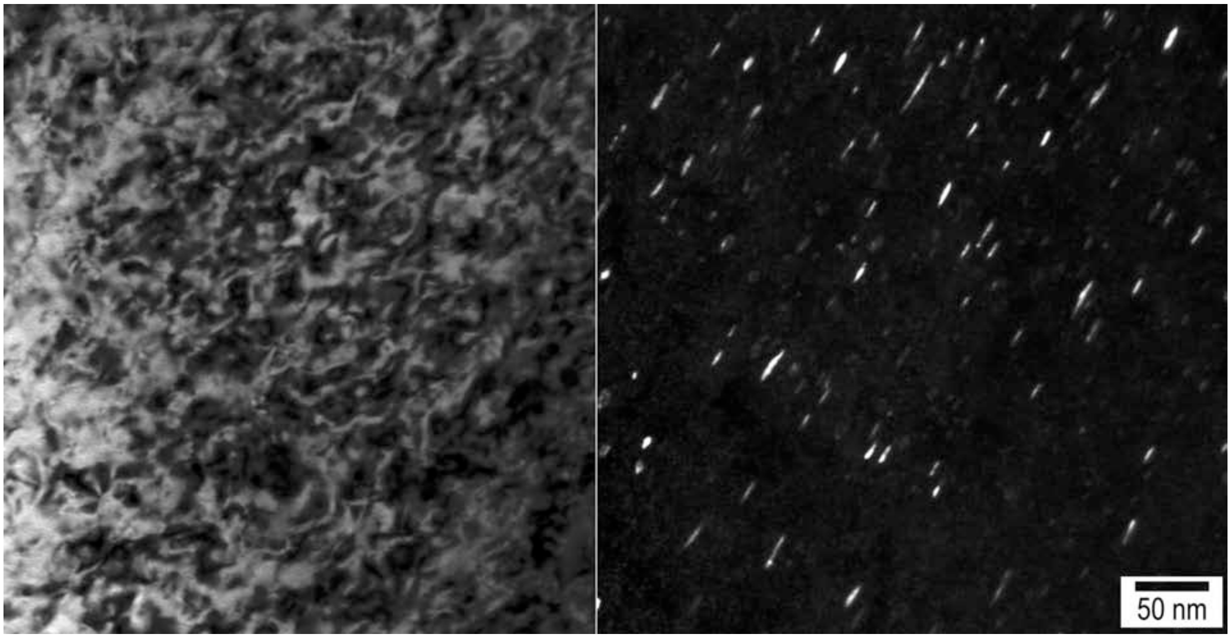

Figure D.18. Microstructure in alloy 800H irradiated with Ni ion at 500ºC to dose of 50 dpa. Bright filed image (left) showing dislocation loops under g=200 and the rel-rod dark filed image (right) revealing ¼ of the faulted dislocation loops.

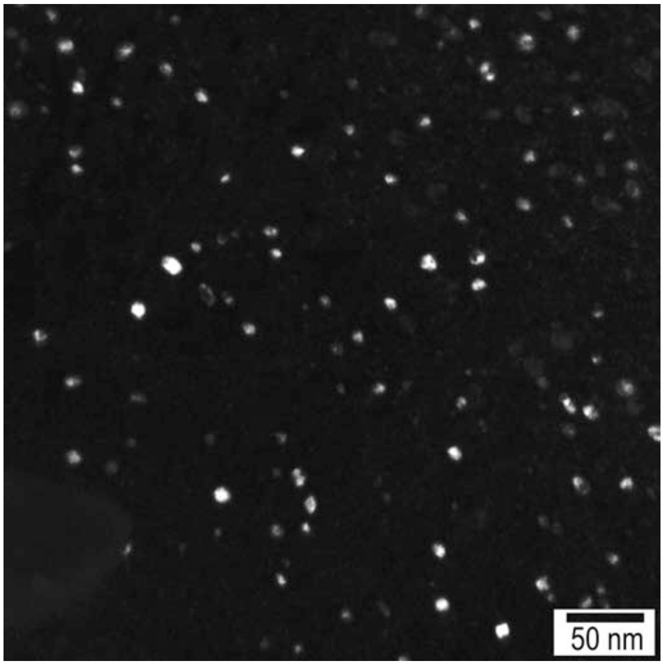

Figure D.19, Dark file image of finely distributed precipitates in 800H irradiated with Ni ions at 500ºC to 50 dpa. The image was taken using the diffraction from the precipitates.

D.2.3 800H Irradiated in ATR, HFIR, and PHENIX

Three millimeter diameter disks of 800H have been irradiated in the ATR reactor at 500°C and 800°C to low dose (1-3 dpa). These reside at the Idaho National Laboratory and are scheduled for future examination. As mentioned in section B, grain boundary engineered and control tensile samples have been irradiated in HFIR and will be examined in the future. Samples of 800H have also been included in the FUTURIX-SMI irradiation campaign.

D.3 Future Work

- The effect of GBE on the radiation stability of 800H needs to be initiated.
- Analysis of irradiated 800H from ATR, HFIR, and PHENIX
- Broader studies on microstructural development of 800H under radiation can be achieved using ion beam techniques

D.4 References

[D.1] Lindgren, J. R., “Irradiation effects on high-temperature gas-cooled reactor structural materials,” *Nuclear Technology*, **66**, 607, (1984).
[D.2] Thiele et al., “Investigation into the irradiation behavior of high-temperature alloys for high-temperature gas-cooled reactor applications,” *Nuclear Technology*, **66**, 597, (1984).
[D.3] Harman, D. G., “Incoloy 800: enhanced resistance to radiation damage,” *Nuclear Applications and Technology*, **9**, 561, (1970).
[D.4] James, L. A., “Effect of fast neutron irradiation on fatigue-crack growth behavior of three nickel-base alloys,” *Nuclear Technology*, **53**, 64, (1981).
[D.5] Brinkman et al., “Influence of irradiation on the creep/fatigue behavior of several austenitic stainless steels and Incoloy 800 at 700 C,” *Effects of Radiation on Substructure and Mechanical Properties of Metals and Alloys*, *ASTM STP 529*, 473, (1973).
[D.6] Gelles, D. S., “Microstructural examination of several commercial alloys neutron irradiated to 100 dpa,” *Journal of Nuclear Materials*, **148**, 136, (1987).
[D.7] J. F. Bates and R. W. Powell, J. Nucl. Mater (1981) 200

E. Literature Survey of Radiation Effects in High Temperature Ni-Base Alloys (Hastelloy Variants)

E.1 Mechanical Strength-thermal Aging

McCoy et al. performed tensile tests on Hastelloy-X [E.1]. The base metal was aged in both flowing HTGR helium and inert gas for a maximum aging time of 20,000 hours and temperatures up to 871°C. The tensile tests were then done on the samples at ~25°C. Figure E.1 shows the influence of aging on the yield stress (YS) and the ultimate tensile stress (UTS).

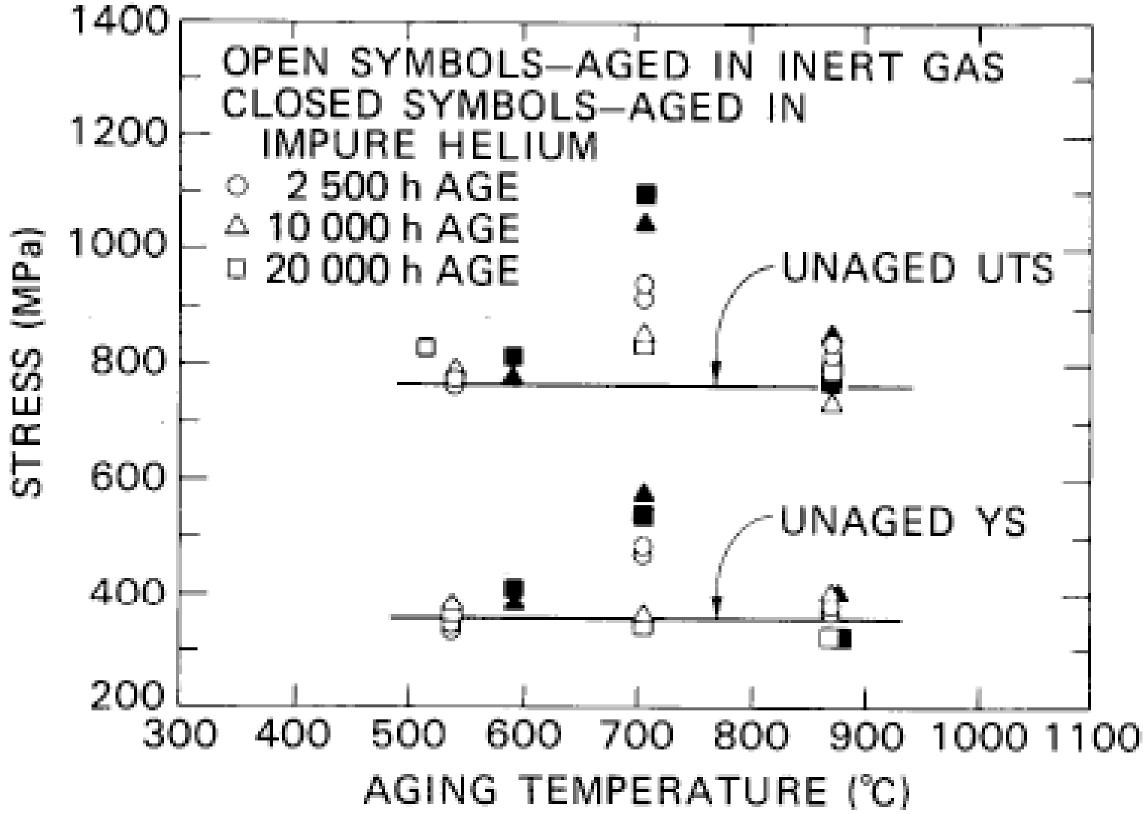

Figure E.1. Influence of aging temperature on Yield Strength and Ultimate Tensile Strength of Hastelloy-X subsequently tested at 25°C.

As can be seen in the figure above, aging at 704°C had the greatest effect on stress. The samples aged in the inert gas show an increase of ~25% in both YS and UTS after about 2,500 hours. However, after longer aging times, the increase in strength is lost. With the samples aged in the impure helium, the strength increase continues to the longer aging times. McCoy et al. hypothesize that the carburization that occurs in the HTGR helium leads to the formation of carbides with structures that were strengthening [E.1]. The variations of strength at temperatures higher and lower than 704°C were very small.

In addition to tensile testing at 25°C, some of the samples were tested at the aging temperatures [E.1]. The testing of these samples show that the as-received samples and the samples aged for 20,000 hours in inert gas had identical strength properties. However, the samples aged for the same amount of time in helium had increased strengths when compared to the as-received samples. The largest increase was seen at the aging temperature of 704°C. Figure E.2 shows these results.

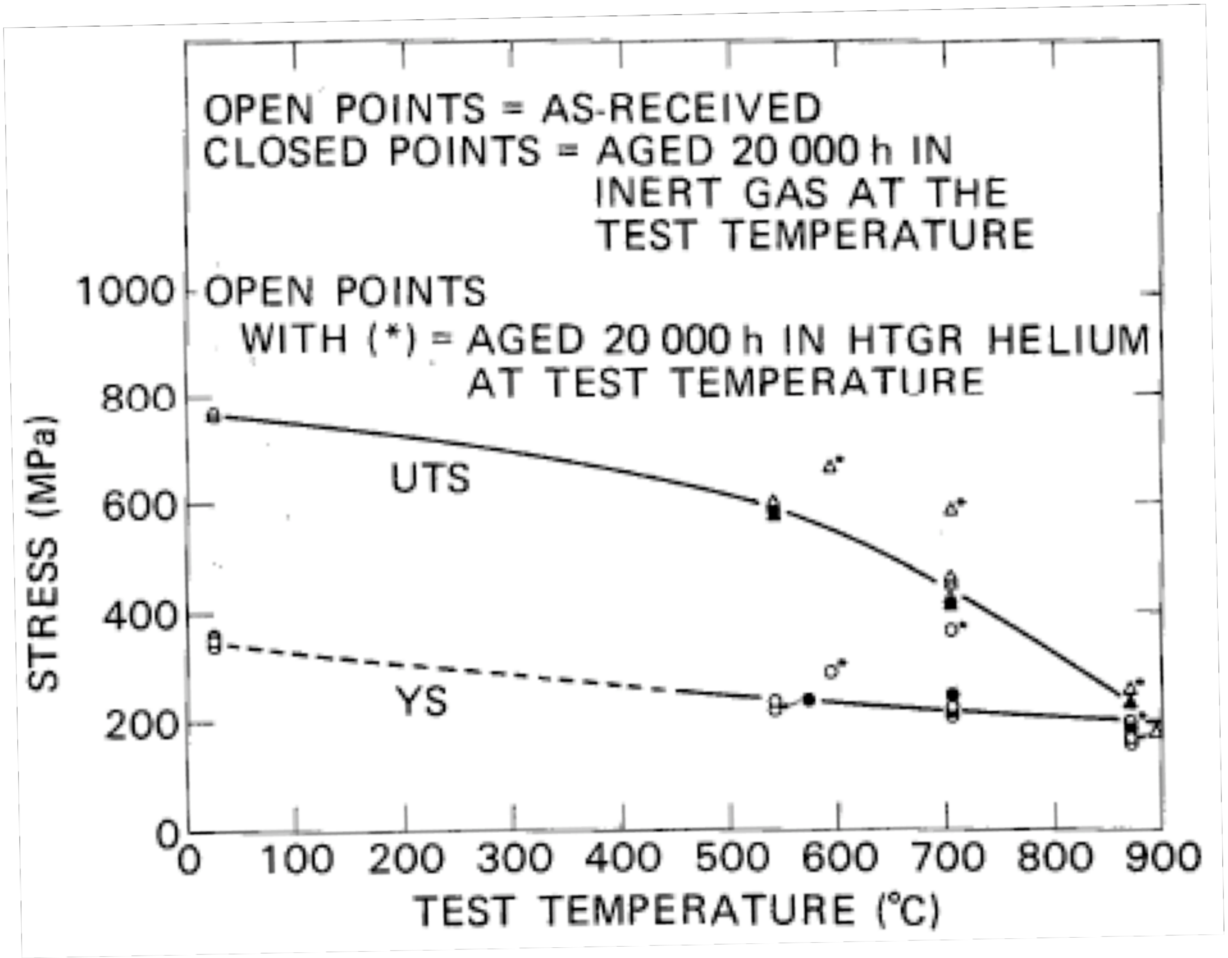

Figure E.2. Yield Strength and Ultimate Tensile Strength of Hastelloy-X samples aged and subsequently tested at the aging temperature.

Hastelloy-X shows a trend of decreasing elongation with aging [E.1]. The trend is particularly obvious at 704°C and 871°C. Figure E.3 shows these results. After aging for several thousand hours at 704°C or 871°C, the samples show elongation values reduced to only 10 to 20% of the original values. In all cases the elongation after aging in helium was less than that obtained after aging in the inert gas. The lowest value obtained for elongation was 8.2% after aging for 20,000 hours at 704°C in helium.

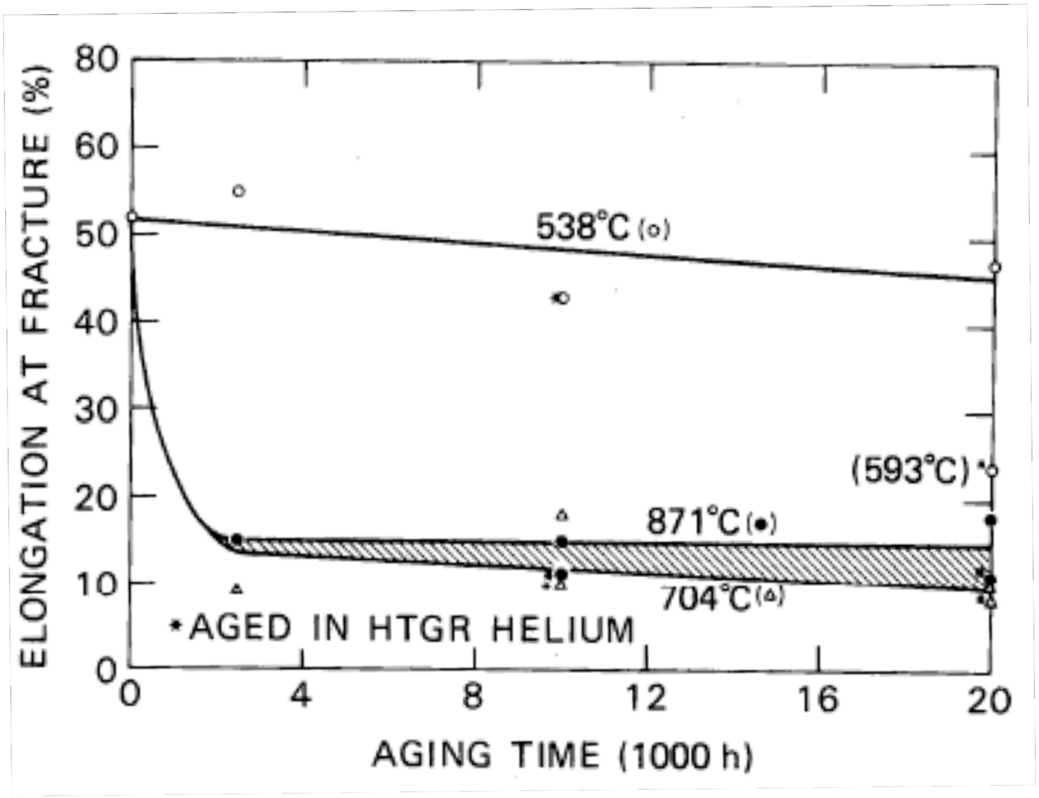

Figure E.3. Elongation of Hastelloy-X at 25°C after aging at the indicated temperatures.

The elongation of Hastelloy-X was also tested at the same temperature at which they were aged [E.1]. The elongation of these samples at fracture can be seen in Figure E.4. The values of elongation are the same for as-received samples and the samples aged in the inert gas for 20,000 hours. The samples aged in the helium show significantly lower fracture elongations than the as-received samples. The lowest value of 21.4% occurs in a sample aged for 20,000 hours at 593°C in helium.

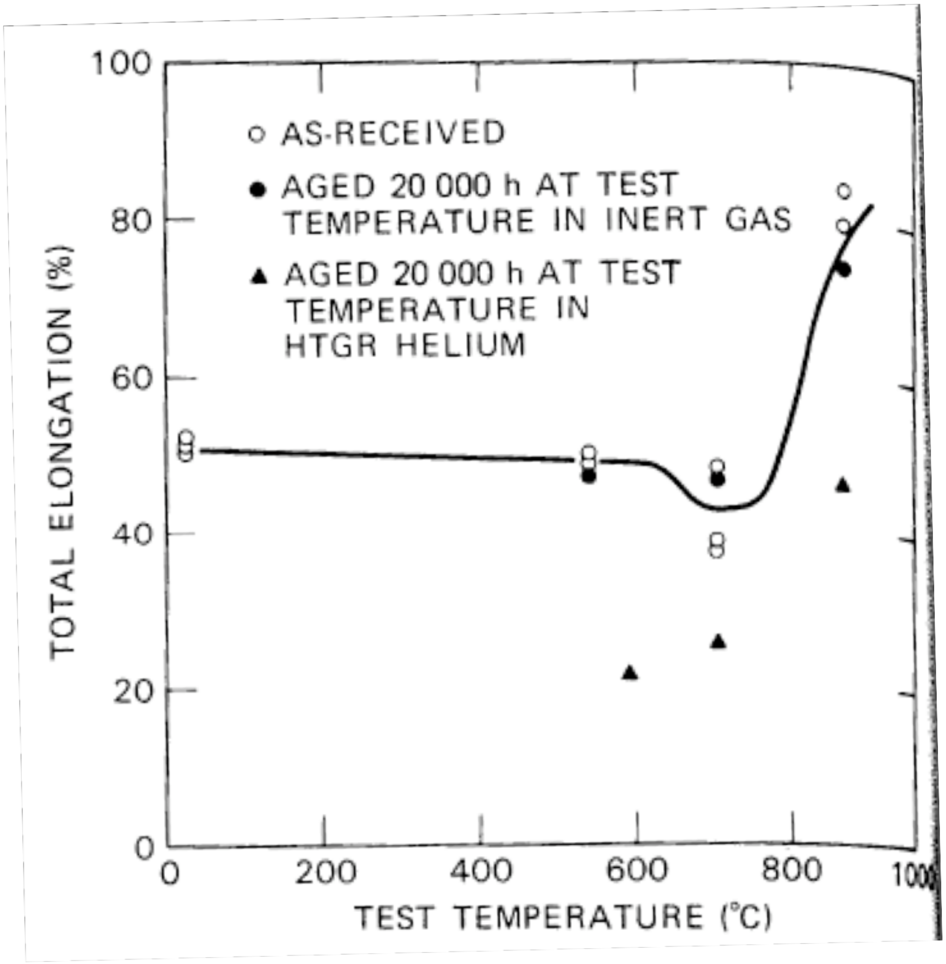

Figure E.4. Elongation of Hastelloy-X samples aged and tested at the same temperature.

E.2 Mechanical Strength and Ductility-irradiation

Tensile tests on Hastelloy-X were performed by Thiele et al at temperatures of 600, 700 and 850°C [D.2]. Prior to testing, the samples were irradiated to a thermal fluence of $1.1\text{x}10^{25}$ m^{-2} at 375°C. Following irradiation, the irradiated samples were tested at the indicated temperature along with unirradiated samples. The tensile tests were carried out in air with a strain rate of 0.3%/min up to 1% strain. Beyond this, the strain rate was raised to 10%/min until rupture.

Figure E.5 shows the results of the tensile tests on Hastelloy-X [E.2]. Hastelloy-X is represented by alloy 3 in this figure. This alloy shows an increase of the 0.2% proof stress after irradiation. However, as the temperature is increased, the increase in yield strength becomes smaller. Figure E.6 shows the ultimate tensile strength before and after irradiation. Hastelloy-X shows a decrease in ultimate tensile strength after irradiation. This effect is more pronounced as the test temperature is increased.

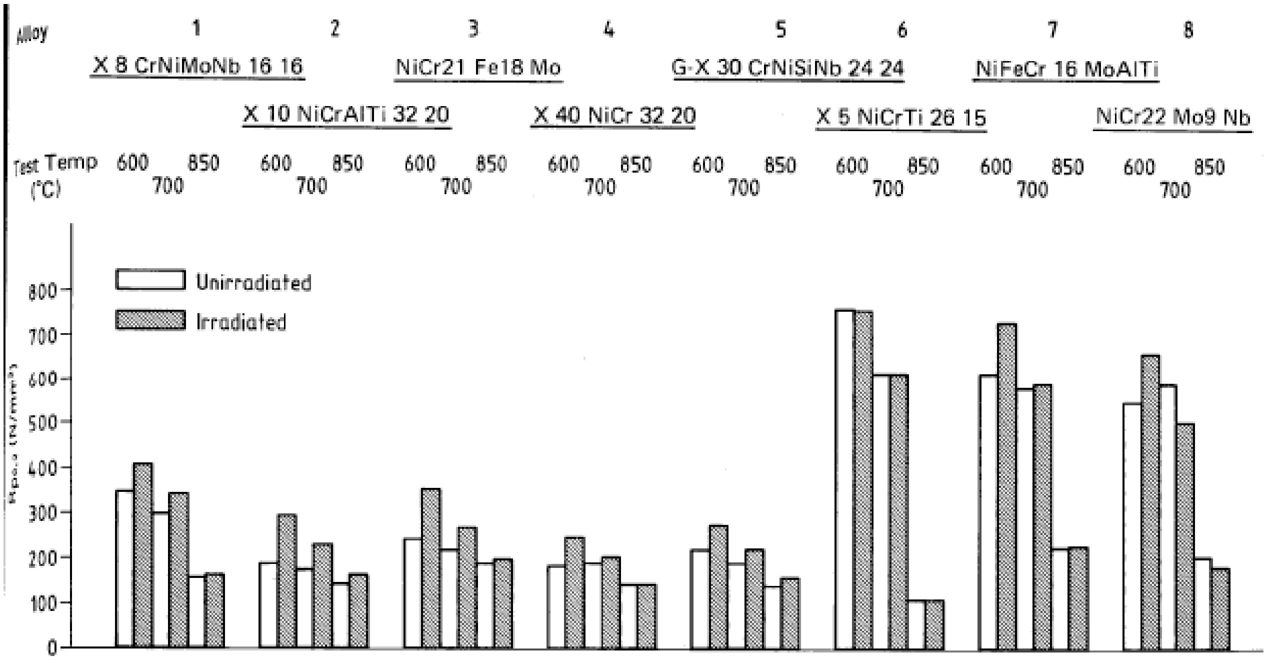

Figure E.5. Influence of test temperature on yield strength ($R_{p0.2}$ or 0.2% proof stress) of Hastelloy-X (alloy 3) before and after irradiation.

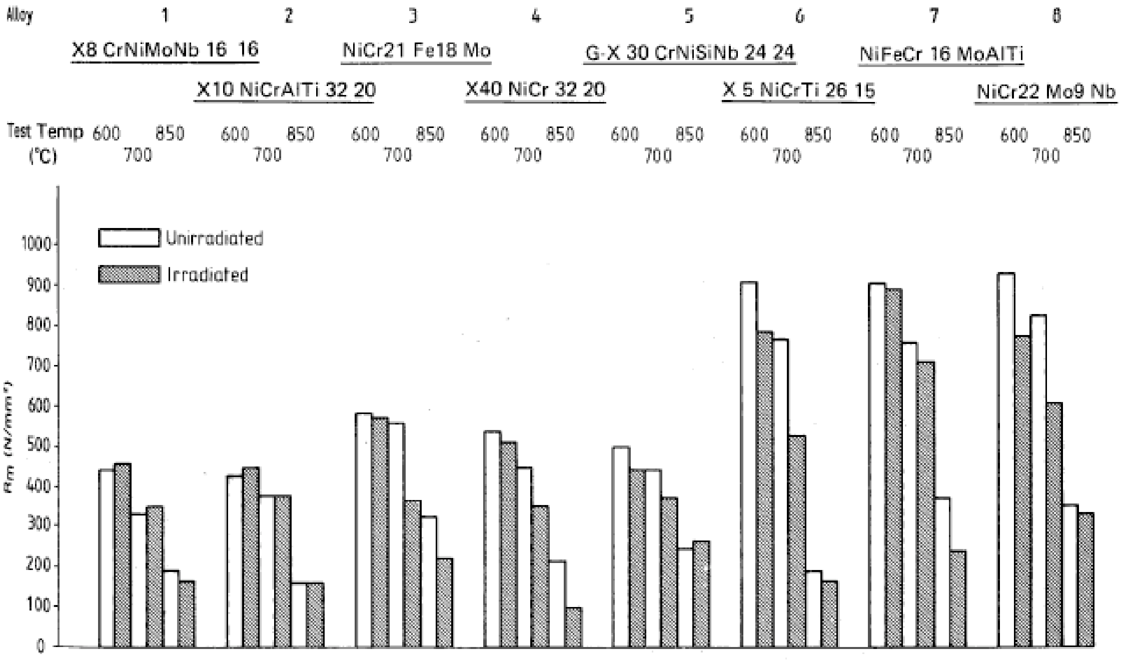

Figure E.6. Influence of test temperature on ultimate tensile strength (R_{max}) of Hastelloy-X (alloy 3) before and after irradiation.

Room temperature and elevated temperature tensile data on previously irradiated Hastelloy-X is presented by Lindgren [E.3]. Figure E.7 shows that the strength increases and the elongation decreases at every test temperature.

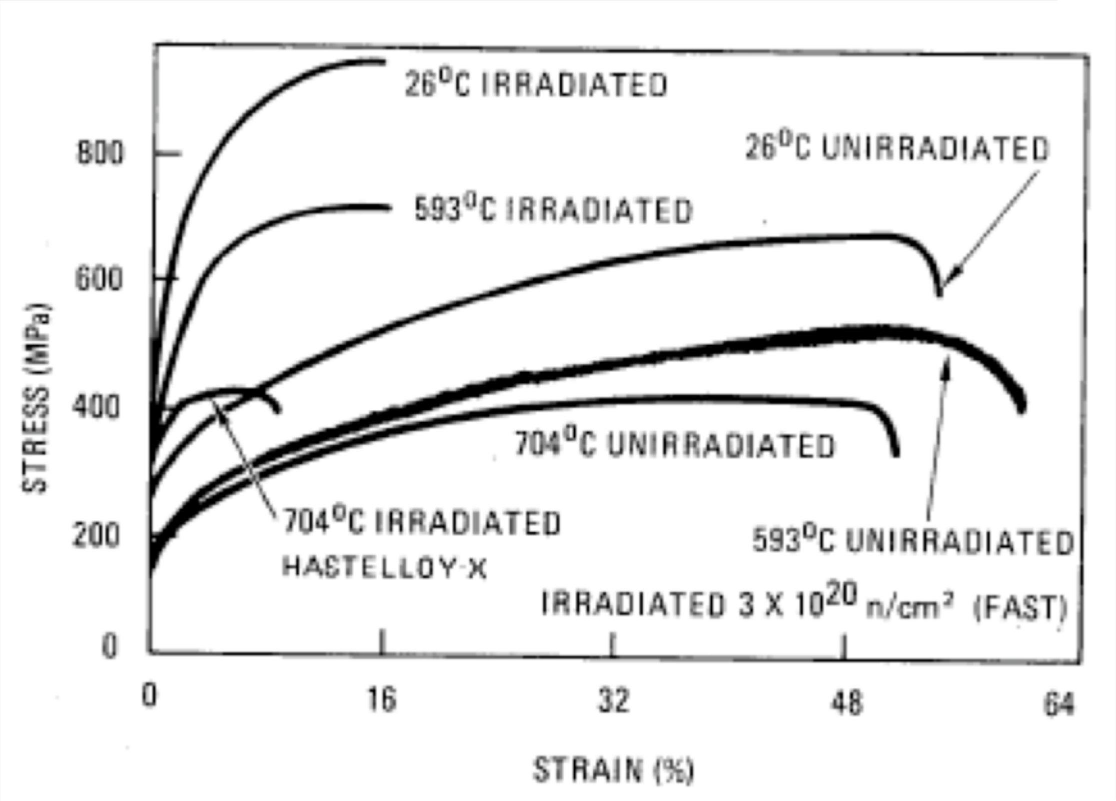

Figure E.7. Stress-strain curves for Hastelloy-X before and after irradiation of fast neutrons to $3.3 \times 10^{20} n/cm^2$.

Rupture elongation of Hastelloy-X was studied by Thiele et al [E.2]. They found that rupture elongation is most affected by irradiation. A loss of ductility was found at all testing temperatures for the alloy. This drastic decrease in ductility can be seen in Figure E.8. Hastelloy-X was also found to have major high-temperature irradiation embrittlement at 700°C and 850°C.

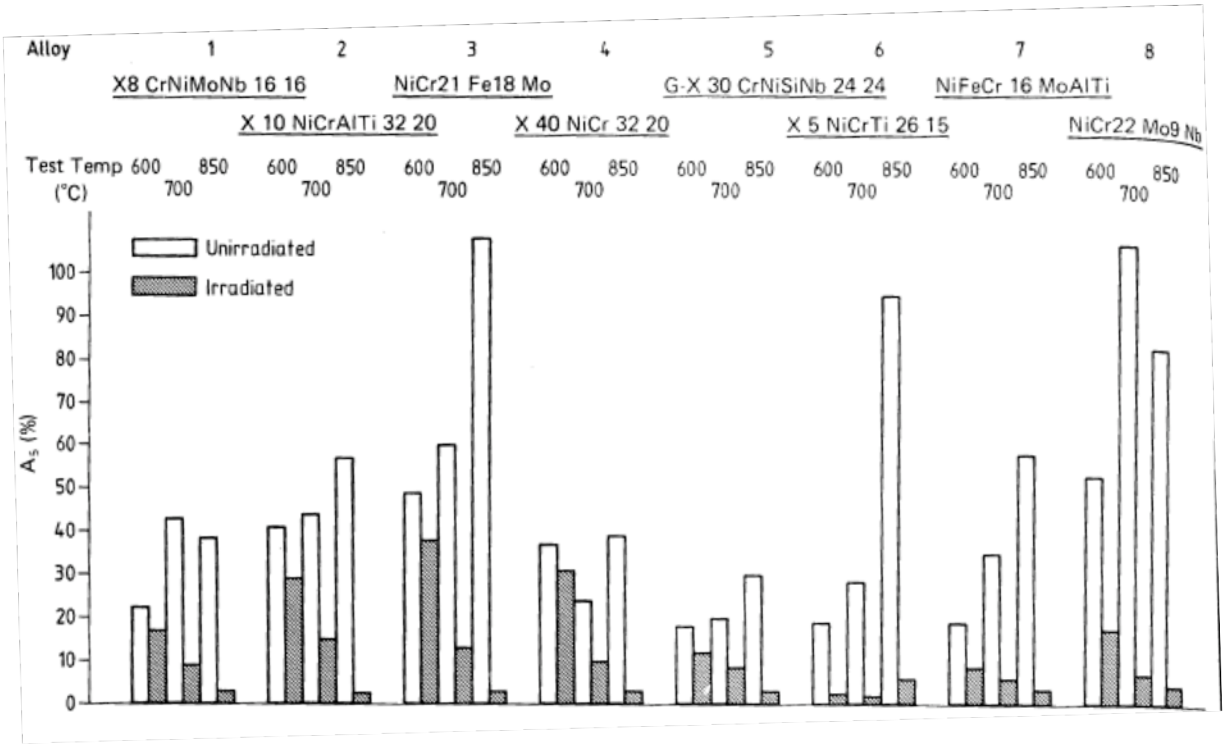

Figure E.8. Influence of test temperature on rupture elongation (A_s) of Hastelloy-X before and after irradiation.

Lindgren measured the tensile ductility of various metallurgically modified Hastelloy-X samples [E.3]. Figure E.9 shows that irradiation decreased the ductility of Hastelloy-X, but this effect was mitigated by decreasing the boron content in the alloy (presumably reducing the formation of transmuted helium that forms bubbles and leads to loss of ductility). The effects of thermal neutron dose on Hastelloy samples with slight differences in boron concentration are also shown in Figure E.10. Ductility is lost with increasing neutron fluence and the loss appears slightly faster for alloys with higher bulk boron concentrations.

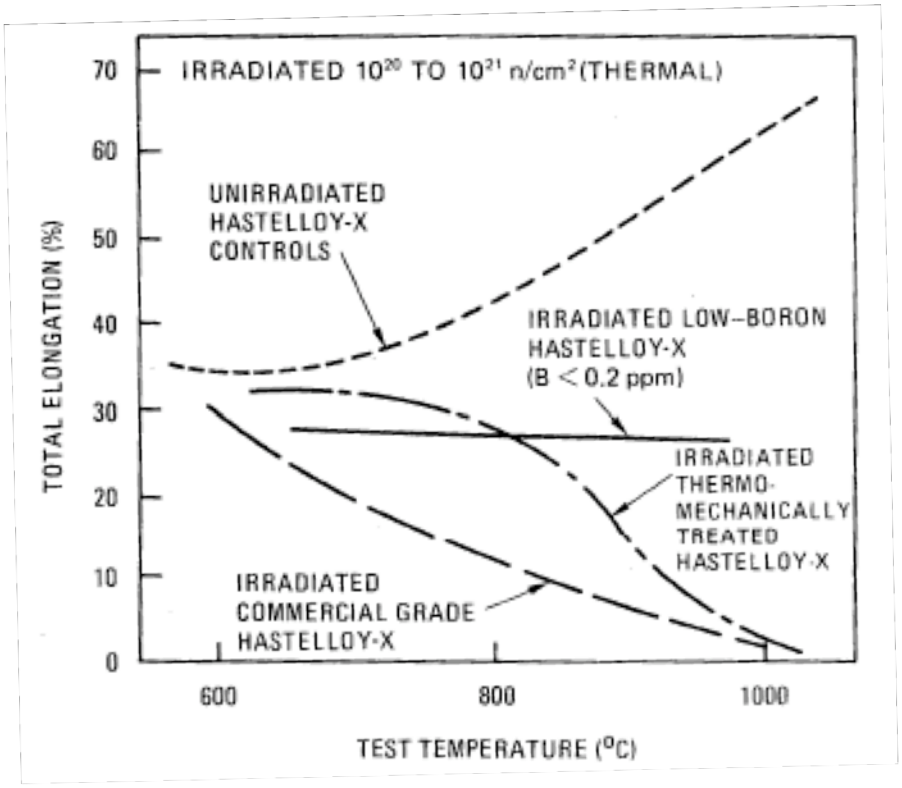

Figure E.9. Improvement of post-irradiation tensile ductility of Hastelloy-X by metallurgical modifications.

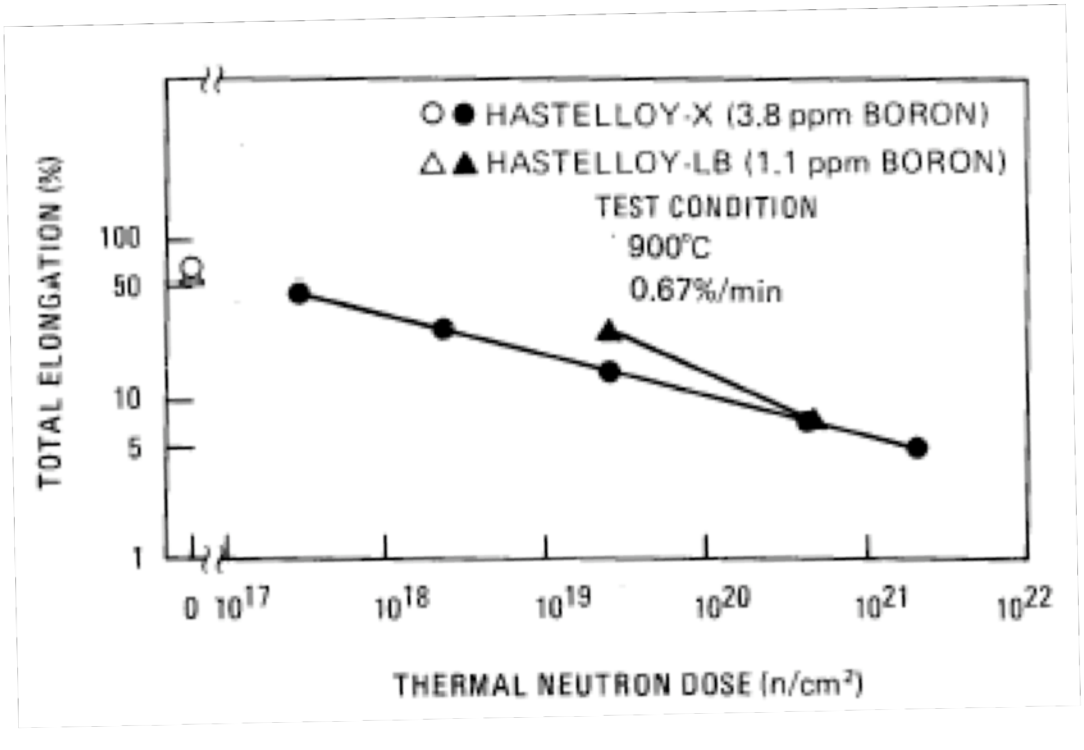

Figure E.10. Effect of thermal neutron dose on total elongation of irradiated Hastelloy alloys.

Lindgren also presents data on the load versus elongation of Hastelloy-X tested at 600, 700 and 850°C following irradiation with thermal and fast fluences of 1.1×10^{21} n/cm^2 in Figure E.11 [E.3].

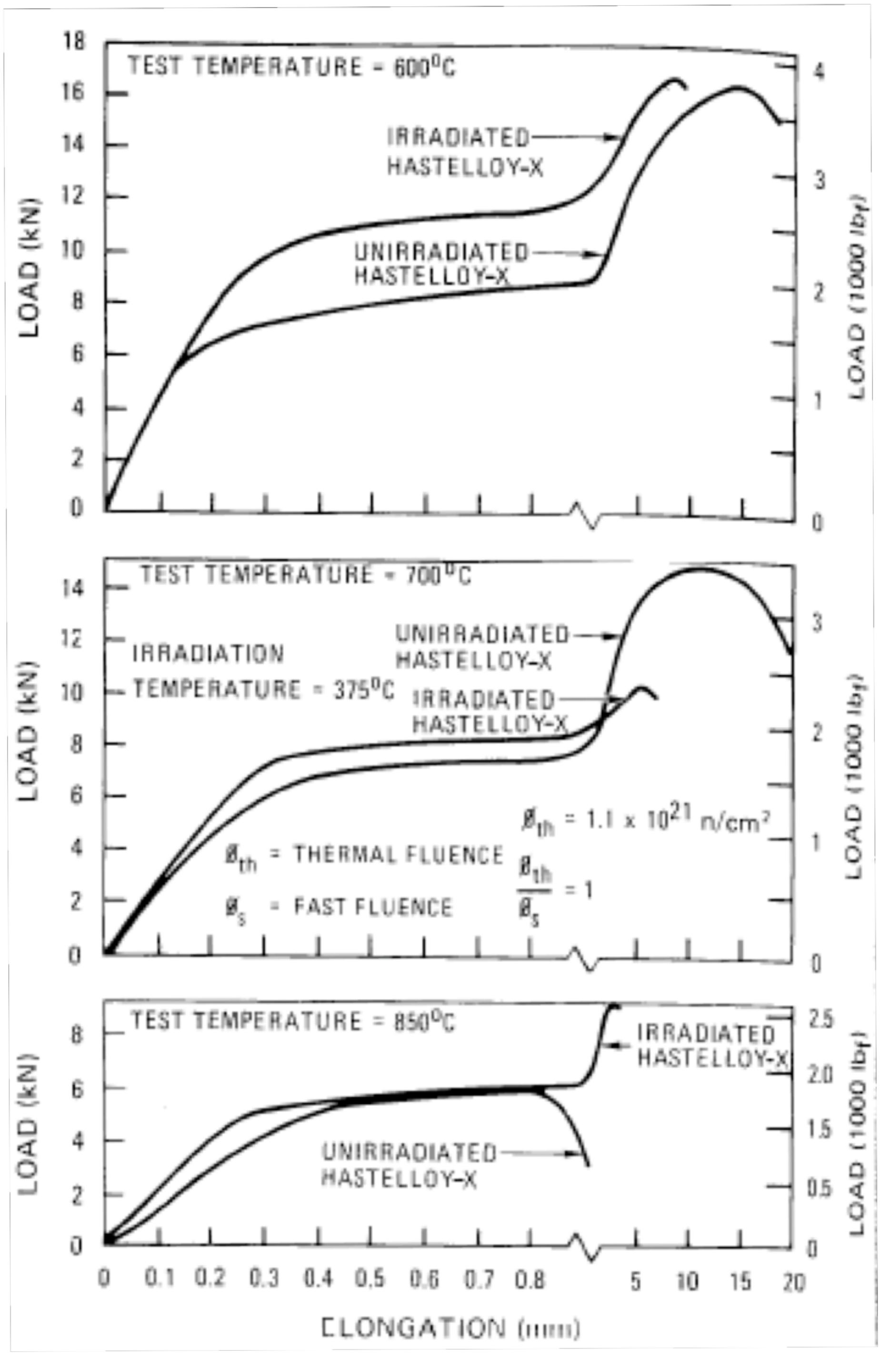

Figure E.11. Load versus elongation of Hastelloy-X tested at 600, 700 and 850°C following irradiation.

E.3 Fatigue

Strain-controlled fully reversed fatigue tests were performed from room temperature to 871°C with a cyclic strain rate of $4\text{x}10^{-3}$/s [E.1]. Figure E.12 shows strain-controlled data for Hastelloy-X generated in air up to 871°C. A significant decrease in the continuous cycle fatigue life is seen between room temperature and 538°C. This trend continues as the aging temperature is increased.

Hastelloy-X samples were also fatigue tested after solution annealing and solution-annealing plus aging in both air and HTGR helium [E.1]. Little or no difference in the sample fatigue was seen between the samples aged in air and the samples aged in helium at 538°C. However, thermally aging the samples before testing can reduce fatigue life, depending on the prior exposure time. Figure E.13 shows this data.

Samples of Hastelloy-X were also thermally aged for 10,000 hours at 871°C and then fatigue tested at the same temperature [E.1]. This thermal aging decreased the low-cycle life of the alloy. However, that cycle life was restored when the thermal aging time was extended to 20,000 hours. McCoy et al. speculate that this change was seen due to subtle changes in the alloy microstructure and resulting changes in ductility. Figure E.14 shows these results.

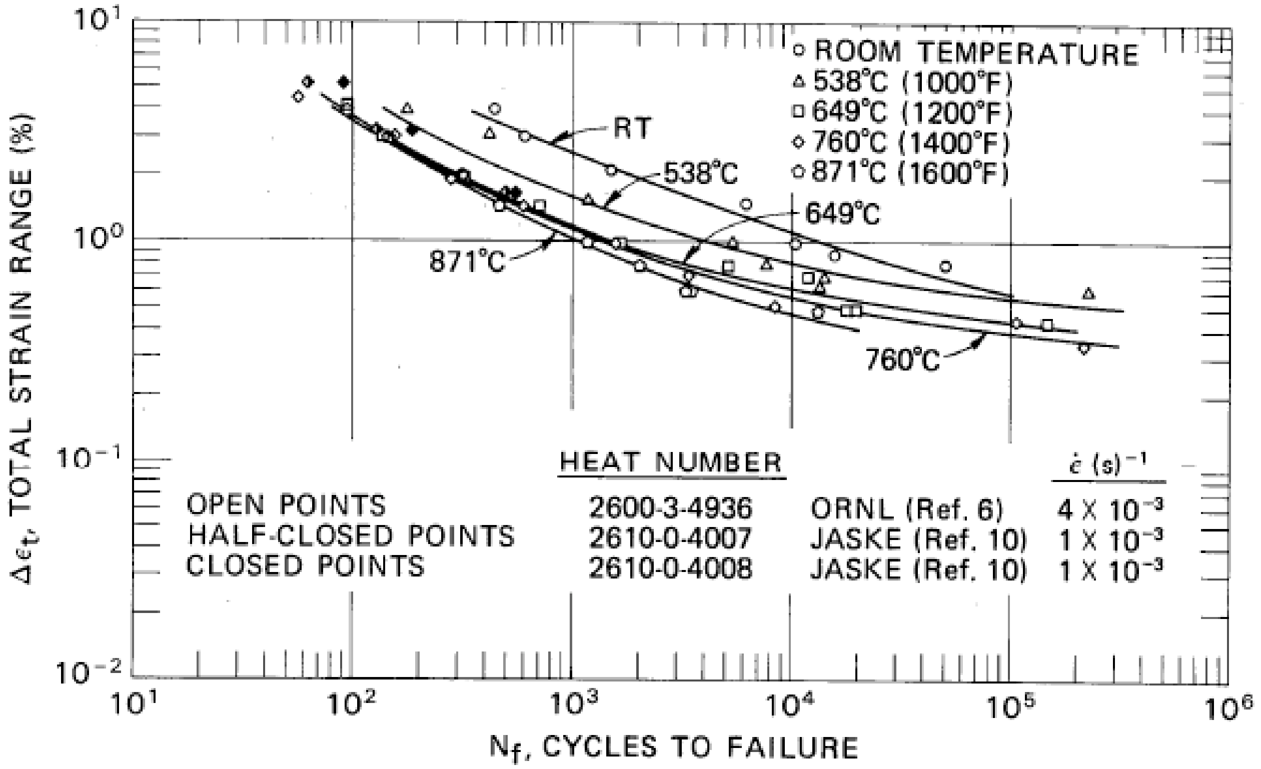

Figure E.12. Total strain range versus cycles to failure for Hastelloy-X tested in air.

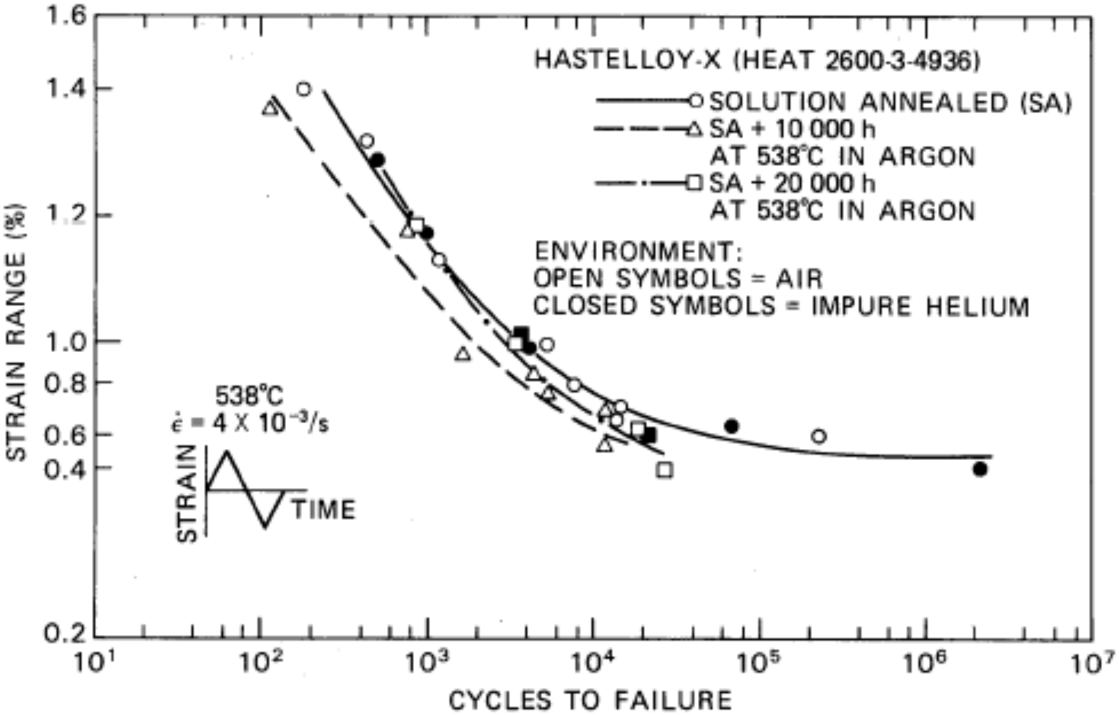

Figure E.13. Comparison of strain-controlled fatigue data generated at 538°C in air and HTGR helium for Hastelloy-X.

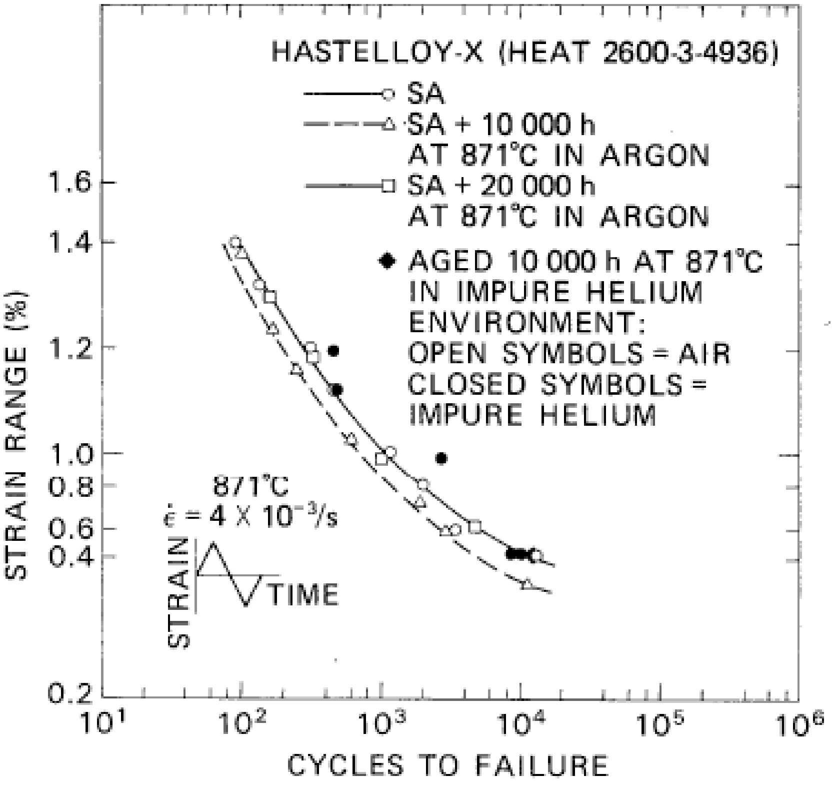

Figure E.14. Comparison of strain-controlled fatigue data generated at 871°C in air and HTGR helium for Hastelloy-X.

E.4 Creep

McCoy et al performed creep studies on two heats of the Hastelloy-X alloy [E.1]. The test results for the time to 2% strain as a function of stress showed no detectable influence by lot or test environment. Figure E.15 shows these creep results.

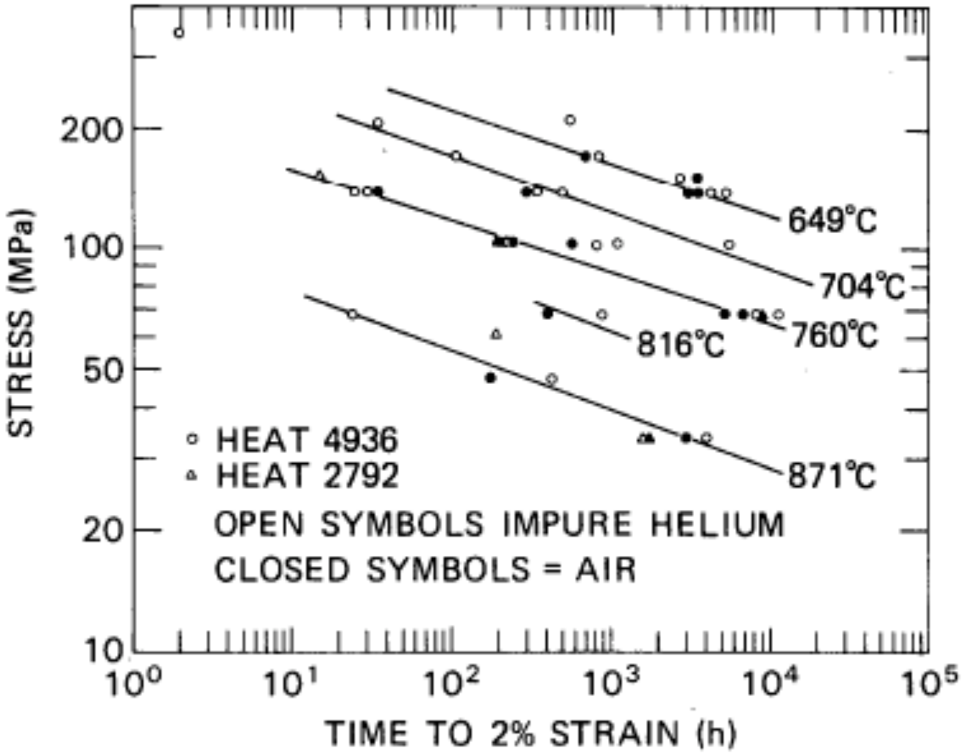

Figure E.15. Time to 2% strain as a function of stress for Hastelloy-X.

Stress/rupture properties were observed for rupture times up to 40,000 hours [E.1]. As with lower strains, lot and test environment have no detectable effects. As can be seen in Figure E.16, the only irregularity seen in the creep data exists at 760°C after approximately 20,000 hours where two tests fail and two continue. The results from these two continuing tests are not known.

The creep strain for each test is shown as a function of rupture time in Figure E.17 [E.1]. The circles represent heat 4936 with the triangles represent heat 2792. The open symbols were aged in impure helium and the closed symbols were aged in air. The samples run in the impure helium fail at lower strains than those tested in air. However, the lowest fracture strain was still greater than 10%.

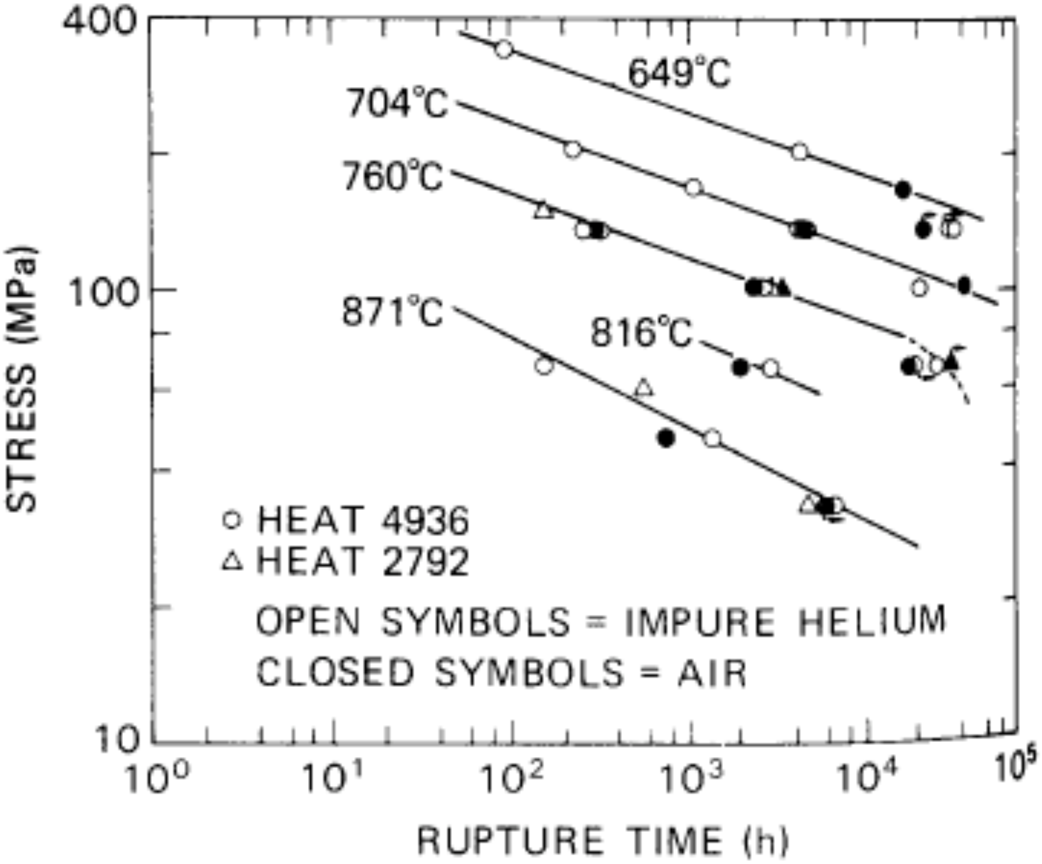

Figure E.16. Stress/rupture properties of Hastelloy-X.

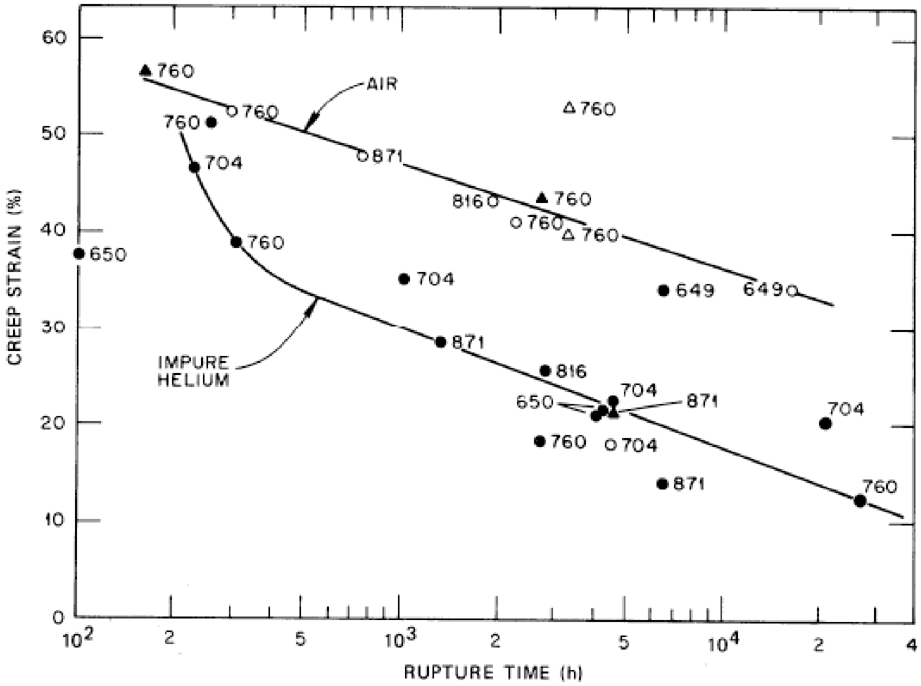

Figure E.17. Relation of creep strain to rupture life for Hastelloy-X.

E.5 Creep Rupture

The alloy Hastelloy-XR has been studied by K. Hada et al [E.4]. The nickel-based alloy Hastelloy-XR was developed to have superior corrosion resistance under exposure to the primary helium coolant in the Japanese High Temperature Test Reactor. Figure E.18 shows the creep rupture life data for Hastelloy-XR. This data shows that the maximum rupture life reaches 30,000 hours.

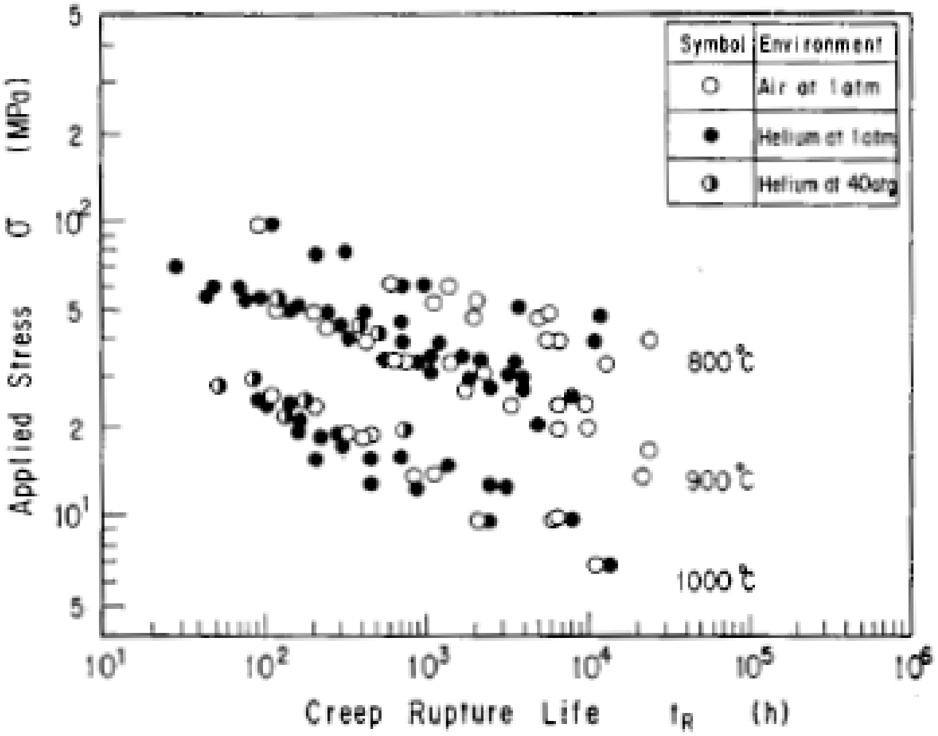

Figure E.18. Creep rupture strength for Hastelloy-XR

E.5 References

[E.1] McCoy et al., “Hastelloy-X for high-temperature gas-cooled reactor applications,” *Nuclear Technology,* **66**, 161, (1984).

[E.2] Thiele et al., “Investigation into the irradiation behavior of high-temperature alloys for high-temperature gas-cooled reactor applications,” *Nuclear Technology*, **66**, 597, (1984).

[E.3] Lindgren, J. R., “Irradiation effects on high-temperature gas-cooled reactor structural materials,” *Nuclear Technology*, **66**, 607, (1984).

[E.4] K. Hada et al., “Application of new design methodologies to very high-temperature metallic components of the HTTR,” *Nuclear Engineering and Design,* **132**, 13, (1991).

F. Conclusions and Outlook

Any metallic material used in a GFR core is subject to unprecedented temperatures and neutron damage as compared to the environment experienced in a thermal spectrum gas-cooled reactor. This project is developing microstructurally tailored materials, specifically using grain boundary engineering techniques, to improve the creep strength, oxidation resistance, and radiation resistance of candidate metallic alloys. Several important results have been achieved, specifically:

- Grain boundary distributions have been altered to increase the fraction of low-energy boundaries in a ferritic-martensitic steel, T91, in an Fe-base austenitic alloys, 800H, and in a Ni-base alloy, 617.
- The grain boundary optimization in T91 has been shown to improve the creep resistance.
- The grain boundary optimization in 800H has been shown to reduce unwanted oxide spallation in alloy 800H
- The optimized grain boundary distributions have proven to be stable in all three alloys to certain limiting temperatures. The 617 stability studies indicate the stability is very dependent on the grain boundary character distributions, pointing to the possibility that the improved grain boundary distributions may be stable to higher temperatures than currently achievable.

To a limited extent, the radiation stability of alloy 800H has been examined using heavy ion irradiation. The studies show typical radiation hardening. These studies will be complimented by future data from samples irradiated in ATR, HFIR, and PHENIX. The HFIR samples include material that has undergone the GBE treatment.

Future work will continue to improve the distributions of grain boundaries in all three alloy systems, determine the temperature limits at which these treatments are stable and the dependence of this temperature on initial distribution. The fundamental basis for improved creep strength and improved oxidation resistance will be examined. Additional creep and long-term oxidation data will be obtained. The effect of GBE on radiation response and impact properties will be part of future studies.

The limited resources allocated to this work have already produced some remarkable improvements in properties that indicate improved potential for metallic materials in GFR service.

G. Papers

T. R. Allen, L. Tan, Y. Chen, X. Ren, K. Sridharan, G. S. Was, G. Gupta, and P. Ampornrat, Corrosion of Ferritic-Martensitic Alloys in Supercritical Water for GenIV Application, Proceedings of Global 2005, Paper 419.

T. R. Allen, Y. Chen, L. Tan, X. Ren, and K. Sridharan, Corrosion of Candidate Materials for Supercritical Water-Cooled Reactors, 12th Environmental Degradation Conference of Materials in Nuclear Power Systems-Water Reactors, Eds., Todd R. Allen, Peter J. King, and Lawrence Nelson, TMS, 2006, p. 1397.

J. Gan, J. I. Cole, T. R. Allen, University of Wisconsin, Madison, WI, USA, S. Shutthanandan, S. Thevuthasan, "Irradiated Microstructure of Alloy 800H," J. Nucl. Mater. 351(1-3) (2006) 223-227.

G. Gupta, G. S. Was, B.Alexandreanu, "Grain Boundary Engineering of Ferritic-Martensitic alloy T91," Journal of Metallurgical and Materials Transactions A, Vol. 35A, No. 2, pp. 717-719, 2004.

G. Gupta, G. S. Was, T.R.Allen, P.Ampornrat, "Role of Grain Boundary Engineering in Mitigating Stress Corrosion Cracking of HT-9 in Supercritical Water," Journal of Nuclear Materials, submitted, 2006.

G. Gupta, G. S. Was "The Role of Grain Boundary Engineering on the High Temperature Creep of Ferritic-Martensitic Alloy T91," Journal of ASTM international, March 2005, Vol.2, No.3.

G. Gupta, G. S. Was, "Interpretation of Improved Creep Properties of a 9Cr-1Mo-Nb- V (T91) Steel by Grain Boundary Engineering," TMS Letters, 2005, vol. 2, Issue 3, p.g 71-72.

L. Tan and T. R. Allen, An EBSD Study of Oxidation Behavior of an Iron-base Alloy in Supercritical Water Reactor, EPD Congress 2005 Edited by Mark E. Schlesinger TMS (The Minerals, Metals & Materials Society), 2005, p.61.

L.Tan and T.R. Allen, An electron backscattered diffraction study of grain boundary-engineered INCOLOY alloy 800H, Metallurgical and Materials Transactions A 36(7) (2005) 1921-1925.

L. Tan , K. Sridharan, T.R. Allen, The Effect of Grain Boundary Engineering on the Oxidation Behavior of INCOLOY Alloy 800H in Supercritical Water, J. Nucl. Mater. 348 (2006) 263.

L. Tan, K. Sridharan, and T. R. Allen, "Grain Boundary Engineering of FCC and BCC Alloys," Transactions of the 2006 ANS Annual Meeting, Reno, NV, Vol. 94, June 2006, p. 744.

L. Tan, K. Sridharan, and T. R. Allen, "Grain Boundary Engineering of FCC and BCC Alloys," submitted to J. Nucl. Mater. (NFSM)

L. Tan, K. Sridharan, T. Allen, G. Gupta, G. S. Was, “Improved Creep Properties of Grain Boundary Engineered 9Cr-1MoVNb (T91) steel,” Transactions of the 2006 ANS annual conference, Reno, NV, Vol. 94, June 2006, pp. 727-728.